NONLINEAR AEROSERVOELASTIC MODELLING AND ANALYSIS OF AIRCRAFT WITH CONTROL SURFACE FREEPLAY

A THESIS SUBMITTED TO
THE GRADUATE SCHOOL OF NATURAL AND APPLIED SCIENCES
OF
MIDDLE EAST TECHNICAL UNIVERSITY

BY

UTKU YURTSEVER

IN PARTIAL FULFILLMENT OF THE REQUIREMENTS
FOR
THE DEGREE OF MASTER OF SCIENCE
IN
AEROSPACE ENGINEERING

NOVEMBER 2022

Approval of the thesis:

NONLINEAR AEROSERVOELASTIC MODELLING AND ANALYSIS OF AIRCRAFT WITH CONTROL SURFACE FREEPLAY

submitted by **UTKU YURTSEVER** in partial fulfillment of the requirements for the degree of **Master of Science** in **Aerospace Engineering**, Middle East Technical University by,

Prof. Dr. Halil Kalıpçılar
Dean, Graduate School of **Natural and Applied Sciences** _____

Prof. Dr. Serkan Özgen
Head of the Department, **Aerospace Engineering** _____

Assoc. Prof. Dr. Melin Şahin
Supervisor, **Aerospace Engineering Dept., METU** _____

Prof. Dr. Altan Kayran
Co-Supervisor, **Aerospace Engineering Dept., METU** _____

Examining Committee Members:

Assoc. Prof. Dr. Ercan Gürses
Aerospace Engineering Dept., METU _____

Assoc. Prof. Dr. Melin Şahin
Aerospace Engineering Dept., METU _____

Assist. Prof. Dr. Ali Türker Kutay
Aerospace Engineering Dept., METU _____

Assoc. Prof. Dr. Mustafa Kaya
Aerospace Engineering Dept., AYBÜ _____

Assoc. Prof. Dr. Turaç Farsadi
Mechanical Engineering Dept., ATÜ _____

Date: 24.11.2022

I hereby declare that all information in this document has been obtained and presented in accordance with academic rules and ethical conduct. I also declare that, as required by these rules and conduct, I have fully cited and referenced all material and results that are not original to this work.

Name Last name : Utku YURTSEVER

Signature :

ABSTRACT

NONLINEAR AEROSERVOELASTIC MODELLING AND ANALYSIS OF AIRCRAFT WITH CONTROL SURFACE FREEPLAY

Yurtsever, Utku
Master of Science, Aerospace Engineering
Supervisor: Assoc. Prof. Dr. Melin Şahin
Co-Supervisor: Prof. Dr. Altan Kayran

November 2022, 137 pages

In this study, nonlinear aeroservoelastic analysis of aircraft with control surface freeplay is performed using the fictitious mass approach. For the demonstration of the nonlinear aeroservoelastic analysis methodology, an available very light aircraft (VLA) design configuration is selected. The aeroelastic model of the aircraft is obtained by combining the structural and aerodynamic models of the aircraft, which are prepared by the finite element modelling and analysis tool MSC.Patran/MSC.Nastran and the aeroelastic solver ZAERO, respectively. Nonlinear aeroservoelastic model of the aircraft is obtained by integrating the control surface freeplay models and the flight control algorithm created using MATLAB. The nonlinear effects of different control surface freeplays on the aircraft are investigated at various flight conditions. The results with aileron, elevator, and rudder freeplays show that for the particular aircraft studied, elevator is the most critical control surface in terms of nonlinear aeroservoelastic behavior of the aircraft leading to instability, and the freeplay in the rudder has no effect on the instability of the aircraft.

Keywords: Aeroelasticity, Aeroservoelasticity, Nonlinear Aeroservoelastic Modelling, Freeplay, Fictitious Mass Approach

ÖZ

BOŞTA HAREKET DAVRANIŞI İÇEREN KONTROL YÜZEYLERİNE SAHİP UÇAĞIN DOĞRUSAL OLMAYAN AEROSERVOELASTİK MODELLENMESİ VE ANALİZİ

Yurtsever, Utku
Yüksek Lisans, Havacılık ve Uzay Mühendisliği
Tez Yöneticisi: Dr. Melin Şahin
Ortak Tez Yöneticisi: Prof. Dr. Altan Kayran

Kasım 2022, 137 sayfa

Bu çalışmada uçaktaki kontrol yüzeylerindeki boşta hareket davranışından dolayı doğrusal olmayan bir şekilde hayali kütle kullanımı ile modellenip analiz edilmiştir. Doğrusal olmayan aeroservoelastik analiz metodolojisinin gösterimi için mevcut bir çok hafif hava aracı seçilmiştir. Sonlu elemanlar modelleme ve analiz programı MSC.Patran ve MSC.Nastran kullanarak oluşturulan uçağın yapısal modeli, aeroelastisite çözücüsü olan ZAERO ortamında oluşturulan aerodinamik model ile birleştirilerek aeroelastik model oluşturulmuştur. Uçuş kontrol algoritması MATLAB kullanarak oluşturulmuş ve sistemin doğrusal davranışını bozan kontrol yüzeylerindeki boşta hareket davranışı modellenmesi ile doğrusal olmayan aeroservoelastik model elde edilmiştir. Farklı boşta hareket davranışlarının serbest oynama açıları göz önüne alınarak doğrusal olmayan bu davranışın, uçağın üzerindeki etkisi zamana bağlı olarak ve farklı uçuş koşullarında incelenmiştir. Kanatçıklar, irtifa dümeni ve istikamet dümeninde yapılan incelemelerde, irtifa dümeninin uçağın aeroservoelastik davranışın en önemli kontrol yüzeyi olduğu belirlenirken istikamet dümenindeki boşta hareket davranışı uçağın kararsızlığı üzerinde etkisinin olmadığı saptanmıştır.

Anahtar Kelimeler: Aeroelastisite, Aeroservoelastisite, Doğrusal Olmayan Aeroservoelastik Model, Boşta Hareket Davranışı

To my beloved family,

ACKNOWLEDGMENTS

I would like to express my gratitude to Prof. Dr. Altan Kayran and Assoc. Prof. Dr. Melin Şahin, for their patience and supervisions through this study.

I would like to also thank Aerospace Engineering Department of Middle East Technical University and Turkish Aerospace Industries, Inc. for their significant Very Light Aircraft (ODTÜ-VLA) project which is studied in this thesis.

I am also thankful to my colleagues Başak Okumuş, Çağrı Koçan and my chief Evren Sakarya in Turkish Aerospace Industries, Inc. for their endless motivation, encouragement and help from beginning of my graduate program.

Special thanks to my close friends Uğur Tezcan and Mustafa Uğur for all our admirable memories in Aerospace Engineering Department and their motivations throughout this study.

My grateful thanks are for my friends Sedat Mert, Bader Bilgin and Atalays couple for their all endless friendships and precious coffee breaks.

TABLE OF CONTENTS

LIST OF TABLES

TABLES

LIST OF FIGURES

FIGURES

LIST OF ABBREVIATIONS

AE	Aeroelasticity
AIC	Aerodynamic Influence Coefficient Matrix
ASE	Aeroservoelasticity
CFD	Computational Fluid Dynamic
CG	Center of Gravity
FBW	Fly-by-wire
FCC	Flight Control Computer
FE	Finite Element
FM	Fictitious Mass
GAF	Generalized Aerodynamic Force Matrix
GFEM	Global Finite Element Model
LCO	Limit Cycle Oscillation
LQR	Linear Quadratic Regulator
RFA	Rational Function Approximation

LIST OF SYMBOLS

a	Aerodynamic displacement
a_∞	Freestream speed of sound
b	Half-span
C_l	Coefficient of roll moment in ZAERO
c_L	Coefficient of Lift
c_{L_α}	Derivative of c_L with respect to α
c_{L_q}	Derivative of c_L with respect to q
C_m	Coefficient of pitch moment in ZAERO
c_m	Coefficient of Pitch Moment
c_{m_α}	Derivative of c_m with respect to α
c_{m_q}	Derivative of c_m with respect to q
C_n	Coefficient of yaw moment in ZAERO
c_n	Coefficient of Yaw Moment
c_{n_r}	Derivative of c_n with respect to r
c_{n_p}	Derivative of c_n with respect to p
C_x	Coefficient of drag in ZAERO
C_y	Coefficient of side force in ZAERO
C_z	Coefficient of lift in ZAERO
dB	Decibel
D	Drag force
F_h	Force and moments due to structural deformation
F_a	Aerodynamic force and moment vectors
F_I	Inertia force and moment vectors
F_R	Rigid body forces
F_f	Flexible body forces
g	Non-dimensional damping
h(t)	Structural displacement vector in time

$\{h\}$	Structural mode shape
$\{\bar{h}\}e^{i\omega t}$	Harmonic solution of structural displacement vector
Hz	Hertz
i	Complex number
k	Reduced frequency
L	Reference chord length
M	Mach number
M_∞	Freestream mach number
M_x	Roll moment
M_y	Pitch moment
M_z	Yaw moment
n_{aero}	Total number of aerodynamic boxes
N_h	Number of mode shapes
N_{lag}	Number of lag terms
n_{total}	Total number of degrees of freedom in GFEM
p	Roll rate
$\tilde{p}$	Non-dimensional Laplace parameter
q	Pitch rate
q_∞	Total dynamic pressure of freestream
r	Yaw rate
s	Laplace variable
$\{u_{ac}\}$	Commended deflection of control surface
$\{u_{ae}\}$	Aeroelastic input vector
$\{x_{ae}\}$	Aeroelastic state vector
$\{y_{ae}\}$	Aeroelastic output vector
$\{u_p\}$	Aeroelastic plant-level input vector
$\{x_p\}$	Aeroelastic plant-level state vector
$\{y_p\}$	Aeroelastic plant-level output vector
$\{u_R\}$	Rigid body input vector
$\{x_R\}$	Rigid body state vector
$\{y_R\}$	Rigid body output vector
$\{u_v\}$	Aeroelastic vehicle -level input vector

$\{x_v\}$	Aeroelastic vehicle -level state vector
$\{y_v\}$	Aeroelastic vehicle -level output vector
$\{u_{ae}\}$	Aeroelastic input vector
V	Velocity
V_f	Flutter speed
V_L	Limit speed
V-g	Velocity versus damping
V-f	Velocity versus frequency
$\{\delta\}$	Actuator state
δ_{cs}	Deflection of control surface
δ_{ail}	Deflection of aileron
δ_{rud}	Deflection of rudder
δ_{ele}	Deflection of elevator
δ_0	Freeplay angle
ε	Error in least square fit
$\{\xi\}$	Generalized Coordinate
λ	Complex eigenvalue
γ	Decay rate
ρ	Air density
Φ	Total velocity potential
ω	Natural frequency
°	Degree
$[\phi]$	Mass normalized modal matrix
$[\phi_h]$	Structural modal matrix
$[\phi_c]$	Kinematic control surface modal matrix
$[A_0]$	Aerodynamic stiffness matrix
$[A_1]$	Aerodynamic damping matrix
$[A_2]$	Apparent mass matrix
$[A_{ae}]$	Aeroelastic A matrix in state-space domain
$[B_{ae}]$	Aeroelastic B matrix in state-space domain
$[C_{ae}]$	Aeroelastic C matrix in state-space domain
$[D_{ae}]$	Aeroelastic D matrix in state-space domain

$[A_p]$	Aeroelastic plant-level A matrix in state-space domain
$[B_p]$	Aeroelastic plant-level B matrix in state-space domain
$[C_p]$	Aeroelastic plant-level C matrix in state-space domain
$[D_p]$	Aeroelastic plant-level D matrix in state-space domain
$[A_R]$	Rigid body A matrix in state-space domain
$[B_R]$	Rigid body B matrix in state-space domain
$[C_R]$	Rigid body C matrix in state-space domain
$[D_R]$	Rigid body D matrix in state-space domain
$[A_v]$	Aeroelastic vehicle-level A matrix in state-space domain
$[B_v]$	Aeroelastic vehicle-level B matrix in state-space domain
$[C_v]$	Aeroelastic vehicle-level C matrix in state-space domain
$[D_v]$	Aeroelastic vehicle-level D matrix in state-space domain
$[C]$	Global damping matrix
$[G]$	Spline Matrix
$[D]$	Parametric matrix of RFA
$[I]$	Identity Matrix
$[M]$	Global mass matrix
$[R]$	Aerodynamic lag roots
$[W]$	Weighting factor
$[E]$	Parametric matrix of RFA
$[\bar{M}]$	Generalized mass matrix
$[K]$	Global stiffness matrix
$[\bar{K}]$	Generalized stiffness matrix
$[Q]$	Generalized aerodynamic force
$[Q_{hh}]$	Generalized aerodynamic force matrices due to structural modes
$[Q_{hc}]$	Generalized aerodynamic force matrices due to control surfaces
$[\tilde{Q}]$	Approximated $[Q]$ with RFA
$[\tilde{Q}_{hh}]$	Approximated $[Q_{hh}]$ with RFA
$[\tilde{Q}_{hc}]$	Approximated $[Q_{hc}]$ with RFA

CHAPTER 1

INTRODUCTION

1.1 Background to the Study

1.1.1 Aeroelasticity

There has been comprehensive amount of work in recent years to model and analyze aeroelastic response of the aircraft while planes are getting lighter due to fuel efficiency requirement and more agile aircraft demand. Nowadays, it is essential to estimate the aeroelastic response of aircraft during preliminary design phases in order to prevent weight penalties and to escape flutter or catastrophic structural failure.

The improvements in aerospace and materials industry made aircraft lighter day after day resulting in more flexible aircraft. Flexible aircraft are prone to flutter or limit cycle oscillation (LCO) type sustained oscillations due to the coupling of unsteady aerodynamics and structural vibrations and unpredictable structural failures may be encountered.

1.1.2 Aeroservoelasticity

Further improvements in aircraft resulted in the development of fly-by-wire airplanes. For more agile aircraft design to minimize the pilot errors and to increase the comfort of passenger and the flight crew, fly-by-wire aircraft became more popular nowadays. In fly-by-wire aircraft, control surfaces are driven by actuators powered by electricity, hydraulic system, or both. Although actuators facilitate to

overcome the loads on control surfaces, complexity of the flight control system is increased. Therefore, flight control computers accompany pilots.

Flight control computer requires an integrated flight control algorithm which controls the aircraft motion by deflecting the control surface through actuator commands and stabilizes the aircraft. The flight control algorithm can interfere with the aeroelastic behavior of the aircraft, because both the control surfaces and the main structures to which flight control surfaces are attached to are flexible. The interaction of aerodynamics, flexible structural response and the control algorithm is the field of ASE which is studied in this thesis.

The aeroservoelastic phenomenon is getting more popular because of the increased number of fly-by-wire aircraft. Aeroservoelastic behavior of the fly-by-wire aircraft must be investigated since the flight control algorithm can be easily coupled with aeroelastic behavior of the aircraft causing catastrophic failure. Although inhibiting the instability of the aeroelastic system results in weight penalty, in the field of aeroservoelasticity (ASE), the most convenient way of inhibiting the aeroservoelastic instability is to use structural coupling filters such as notch, low-pass and Kalman filters. It is worth to mention that these filters induce lags on the flight control algorithm and if they are not planned during the preliminary design phase of the aircraft, it can urge the budget of the flight control algorithm.

1.1.3 Nonlinear Aeroservoelastic Analysis

With the increasing complexity of the aeroservoelastic response of the aircraft, the solution fidelity of linear aeroservoelastic analysis decreased; moreover, nonlinearity associated with the aeroservoelastic behaviour of the aircraft can only be analyzed with nonlinear aeroservoelastic analysis, such as limit cycle oscillations due to freeplay of the control surfaces. Therefore, including the nonlinearity in analysis is necessary. However, conducting nonlinear analysis in ASE is not a straightforward process as in other aerospace and engineering fields. It requires substantial workload

to define, model and analyze the system. Moreover, validating the aeroservoelastic behavior of the aircraft by experimental test is not a budget-friendly method since it requires flight tests which are very dangerous to conduct. Therefore, analysis of the nonlinear aeroservoelastic behavior of the aircraft using a model based solution is studied more and more in the literature.

1.2 Objective of the Thesis

The objective of the thesis is to present a nonlinear aeroservoelastic analysis methodology of aircraft with control surface freeplay and to investigate the nonlinear dynamic behavior of the aircraft which has different control surface freeplays at the same time.

1.3 Scope of the Thesis

In this study, nonlinear aeroservoelastic behaviour of aircraft due to freeplay nonlinearity is investigated in four sub-sections: structural dynamics, aerodynamic, aeroelastic and nonlinear aeroservoelastic modelling and analysis.

Chapter 2 is devoted to the literature survey about the nonlinear ASE. Historical and recent developments are presented. Since the scope of this study is investigating the nonlinear ASE, literature survey mainly focuses on nonlinear ASE topics rather than on unsteady aerodynamics and aeroelasticity.

Chapter 3 is dedicated to the structural dynamics modelling of the very light aircraft that is investigated in this thesis. Details of the global FE model of the aircraft including the control surfaces are given. Modal analysis of the aircraft is conducted, and mode shapes and natural frequencies are obtained. Mode shapes and associated frequencies are used as the base structural dynamic model in the following sections.

Chapter 4 describes the aerodynamic modelling which is used in the aeroelastic and the related analysis. Based on the computational fluid dynamic (CFD) model, high

fidelity aerodynamic model is created. Classical aerodynamic influence coefficient (AIC) matrices are stored and then they are transformed into state-space domain via the Rational Function Approximation (RFA). In order to decide on the least square fit methodology, Roger's and Minimum State methods are compared and it is decided to use the Roger's method since it showed better approximation.

Chapter 5 gives the details on the open-loop response of the aircraft which basically excludes the control algorithm. In order to obtain the aeroelastic model, spline methodology which is the coupling of the structural model with the aerodynamic model, is explained. Spline verification results and details of the aeroelastic analysis of the aircraft are given.

Chapter 6 presents the modelling and analysis of the linear and nonlinear aeroservoelastic phenomenon. Firstly, actuator dynamics model is introduced. Then, static aeroelastic analysis is performed in order to obtain rigid body stability derivatives which are used in a simple flight control algorithm design. Control surface freeplay and fictitious mass implementations are described. Lastly, time marching nonlinear aeroservoelastic analyses of the aircraft are conducted for different control surface freeplay input. Finally, results are presented.

The general conclusions and future work recommendations for this study are given in Chapter 7.

1.4 Limitations of Study

Primary limitations of the study are:

1. Real very light aircraft that is studied in this thesis does not have any sensor, servo-actuator and flight control algorithm system. Therefore, implementation of them in the study is completely artificial.

2. For the very light aircraft studied, rigid body aircraft stability coefficients and derivatives are not available. In order to model the aeroservoelastic behaviour of the aircraft, they are obtained using a rather inconvenient way.

3. In the nonlinear aeroservoelastic analyses performed, aircraft is assumed to be always in the level flight condition. No maneuver condition is considered in this study.

CHAPTER 2

LITERATURE REVIEW

2.1 Introduction

This chapter presents the literature survey regarding the nonlinear aeroservoelastic analysis due to freeplay motion on the control surfaces with the fictitious mass approach. Firstly, latest advances and progresses on the field of ASE are summarized. Then, the work done on the effect of freeplay on the aeroservoelastic behaviour of aircraft is discussed. Specifically, work performed with and without fictitious mass approach is emphasized. Finally, recent improvements on nonlinear aeroservoelastic analysis are explained.

2.2 Aeroservoelasticity

Aeroelasticity (AE) is an interesting and complex phenomenon where inertial forces, the elasticity of the aircraft and aerodynamic forces and moments couple with each other [1]. During the design phase of an aircraft, it is inevitable to study this phenomenon in order to prevent expensive costs like time, weight penalties and failure of the aircraft or sub-structure [2]. While the technology on the control of aircraft improved in order to make the aircraft more agile and comfortable, a different phenomenon, ASE, has appeared. ASE involves the coupling of the flight control algorithm and aeroelastic behavior of the aircraft [3]. It is necessary to investigate the aeroservoelastic behavior of the aircraft in order to prevent catastrophic failure due to instabilities related with ASE.

First formal ASE studies started with the highly maneuverable fighters such as the Lockheed F-16, the McDonnell Douglas F/A-18 and some of civil transport aircraft which are all built with automatic flight control system in the early 1970s [4]. In order to fly beyond the open-loop flutter speed in these agile aircraft, passive flutter suppression systems were developed by Abel et. al. in the late 1970s [5],[6]. This first passive flutter suppression system and likewise the first aeroservoelastic studies were based on changing the closed-loop characteristic of the aircraft with respect to the inputs of the sensors which measure also the structure response of the wing.

Followingly, in order to build active flutter suppression system, the time domain representation of the aeroelastic model which is based on the frequency domain was required. To be able to do that, Dunn [7] presented the unsteady aerodynamic forces in the time domain by Padé approximation in 1980 and Karpel [8] has discussed several rational function approximation methods and offered the “minimum-state” approximation in 1981.

The other improvements in ASE were related with other flight regimes such as separated and transonic-induced flows. The Theodorsen [9] model of the representation unsteady oscillatory aerodynamic has been used up to present. This method is based on linearized small-disturbance and potential aerodynamic model with a harmonic motion assumption for wing-like surfaces. Therefore, during the time domain representation it can be directly used, and transfer matrix of aerodynamic model can be employed. However, this method is not applicable for separated and transonic flows since they are highly nonlinear. Edwards et. al. [10] reviewed the transonic unsteady aerodynamics and their application on aeroelasticity. They have studied the implementations of Navier-Stokes equations for unsteady aerodynamics for high speed flow fields that have low angle of attack and low speed flow fields with high angle of attack. Later, Raveh [11] presented a novel approach on modeling unsteady aerodynamic forces based on Computational Fluid Dynamics (CFD) input-output data for subsonic separated flows. On the other

side, for the transonic regime, transonic small-disturbance (TSD) model has been used and widely accepted in the aeroelasticity field [12].

Although there are several studies on unsteady aerodynamic models in the literature, ASE has inherent uncertainties. Therefore, the flight control algorithm should be robust to compensate these uncertainties in ASE and it should be adaptive. While using high gains in linear feedback theory in flight control algorithm provides robustness, it degrades the performance of the control algorithm at higher frequencies. Therefore, various linear feedback theories such as linear quadratic Gaussian (LQG) [13], H_2/H_∞ control [14] and structured singular value synthesis [15] were proposed to this dilemma.

2.3 Fictitious Mass Approach

In 1975, fictitious mass approach was firstly presented by Karpel et al. [16] in the form of component mode synthesis, where the natural modes of separate structural components are combined for the natural modes of the combined structure. Then, this method was employed to represent modal coordinates of structural modal with large local structural variations in aeroelastic analysis [17]. In this study, they have suggested to formulate time domain aeroelastic equations in state-space model by using small number of generalized coordinates. Then Karpel and Raveh improved the accuracy and efficiency of this technique on modal-based structural analysis [18]. Next, Karpel and Wieseman [19] have used this technique to obtain time domain solution of flutter equations with large stiffness change. In this study, a nominal finite element model is modified with a large fictitious mass which was located on the area of the structural change, and natural mode shapes and frequencies were obtained. Then, separating a subset of these modes at lower frequencies, a set of structural modal coordinates is obtained and used in time domain flutter analysis. The main point of this study was representing the local structural changes such as freeplay without changing the modal coordinates directly and consequently analysis time has been reduced enormously.

2.4 Freeplay Implementations

In the theoretical study of freeplay, the mathematical modeling of freeplay nonlinearity is the first important subtopic. There are several mathematical studies to represent freeplay motion in aeroelastic analysis in the literature. Fundamental approach is idealized and piecewise model of freeplay if there is not any available freeplay test data [20]. In this method, same value of rotational stiffness coefficient has been assumed outside the freeplay regions and inside the freeplay region, control surface rotational stiffness is taken as zero. However, since this approach is discrete at the freeplay zone boundaries, it is a non-smooth freeplay model which introduces discontinuity. Dimitriadis [20] offered an alternative approach which utilized the restoring moment concept, and this approach is used in this study. Pereira et al. [21] introduced a freeplay implementation in which hardening effect of the nonlinearity is modeled via rational polynomial function and freeplay model is represented by hyperbolic functions. With this approach, the discontinuity on freeplay model was avoided and therefore undesired aeroelastic responses mitigated.

Another approach in the literature is the equivalent linearized stiffness approach. Anderson and Mortara [22] have used this method based on the freeplay test data. In this study, they have compared the freeplay analysis results utilizing the equivalent linearized stiffness approach with the maximum freeplay observed in flight test and stated that equivalent linearized stiffness implementation is a conservative approach. Other approach in the literature is based on assuming the freeplay region as nonlinear and non-constant. Vasconcellos et al. [23] stated nonlinear effect of the freeplay can cross the freeplay region of the control surfaces. Therefore, a third order polynomial is assigned in order to represent the cubic hardening or softening behavior of the nonlinearity.

Danowsky et al. [24] and He et al. [25] utilized the describing function approach to model freeplay nonlinearity in aeroelastic analysis. Danowsky et al. used analytical

solution to solve the aeroservoelastic problem and He et al. utilized the harmonic balance method.

2.5 Nonlinear Aeroservoelastic Analysis

The backlash of the control surface actuation systems and manufacturing tolerances leads to control surface freeplay, which is a nonlinear event and couples with the aeroservoelastic model and consequently flutter instability and limit cycle oscillations (LCO) may occur. Therefore, the study of nonlinear dynamic behavior of an aeroservoelastic system is crucial to prevent probable instability occurrences and sustained oscillation type system responses.

The effects of including freeplay in the nonlinear dynamics system behavior were started to be investigated in the 1950s [26]. From then, designers of military and civil aircraft have been dealing with minimizing the freeplay effects and their maintenance costs and also designing aircraft free from any aeroelastic and also aeroservoelastic instabilities. Hoffman et al. [27] conducted the first full scale experimental tests for different freeplays in a wind tunnel in 1954. Then, Woolstan et al. [28] and Shen [29] introduced the first theoretical studies on the freeplay problem. In 1999, Lee et al. [30] investigated the modelling and solutions of nonlinear aeroelastic analysis for different type of structural and aerodynamic nonlinearities. Tian et al. [3] also investigated the nonlinear aeroservoelastic analysis but with a reduced model in order to improve computational efficiency by using the component mode synthesis technique. As progress is made in the computational capabilities and experimental studies, understanding solutions in aeroservoelastic problems involving freeplay and consequently its nonlinear behavior became simpler.

Although nonlinear aeroelasticity is popular topic in the literature, there are few studies about the nonlinear aeroservoelastic analysis due to control surface freeplay by using the fictitious mass approach. The first study related with nonlinear

aeroservoelastic analysis due to freeplay was introduced in 2007 by Gold et al. [31]. In this study, they used a reduced order ASE model with the fictitious mass approach to model nonlinear actuator stiffness. In order to prevent limit-cycle oscillations, a nonlinear control strategy is presented for an unmanned air vehicle (UAV). In 2013, Huang et al. [32] performed nonlinear aeroservoelastic analysis due to structural nonlinearity for a controlled multiple actuated-wing model by using the FM approach. In this study, linear flutter control system was utilized, and they have examined the nonlinear dynamic effects of the freeplay on the linear flutter control algorithm. Karpel et al. [33] investigated the effect of nonlinear structural elements on the aeroservoelastic behaviour by using the full span stick model of the aircraft. They have utilized a linear ASE model in the frequency domain analysis and a nonlinear feedback controller in time-marching analysis and they observed limit-cycle oscillations due to actuator nonlinearities. As a continuation of this study, Roizner et al. [34],[35] conducted a parametric flutter margin analysis by using the same structural and the aerodynamic model for linear and nonlinear stability margins.

In the literature, to the best of the knowledge of the author of this thesis, the effect of simultaneous freeplay in different control surfaces on the limit cycle oscillation behaviour at the aircraft level has not been studied. In this thesis study, the effect of simultaneous aileron-elevator freeplay on the nonlinear aeroelastic behaviour of the aircraft is studied, and the significant effect of simultaneous aileron-elevator freeplay on lowering the LCO speed compared to elevator freeplay only is shown. It is believed that including the investigation of two different control surface freeplay at the same time in terms of nonlinear aeroservoelastic behaviour of the aircraft is a contribution of the thesis study to the literature. Moreover, a part of this study is presented in TOK 2022 (*Otomatik Kontrol Türk Milli Komitesi Ulusal Kongresi*) and published in the proceeding of the conference [36].

CHAPTER 3

STRUCTURAL MODELLING OF THE VERY LIGHT AIRCRAFT

3.1 Introduction

This chapter is dedicated to the development of the structural finite element model of the very light aircraft that is used as the platform to demonstrate the nonlinear aeroservoelastic modelling and analysis involving freeplay of control surfaces. Commercial package programs MSC.Patran® and MSC.Nastran® programs are utilized during modelling and analysis processes, respectively. In order to obtain modal domain results, which is used as the structural model in aeroelastic analysis, MSC.Nastran® SOL 103 solution sequence is executed. In this chapter, firstly finite element model of the aircraft is introduced, then the governing equation of the motion is given.

The results of the modal are a set of eigenvalues and eigenvectors, which represent the dynamic behavior of the aircraft. These eigenvalues and eigenvectors of the system correspond to the frequencies of the vibration modes and mode shapes, respectively. The combination of modal frequencies and mode shapes is adequate to represent the dynamic system behavior or aeroelastic response since these analyses are also conducted in the frequency domain.

3.2 General Coordinate System

The general coordinate system used in this study is given in Figure 3.1. The origin of this coordinate system is at the frontmost nose point of the aircraft. x axis points aft, y axis points in the direction of the right wing and z axis points upwards.

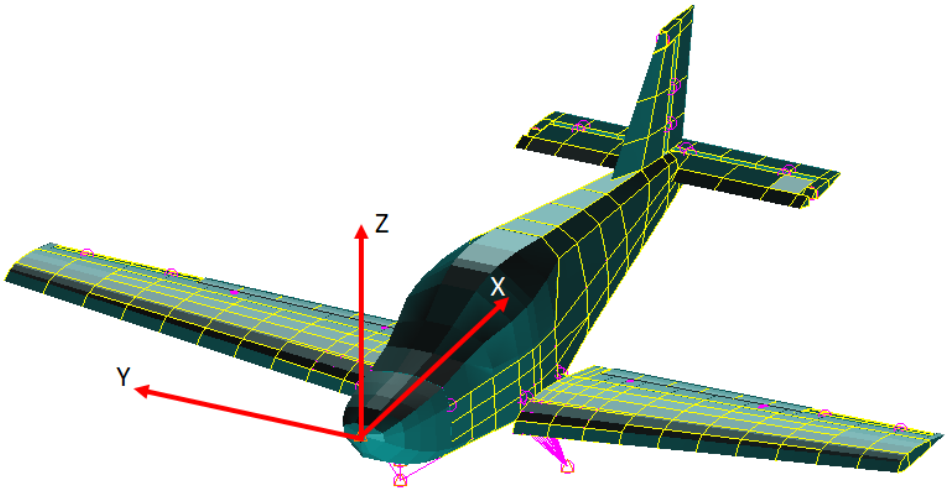

Figure 3.1 General Coordinate System

3.3 Finite Element Model Representation

The global Finite Element Model (GFEM) of the aircraft is shown in Figure 3.2 - 3.4. The GFEM is constructed by FE models of primary structural elements of the aircraft such as fuselage frames, wing ribs, spars etc., and the aim of using GFEM is to represent the global aircraft structure behaviour while providing affordable computational time by using less memory.

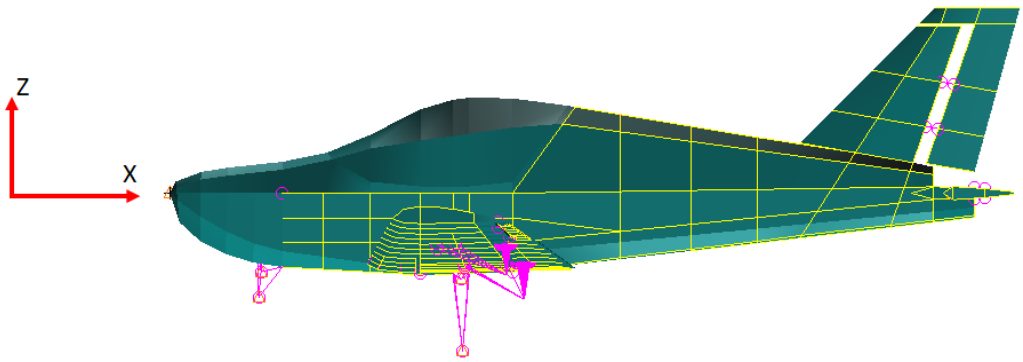

Figure 3.2 Side View of the Finite Element Model of the Aircraft

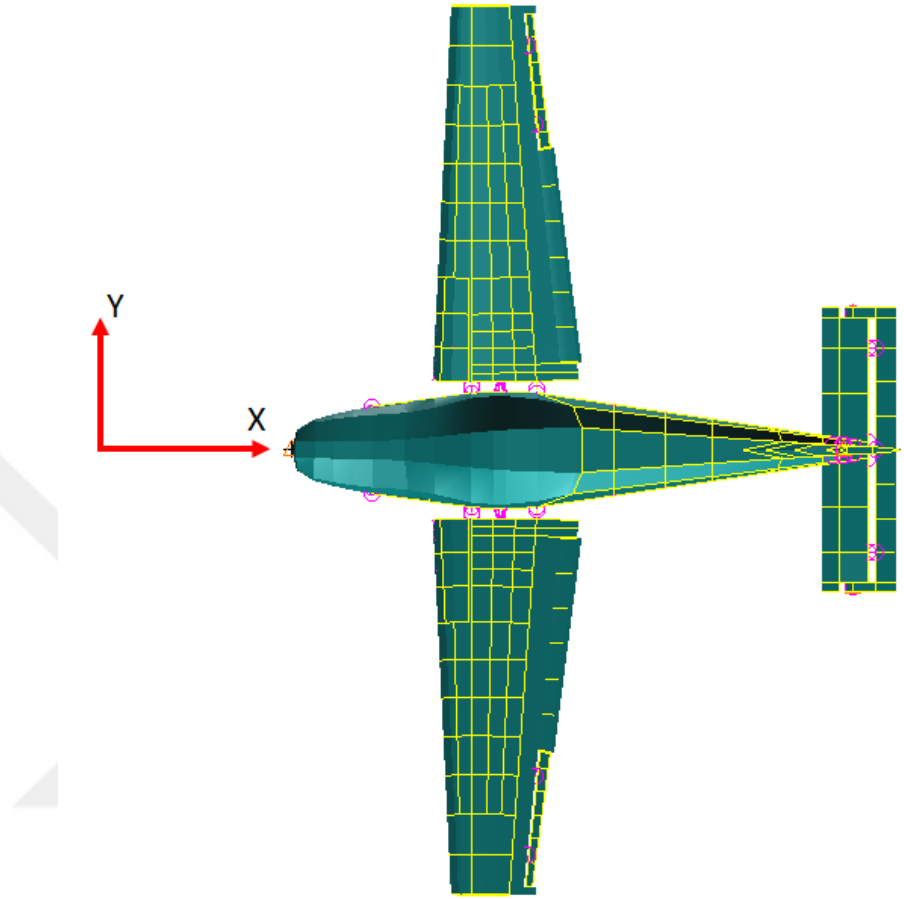

Figure 3.3 Top View of the Finite Element Model of the Aircraft

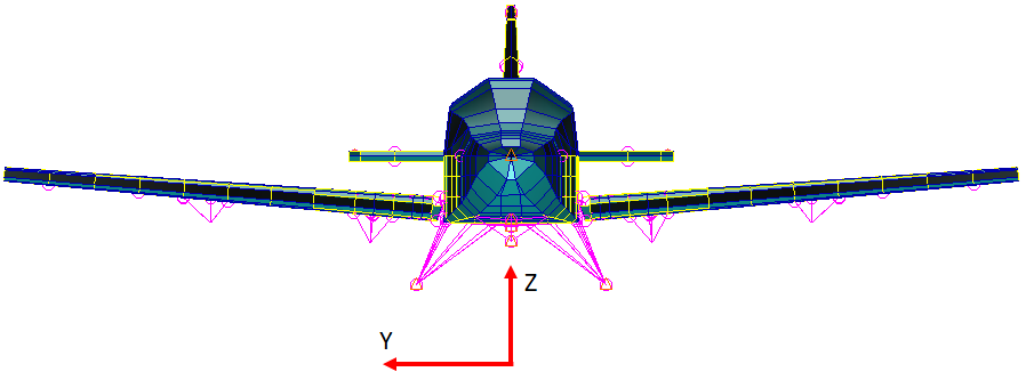

Figure 3.4 Front View of the Finite Element Model of the Aircraft

The GFEM of the aircraft consists of fuselage, wing, vertical tail, horizontal tail, and control surfaces: ailerons, elevator, and rudder. The number of elements used in the structural finite element model are given in Table 3.1.

Table 3.1 Number of Elements used in Structural Model

Element Type	Element Name In MSC Nastran	Element Description	Number of Elements
1-D Bar	CBAR	Simple Beam Element	52
1-D Bar	CBEAM	Beam Element	28
0-D Bar	CBUSH	Spring/Damper Element	9
0-D Mass	CONM2	Concentrated Mass Element	17
2-D Shell	CQUAD4	Quadrilateral Plate Element	58215
1-D Bar	CROD	Rod Element	3767
2-D Shell	CTRIA3	Triangular Plate Element	135
1-D Rigid	RBE2	Rigid Link Element	32
1-D Rigid	RBE3	Interpolation Constraint Element	17

The CBAR, CBEAM and CROD elements represent 1-D bar, beam and rod structures of the aircraft, respectively. CBUSH elements are used to represent the spring and local stiffness in the connections on the aircraft, such as actuator stiffness. CONM2 elements are concentrated mass elements such as equipment of aircraft or pilot weight. CQUAD4 and CTRIA3 elements are used to model 4-noded quadrilateral and 3-noded triangular thin shell structures like the skin of the aircraft, respectively. RBE2 and RBE3 are the rigid body elements which are employed on rigid links and interpolation constraint elements.

In this study, the CROD type of finite element members are utilized to model symmetric and constant cross-sectional flanges of spars and ribs, and also frames of the aircraft since these structures and also their finite element representation carries

only axial and torsional loads [37]. The location of these type of elements in FE model presented in Figure 3.5.

The CTRIA3 and CQUAD4 type elements are used to simulate thin shell plate components of the aircraft such as skin. These types of elements carry in-plane force, moments and shear forces [37]. Therefore, they are used to model the skin plates of the aircraft and they are shown in Figure 3.6.

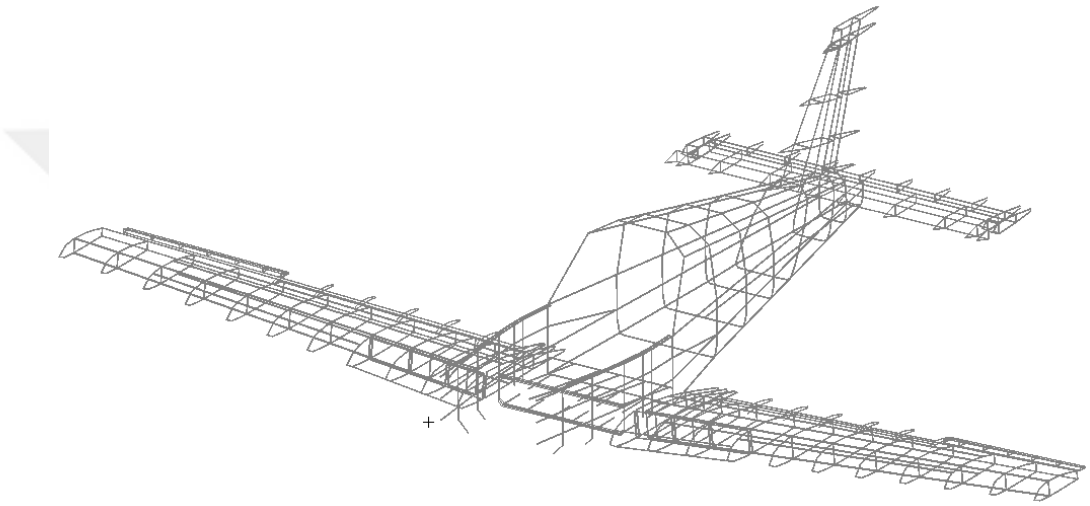

Figure 3.5 CROD Elements in the FE Model of the Aircraft

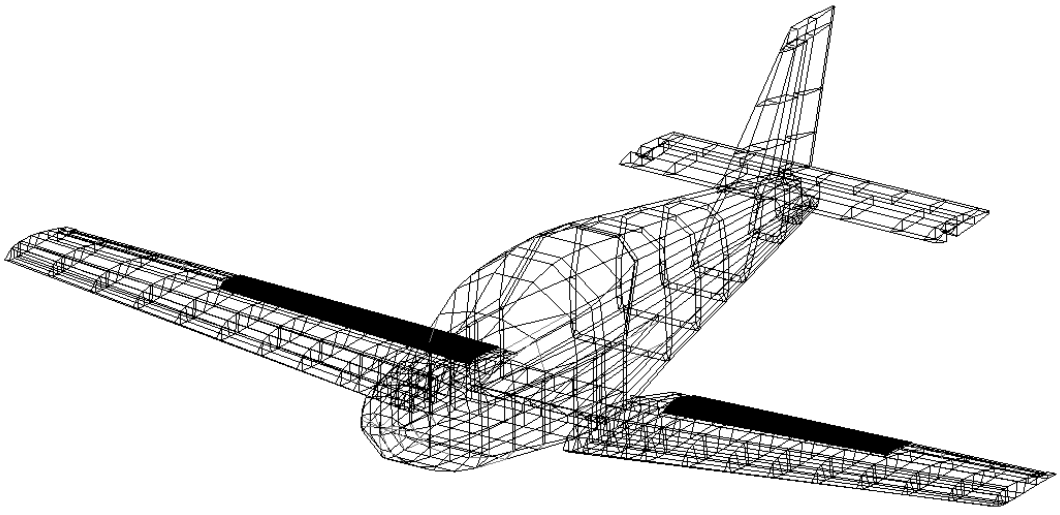

Figure 3.6 CQUAD4 and CTRIA3 Elements in the FE Model of the Aircraft

The CBEAM element type is the comprehensive version of the CROD which can also carry transverse shear forces, bending moments and cross-sectional warping loads [37]. On the other hand, CBAR element type has same properties with the CBEAM except the cross-sectional warping loads. In this study, CBEAM and CBAR type of elements are used to model complex geometries with varying cross-sectional areas such as engine mounts and wing-fuselage connection parts since these areas are exposed to relatively large amounts of force and moment than other parts of the aircraft and it requires a comprehensive modelling in order to represent the static and dynamic behaviour of the aircraft better. The locations of the CBEAM and CBAR elements are presented in Figure 3.7.

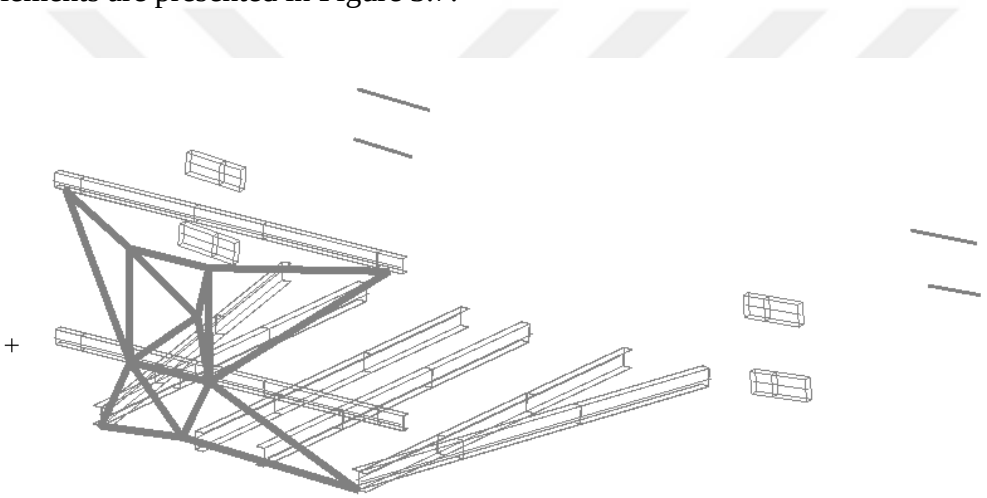

Figure 3.7 CBEAM and CBAR Elements in the FE Model of the Aircraft

The CONM2 element type are used to model concentrated mass such as equipments and pilots weight. These lumped mass elements are distributed to aircraft frames by of the rigid body element, RBE3, to increase the accuracy of mass distribution of the aircraft. The other rigid body element type, RBE2, is to represent a rigid connection such as hinge of the control surfaces of the aircraft as shown in Figure 3.8 and Figure 3.9. The CBUSH elements are utilized to model generalized spring type structural elements such as actuator stiffness.

Utilizing the GFEM, stiffness and mass matrices are constructed by MSC.Nastran®. Since the structural model has 57369 nodes with 6 degree of freedom per node, 3 translational and 3 rotational, the degree of freedom in the modal analysis is 344214. In other words, the constructed stiffness matrix is a square one and its size is 344214 by 344214.

The mass model of the aircraft is represented by the density of structural components and concentrated (lumped) mass elements CONM2. Lumped mass elements in the FE model are distributed to certain nodes by RBE3 elements according to the degree of freedom and the distance between the lumped element location and the node. The weight, inertia and center of gravity (CG) properties of the aircraft with respect to the general coordinate system of the structure model are given in Table 3.2.

Table 3.2 Weight and Inertia Properties of the Very Light Aircraft

Property	*Value*	*Unit*
CG in x-direction	2007.000	mm
CG in y-direction	-0.562	mm
CG in z-direction	-119.200	mm
Total Mass	714.030	kg
Inertia about XX axis	1.020 E+09	$kg.mm^2$
Inertia about XY axis	6.610 E+05	$kg.mm^2$
Inertia about YY axis	9.752 E+08	$kg.mm^2$
Inertia about XZ axis	5.757 E+07	$kg.mm^2$
Inertia about YZ axis	1.843 E+05	$kg.mm^2$
Inertia about ZZ axis	1.816 E+09	$kg.mm^2$

Using MSC.Patran®, finite element model is created by assigning proper material properties like elastic modulus, Poisson ratio and density etc. Therefore, necessary

information to generate the mass and stiffness matrices in the structural dynamic model is determined. Mass and stiffness information is the input of the modal analysis which is conducted by using MSC.Nastran®. Using the mass information given in Table 3.2 and the stiffness information according to the properties of the elements, MSC.Nastran® creates the global mass and stiffness matrices firstly. Then, it solves the eigenvalue problem which is given in the following section and the modal domain results are obtained.

3.4 Control Surface Actuator Stiffness Implementation

In order to use the finite element model of the aircraft structure in nonlinear aeroservoelastic analysis, rotational stiffness of control surfaces about their hinge axes must be controlled. The aim of this is to gain ability to control and change the control surface stiffness in the freeplay region. Outside the freeplay region, control surfaces have their own stiffness, and they have modal frequencies depending on their inertia about their hinge axes. The diagrammatic representations of the aileron and rudder actuator stiffness implementation are given in Figure 3.8 and Figure 3.9. In Figure 3.8, the left coincident node of the CBUSH element is connected to spar of the wing by RBE2 element and right coincident nodes of this spring element is connected to front spar of the aileron. CBUSH element, which is a type of spring element in FE modelling, ensures the translational and rotational stiffness of the aileron on the hinge axis whereas RBE2 element provides a rigid body connection between the hard points of the main surfaces, such as spars, and the corresponding nodes of the CBUSH element. In a way, RBE2 elements simulate the arms of the servo actuators.

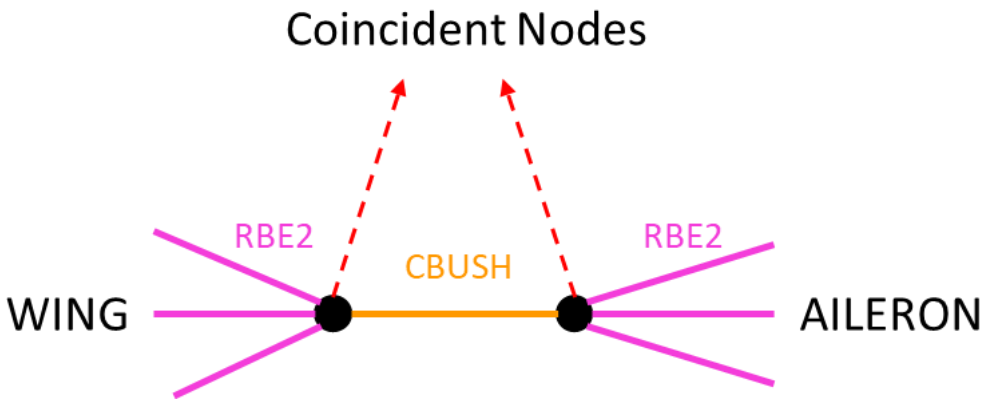

Figure 3.8 Diagrammatic Representation of Aileron Stiffness

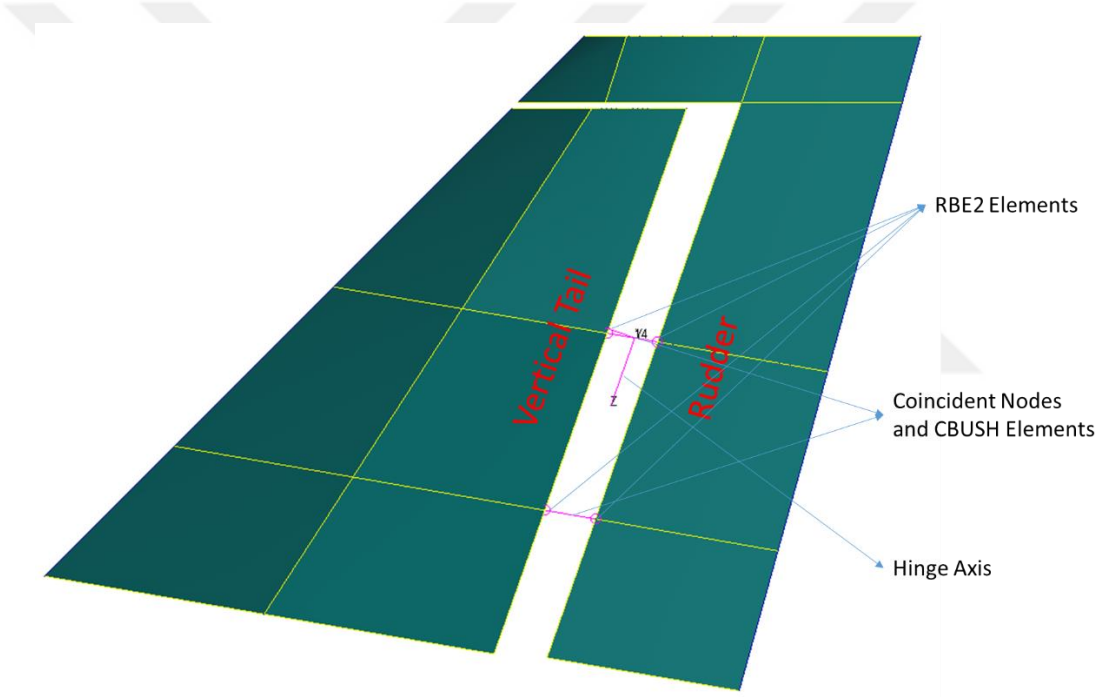

Figure 3.9 Representation of Rudder Stiffness on GFEM

In Figure 3.9 the coincident nodes are placed at the hinge axis of rudder, and these nodes are connected the rudder and vertical tail by rigid body element RBE2. The bush element between the coincident nodes represents an artificial spring element which is called as CBUSH element in MSC.Nastran®.

The property of the CBUSH element is assigned by the PBUSH bulk data card and by changing the stiffness values about the three translational and three rotational axes one can control the nonlinear stiffness of the control surfaces. Except the rotational stiffness about the hinge axis which corresponds to z axis in Figure 3.9, all stiffness values are assigned very high values indicating rigid connection about the axes except for the z axis rotational stiffness. The stiffness values of the control surface about their hinges are chosen by a trial-error procedure by considering the decoupling of control surface natural frequencies from other mode shapes and ensuring that none of the control surface modes has a flutter instability within the flight regime in the open-loop aeroelastic analysis. The stiffness values are given in Table 3.3 where TX, TY and TZ correspond to translational stiffness along the x, y and z axes, respectively and RX, RY and RZ correspond to rotational stiffness values about x, y and z axes, respectively. It should be noted that RZ corresponds to hinge axis rotational stiffness for all control surfaces.

Table 3.3 Control Surface Stiffness Values

	TX [N/m]	*TY [N/m]*	*TZ [N/m]*	*RX [Nm/rad]*	*RY [Nm/rad]*	*RZ [Nm/rad]*
Ailerons	1.00 E+6	1.00 E+6	1.00 E+6	1.00 E+6	1.00 E+6	1.00E+2
Elevator	1.00 E+6	1.00 E+6	1.00 E+6	1.00 E+6	1.00 E+6	1.50E+3
Rudder	1.00 E+6	1.00 E+6	1.00 E+6	1.00 E+6	1.00 E+6	2.30E+3

3.5 Governing Equation of Motion of the Dynamic Model of the Aircraft

The governing equation of motion of the multi degree of freedom dynamic system without any force input is represented as,

$$[M]\{\ddot{h}(t)\} + [C]\{\dot{h}(t)\} + [K]\{h(t)\} = \{0\} \tag{3.1}$$

where $\{h(t)\}$ is the displacement vector, $[M]$, $[C]$ and $[K]$ are the global mass, damping and stiffness matrices respectively. In this equation, vector size is n_{total} x 1 and size of the matrices are n_{total} x n_{total} where n_{total} is total number of degrees of freedom in the finite element model. Since acquiring precise damping of the structural model is not easy, to simplify the governing equation damping is not included in the structural analysis. Then, governing equation becomes as given in Equation (3.2).

$$[M]\{\ddot{h}(t)\} + [K]\{h(t)\} = \{0\} \tag{3.2}$$

Assuming harmonic solution using Equation (3.3),

$$\{h(t)\} = \{\tilde{h}\}e^{i\omega t} \tag{3.3}$$

Equation (3.2) can be expressed as in Equation (3.4).

$$-\omega^2[M]\{\tilde{h}\}e^{i\omega t} + [K]\{\tilde{h}\}e^{i\omega t} = \{0\} \tag{3.4}$$

Finally, the equation motion of the dynamic system can be expressed as an eigenvalue problem given by Equation (3.5).

$$[K - \omega^2 M]\{\tilde{h}\} = \{0\} \tag{3.5}$$

For non-trivial solution of Equation (3.5), determinant of the coefficient matrix must vanish.

$$\det|[K - \omega^2 M]| = \{0\} \tag{3.6}$$

The solution of Equation (3.6) yields eigenvectors and eigenvalues which correspond to mode shapes and mode frequencies.

3.6 Mesh Independence Study

Mesh independence study is conducted in order to determine dependence of the results on the mesh fidelity. For this purpose, bar elements (CBAR, CBEAM and CROD elements), and shell elements (CQUAD4 and CTRIA3 elements) are refined with multiplication factors of 2, 4 and 8, and they are given in Figure 3.10, Figure 3.11, and Figure 3.12 respectively. Necessary grid points are created according to the element type.

Modal analyses are conducted for refined models and modal frequencies obtained are listed in Table 3.4. Using the most refined model which is refined with a multiplication factor of 8 as the basis, natural frequencies are compared, and percent differences are given in Table 3.5. In this table, multiplication factors 2, 4 and 8 are denoted as x2, x4 and x8 respectively. Since differences between frequencies are negligible and the percentage of difference is very small, the nominal mesh is chosen and used in this study. It is worth to mention that frequencies of control surfaces are free from the mesh dependency study since their frequencies depend only on the spring elements in their connections as shown in Figure 3.8 and Figure 3.9.

It should be mentioned that the mass model of the nominal FE model is composed of lumped mass points and structural mass based on the density assigned to the material of finite elements. Since structural mass is based on density, this causes local modes in the refined models and one example of a local mode shape which is amplified with multiplication factor of 2 (x2) is given in Figure 3.13. In order to eliminate local modes and the effect of the inertia effect from the mesh dependency study, the mass model is modified. The details are given in Section 3.6.1.

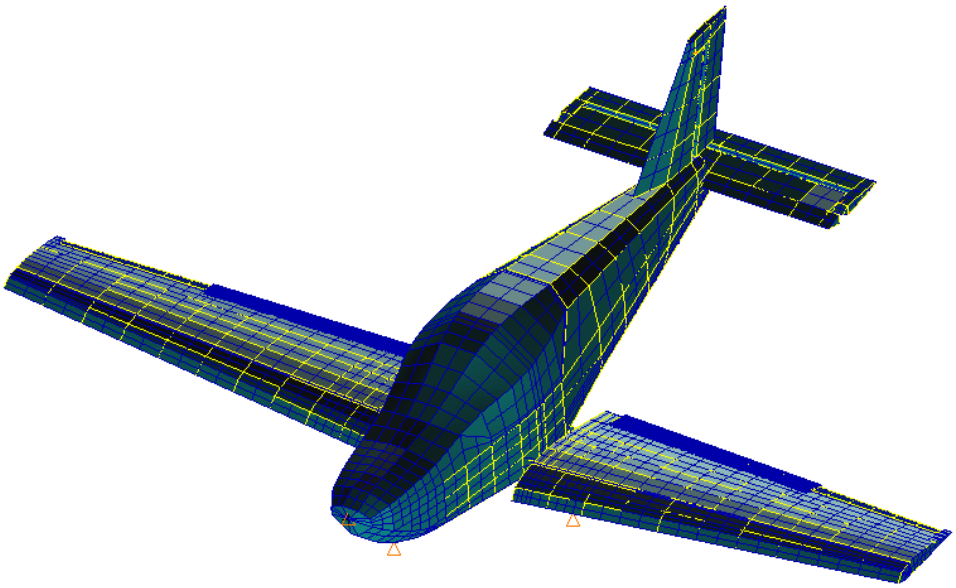

Figure 3.10 Mesh Refinement with Multiplication Factor of 2

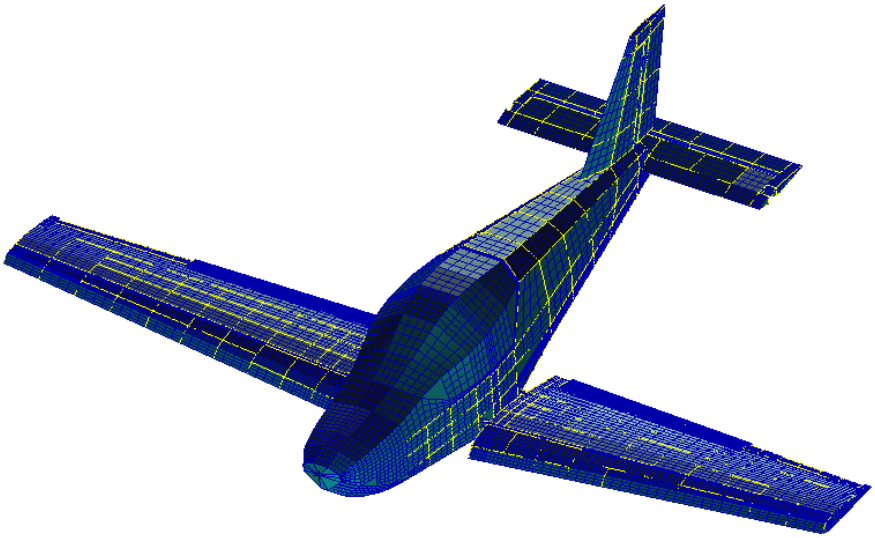

Figure 3.11 Mesh Refinement with Multiplication Factor of 4

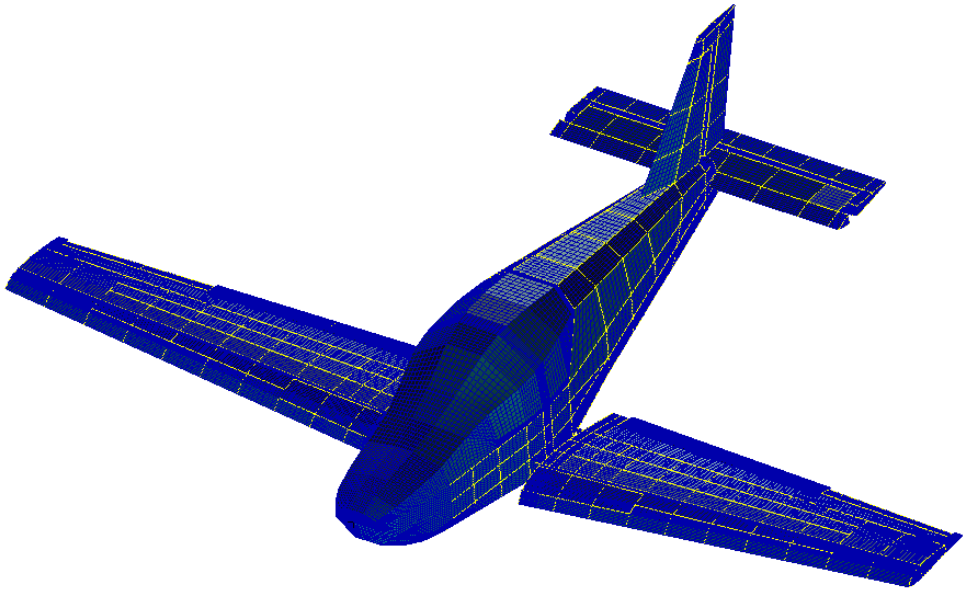

Figure 3.12 Mesh Refinement with Multiplication Factor of 8

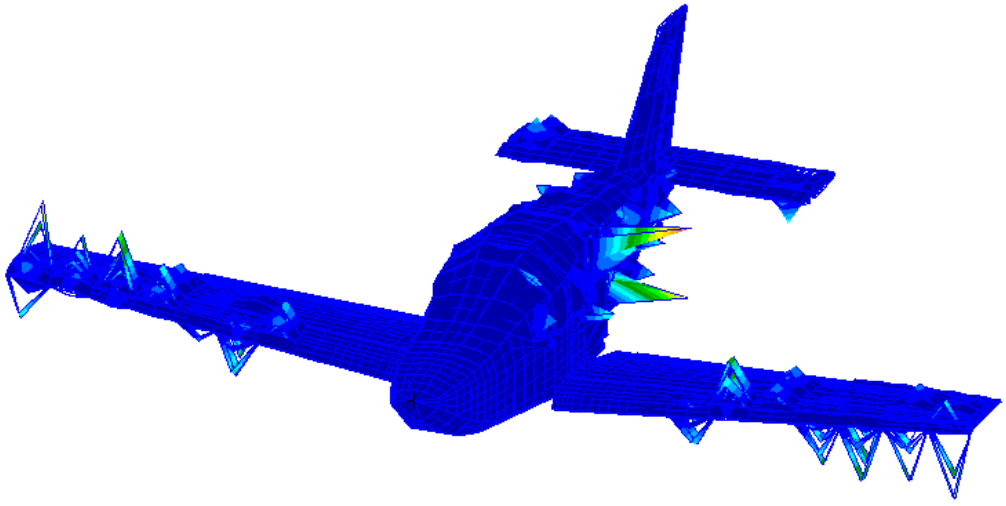

Figure 3.13 Local Mode Shape Example of the GFEM

Table 3.4 Modal Frequencies According to Mesh Density

Mode Shape #	*Frequency [Hz] (Nominal Mesh)*	*Frequency [Hz] (x2)*	*Frequency [Hz] (x4)*	*Frequency [Hz] (x8)*
1	10.328	10.217	10.209	10.205
2	18.568	18.371	18.365	18.361
3	19.476	19.476	19.476	19.476
4	20.392	20.292	20.267	20.238
5	22.083	22.083	22.083	22.083
6	23.225	23.117	23.068	23.059
7	24.624	24.357	24.255	24.223
8	24.988	24.623	24.478	24.359
9	30.414	30.236	30.118	30.095
10	32.083	32.083	32.083	32.083
11	32.120	32.120	32.120	32.120
12	33.173	32.955	32.943	32.938
13	35.974	35.186	35.155	35.146

Table 3.5 Comparison of Modal Frequencies

Mode Shape #	*Difference [%] (Nominal Mesh)*	*Difference [%] (x2)*	*Difference [%] (x4)*
1	1.2053	0.1176	0.0392
2	1.1274	0.0545	0.0218
3	0.0000	0.0000	0.0000
4	0.7609	0.2668	0.1433
5	0.0000	0.0000	0.0000
6	0.7199	0.2515	0.0390
7	1.6555	0.5532	0.1321
8	2.5822	1.0838	0.4885
9	1.0600	0.4685	0.0764
10	0.0000	0.0000	0.0000
11	0.0000	0.0000	0.0000
12	0.7135	0.0516	0.0152
13	2.3559	0.1138	0.0256

3.6.1 Inertia and Mass Modification in Mesh Refinement

The CQUAD4 elements in the nominal FE model are surrounded by CROD elements. At the corners of shell elements, grids of the bar elements are coincident with shell elements grids, so local modes are prevented. When the mesh is refined, new grids are located at the centers of shell elements in the nominal model (red dot in Figure 3.14) and since they do not have any interaction with bar elements, this causes local mode shape problem due to fact that shell elements are 2-D and they cannot resist out of plane forces [37]. In Figure 3.14, an arbitrary fuselage section is given for the nominal mesh (left) and the refined mesh with multiplication factor of 2 (right).

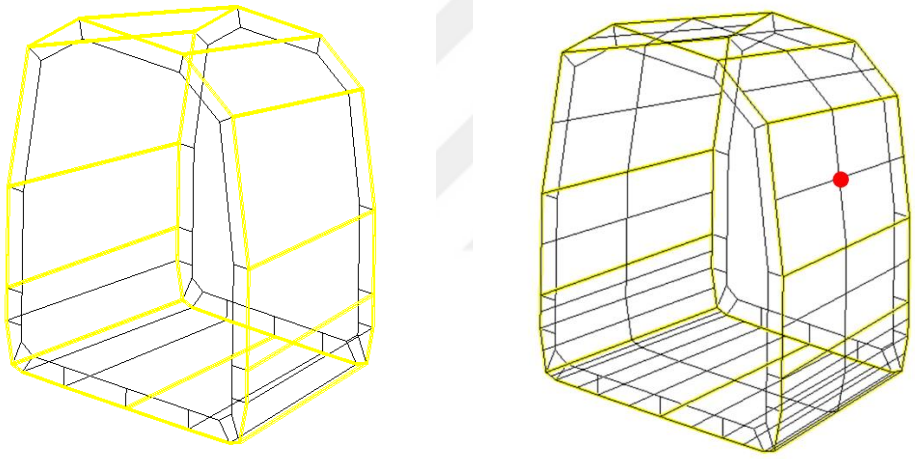

Figure 3.14 Illustration of the Grid Causing Local Mode Shape

The solution of such local mode shapes is handled using the lumped mass approach. For the fuselage section example shown in Figure 3.14, firstly, the center of gravity and the mass and inertia information only for the section involving a local mode is determined with MSC.Patran®. Then a new grid and CONM2 lumped mass element is generated at the center of gravity of the section. The properties of the CONM2 lumped mass element represent the mass and inertia information of this fuselage section. CONM2 element is connected to the grid points at the intersection of the shell and bar elements by RBE3 elements as shown in Figure 3.15. Hence, the mass

and inertia of the section is distributed to selected grid points by the RBE3 elements. Finally, the density of the elements for this section is set to zero and this process is applied to the overall aircraft. Generally, the sections are taken as between the frames in the fuselage and ribs in the wing.

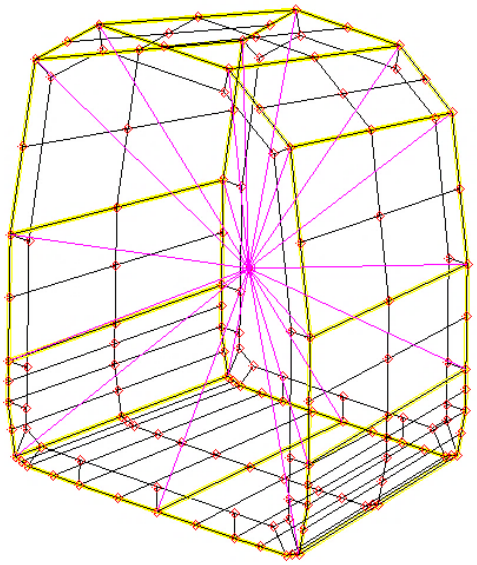

Figure 3.15 Representation of the Modified Mass and Inertia Distribution

3.7 Modal Analysis Results

The solution of eigenvalue problem given by Equation (3.6) is a set of mode shapes and frequencies. Number of frequencies and mode shapes is equal total degree of freedom of the dynamic system and structural behavior of the aircraft can be represented as a superposition of these mode shapes and frequencies. However, in terms of aeroelastic point of view, using all mode shapes and frequencies in the analysis is not convenient way due to the analysis time. The contribution of the modes with higher frequencies are less than the modes with lower frequencies. Therefore, structural dynamic behavior in aeroelastic analysis can be represented by using certain number of mode shapes and frequencies starting from the lowest ones. Ceiling frequency in order to represent dynamic response of this type aircraft is about

40 Hz [38] since higher frequencies cannot be excited by unsteady aerodynamics. The principal mode shapes and their frequencies are listed in Table 3.6 by disregarding the rigid body modes. It should be also mentioned that, given mode shapes and natural frequencies belong to nominal structural model whose mass model consists of lumped mass and density of related structural elements. Since the results of mesh independence study and consequently inertia and mass modification in mesh refinement studies show that the difference between the nominal and refined models are small and negligible, the results of nominal structural model are presented and nominal structural model is used through this study.

Table 3.6 Mode Shapes and Frequencies of the Very Light Aircraft

#	Mode Shape	*Frequency [Hz]*
1	The First Wing Bending	10.328
2	Antisymmetric Wing Bending + Fuselage Torsion	18.568
3	Rudder Rotation	19.476
4	Horizontal Tail Bending + Elevator Rotation	20.392
5	Elevator Rotation	22.083
6	Wing 2nd Bending + Horizontal Tail Rotation	23.225
7	Wing 2nd Bending + Rear Fuselage Lateral Bending	24.624
8	Wing In-plane Bending	24.988
9	Elevator Bending	30.414
10	Aileron Symmetric Bending	32.083
11	Aileron Antisymmetric Bending	32.120
12	Horizontal Tail In-plane Bending + Vertical Tail Bending	33.173
13	Vertical Tail Bending	35.974

For demonstration, wing bending mode shape is given in Figure 3.16. The other mode shapes are presented in Appendix A.

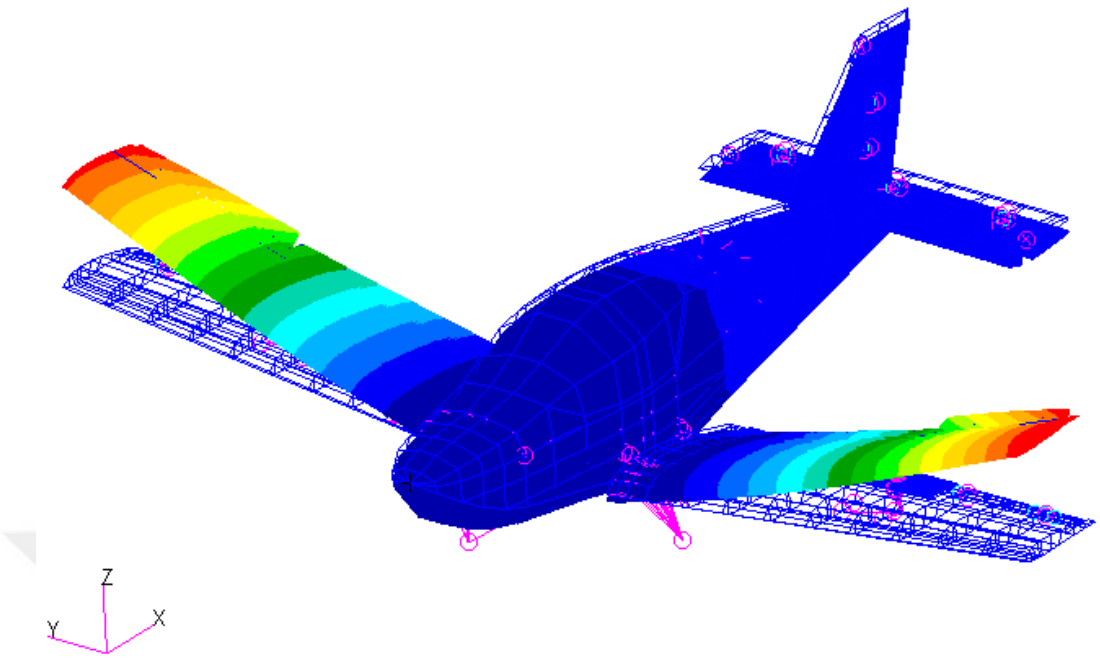

Figure 3.16 The First Wing Bending Mode Shape at 10.328 Hz

3.8 Conclusion

In this chapter, firstly finite element model of structural system is introduced. The details of GFEM of the aircraft are given and then governing equation of motion which is used in modal analysis is presented. Then a mesh independency study is conducted, and it is demonstrated that the nominal mesh fidelity has sufficient maturity to use in this study. The results of the modal analysis are given as mode shapes and frequencies.

CHAPTER 4

AERODYNAMIC MODELLING OF THE VERY LIGHT AIRCRAFT

4.1 Introduction

This chapter presents the unsteady aerodynamic force and moment calculations which are used in the aeroelastic and aeroservoelastic analyses. In order to construct the AIC matrix, which is widely used in the aeroelasticity field, a commercial software system ZAERO which is developed by ZONA Technology, Inc. is utilized.

Firstly, using the 3-D Computational Fluid Dynamics (CFD) model of the aircraft, the aerodynamic model is created. Since ZAERO does not have any user interface environment and CFD model cannot be directly used in aeroelastic analysis as an aerodynamic model, this process required serious workload.

After constructing the aerodynamic model, using ZONA6 submodule of ZAERO, AIC matrices are saved at discrete Mach numbers and for several reduced frequencies. Since computed AIC matrices are saved for once, they can be directly used in following analysis, and it reduces analysis time enormously.

Classical aerodynamic models in aeroelastic analyses are handled in frequency domain approach. In other words, the unsteady aerodynamic force and moments due to structural deformation are calculated at discrete non-dimensional frequencies named as reduced frequencies (k). However, in order to perform time-marching nonlinear aeroelastic and aeroservoelastic analysis, AIC matrices in frequency domain have to be transformed to time domain. In the thesis study, necessary transformations are made by the Rational Function Approximation (RFA) utilizing different approximations.

4.2 Unsteady Aerodynamics Modelling in ZAERO

In this part of the study, unsteady aerodynamics modelling that is used in the aeroelastic analysis is described. Aerodynamic mesh of the aircraft that is obtained by using high fidelity aerodynamic surface mesh prepared for CFD analysis in Ansys Fluent is given in Figure 4.1.

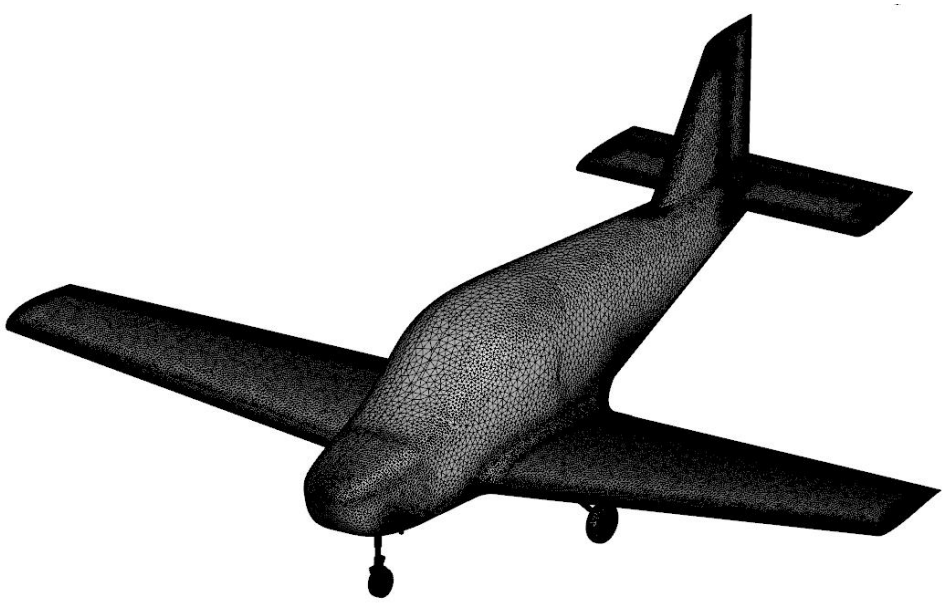

Figure 4.1 High Fidelity Aerodynamic Mesh Prepared for CFD Analysis

As it mentioned previously, the aerodynamic mesh prepared for CFD analysis cannot be directly used in aeroelastic analysis to be performed in ZAERO since the mesh is too dense for aeroelastic analysis. Therefore, using the aerodynamic mesh prepared for CFD analysis, a bunch of slices are taken through the fuselage, wings, and tails as shown in Figure 4.2, in order to construct the aerodynamic mesh be used in aeroelastic analysis. With the help of these slices, the points on wing-like elements and arbitrary body cross sections are determined and a MATLAB® code with graphical user interface is utilized by importing these slices and points as an input. The aim of using slices rather than the solid model in this code is nothing but for simplicity. For instance, in the wing of the aircraft, with the slices, the CFD nodes

intersecting with the slices can be easily determined, and these slices can be used to build the aerodynamic mesh to be used in aeroelastic analysis. Slices at the root and tip of the wing are shown in Figure 4.2. The middle slice through wing in this model is at the edge of the aileron, hence aileron meshes are separated from the wing model and control surface aerodynamic panels are easily defined. This MATLAB® code also generates the bulk data cards of aerodynamic mesh of the aeroelastic model such as CAERO7, BODY7. The aerodynamic model which is created is given in Figure 4.3.

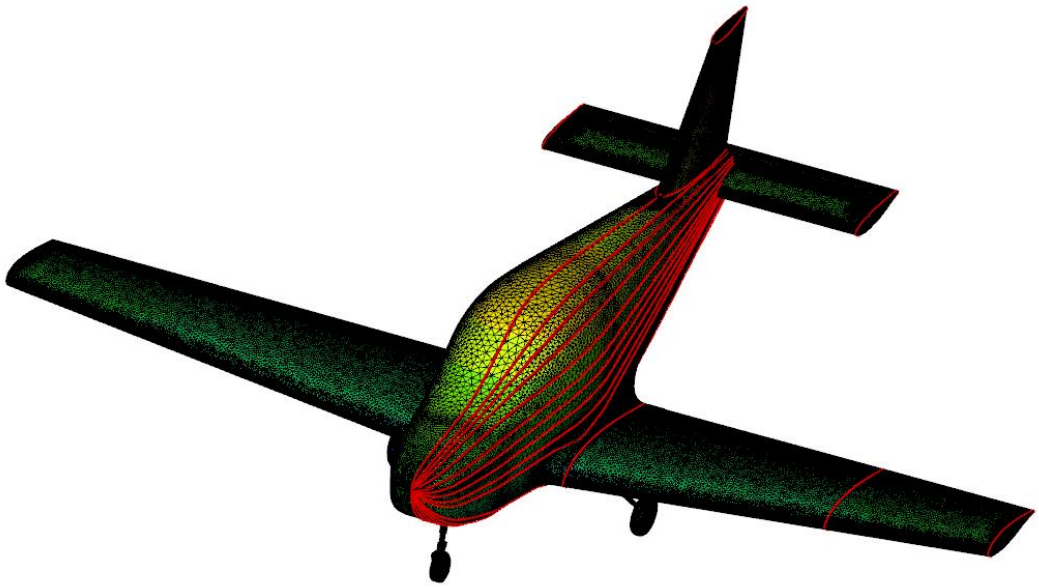

Figure 4.2 Taken Slices from the CFD Model

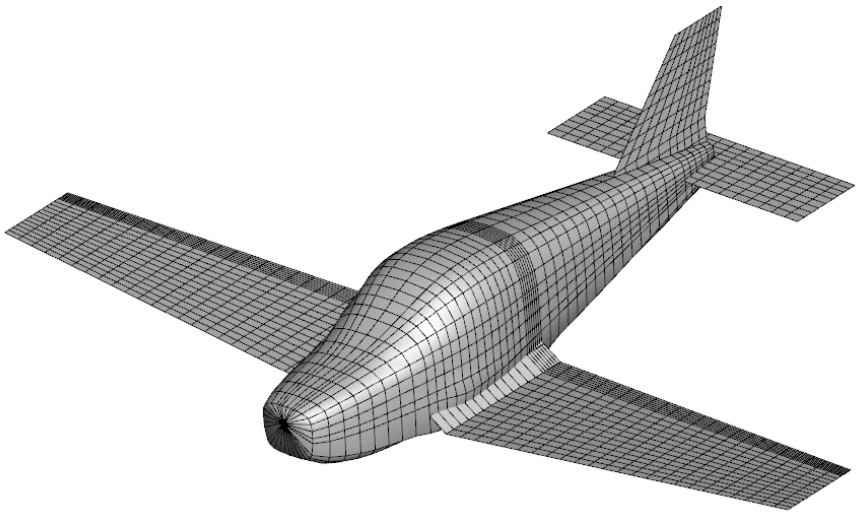

Figure 4.3 Aerodynamic Mesh to be used in Aeroelastic Analysis

In this model, wings and tails are modelled as wing-like elements and fuselage is modelled as a body-like element. In conventional aeroelastic analysis, generally fuselage is not modelled, and this leads to miscalculation of wake vortices in the root of the wing. On the other hand, since wing-like elements are modelled as 2-D panels, the thickness effect is not considered and its effect on the pressure distribution is disregarded; however, since the slices, which are captured from the CFD model, include thickness, and ZAERO has a capability to model the thickness, thickness effect is included in the aeroelastic model. Figure 4.4 shows the 3-D aeroelastic model which also has the thickness effect included in wing-like elements. However, the thickness effect cannot be represented in the spline verification and flutter mode shape representation which is discussed in Section 5.3 and 5.5.

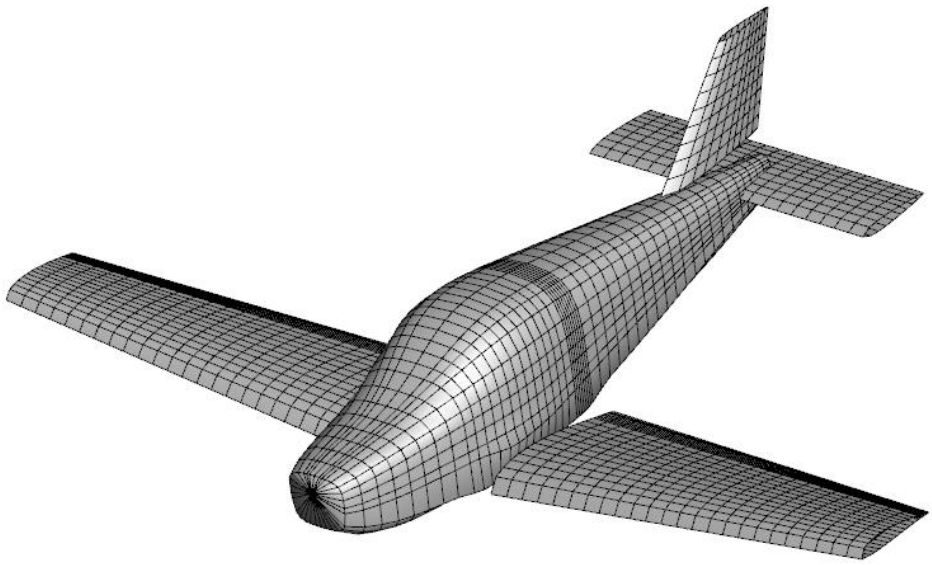

Figure 4.4 Aerodynamic Model in Aeroelastic Analysis with Thickness Effect

Based on the aerodynamic mesh given in Figure 4.4, three-dimensional unsteady linearized small disturbance potential equation [39] is used in the ZONA6 submodule of ZAERO for aerodynamic analysis. It should be noted that the unsteady linearized small disturbance potential equation which is derived from velocity potential equation is widely used and accepted in aeroelasticity field [1] and there are several studies which the fuselage modelled as a body and aeroelastic analysis conducted by utilizing ZAERO in the literature [40],[41],[42].

There are further studies in order to improve the aerodynamic model in aeroelastic analysis such as advanced small perturbation potential flow theory [43] and small disturbance CFD [44]. Therefore, small perturbation assumption is sufficient to represent the aerodynamic behaviour in aeroelastic analysis since the unsteadiness of aerodynamics is based on the small aircraft structure deformations; hence unsteady aerodynamics can easily be assumed linear. The governing three-dimensional unsteady linearized small disturbance potential equation is given by

Equation (4.1) and the derivation of this equation according to usage in aeroelastic analysis and necessary explanations can be found in Appendix C.

$$(1 - M^2{}_\infty)\Phi_{xx} + \Phi_{yy} + \Phi_{zz} - 2\frac{M_\infty}{a_\infty}\Phi_{xt} - \frac{1}{a_\infty^2}\Phi_{tt} = 0 \qquad (4.1)$$

where, M_∞ and a_∞ is the freestream Mach number and speed of sound respectively and Φ denotes the total velocity potential.

The fuselage of the aircraft studied in this thesis is modelled with body-like elements whereas, wings, horizontal and vertical tails of the aircraft are modelled with wing-like elements. ZAERO computes the steady and unsteady pressure on wing-like and body-like components at discrete Mach numbers and reduced frequencies with appropriate integral equations and boundary conditions according to element type and steady/unsteady conditions, then stores AIC matrices. The flow chart of computation procedure for steady and unsteady coefficient of pressures is given in Figure 4.5.

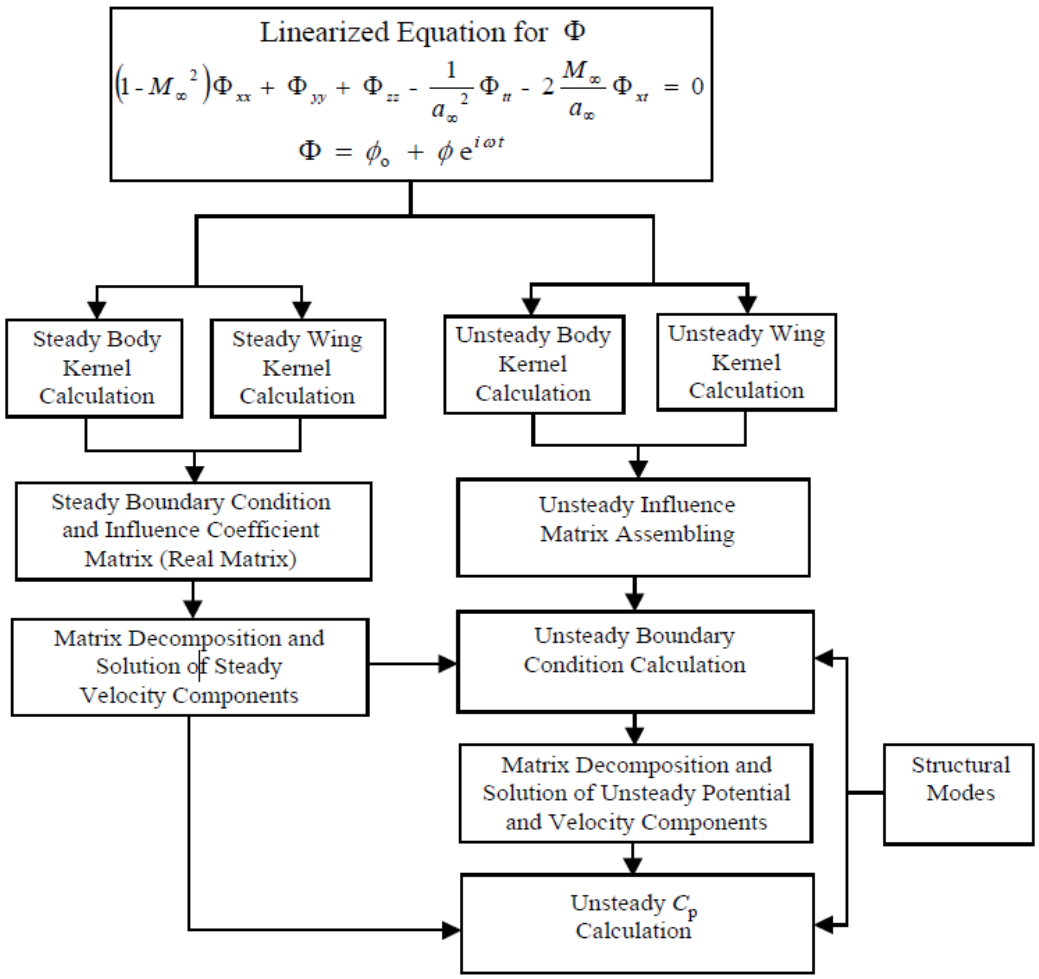

Figure 4.5 Flow Chart of the Computational Procedure for Unsteady Pressures [45]

Following the computational process presented in Figure 4.5, ZAERO makes necessary arrangements by using the pressure coefficient (C_p) and constructs AIC matrices in order to relate the structural mode shapes and the aerodynamic model, as shown in Equation (4.2),

$$\{F_a\} = q_\infty [AIC]\{a\} \tag{4.2}$$

where a, q_∞ F_a denote the aerodynamic displacement vector, dynamic pressure and force and moment vector respectively.

4.3 Rational Function Approximation of Unsteady Aerodynamics

The AIC matrices mentioned in the Section 4.2 are calculated and stored at discrete Mach numbers and reduced frequencies (k). The reduced frequency (k), which is an indication of the unsteadiness of the flow, shows up as the argument in the AIC matrices for the simple harmonic motion assumption. The reduced frequency is defined as,

$$k = \frac{\omega L}{V} \tag{4.3}$$

where ω, L and V are the harmonic oscillatory frequency, reference chord length and velocity of the undisturbed flow. Equation (4.2) can then be re-expressed by Equation (4.4).

$$\{F_a\} = q_\infty [AIC(ik)]\{a\} \tag{4.4}$$

It should be noted that AIC matrices are calculated utilizing simple harmonic motion assumption and stored for each reduced frequency; AIC matrices are defined in the frequency domain. This approach is a very convenient way to study the aeroelastic behavior in terms of calculation time and accuracy. However, time marching solution of nonlinear aeroelastic equations requires time domain aerodynamic force and moment information; therefore, AIC matrices should be transformed into time domain, in other words state space form.

Before this transformation, stored AIC matrices should be in a form of generalized with respect to spline and structural mode shape vector. Spline matrix can be defined such as:

$$\{a\} = [G]\{h\} \tag{4.5}$$

where, a, h and G are aerodynamic displacement vector, structural deformation vector and the spline matrix, respectively. It is worth to mention that size of the h vector is equal to the total structural degree of freedom n_{total}, length of the a vector

is equal to the total number of aerodynamic boxes, n_{aero}, multiplied with 6 since interpolated aerodynamic displacement is expressed in terms of 3 translational (x, y and z axis) displacements, and also their derivatives with respect to the wind axis to cover the slopes of the displacements. Therefore, size of the *G* matrix is (6 x n_{aero}) by (n_{total}). The aerodynamic panels in aeroelastic analysis, wing-like or body-like, have control points which are shown in Figure 4.6. For body-like elements, the control points correspond to the center of the panels, whereas for the wing-like elements, control points correspond to 85% of the chord for subsonic flight regime. The problem of data transversal between the panel model and the structural finite element model usually amounts to the displacement transferal from the structural grid points to the aerodynamic control points of the panel model and that of the forces from the aerodynamic control points to the structural grid points.

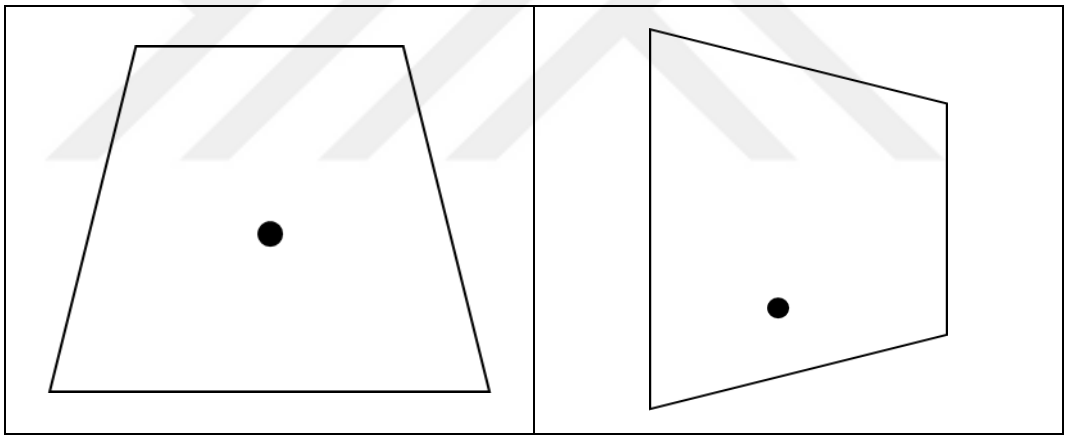

Figure 4.6 Aerodynamic Panel Discretization for Body-like (left) and Wing-like (right) Elements

The aerodynamic force vector (F_a) can be transformed to structural force vector (F_h) by using spline matrix given in Equation (4.5):

$$\{F_h\} = [G]^T\{F_a\} \tag{4.6}$$

The aerodynamic force vector can be re-defined by substituting Equation (4.5) into Equation (4.4):

$$\{F_a\} = q_\infty [AIC(ik)][G]\{h\} \tag{4.7}$$

Then, structural force vector can be expressed by substituting Equation (4.7) into Equation (4.6):

$$\{F_h\} = q_\infty [G]^T [AIC(ik)][G]\{h\} \tag{4.8}$$

It should be noted that the order of the force vector (F_h) given in Equation (4.8) corresponds to the degree of freedom in modal analysis; however, they need to be transformed into the modal domain in order to use in aeroelastic analysis. Once the modal matrix ($[\phi]$) is obtained the via modal analysis solution described in Section 3, the global structural degree of freedom vector (h) can be transformed into generalized coordinates (ξ) as given by Equation (4.9).

$$\{h\} = [\phi]\{\xi\} \tag{4.9}$$

Here, the order of the modal matrix equal to 344214 dof by 19 modes. It should also be noted that 19 modes contain 6 rigid-body modes and 13 elastic modes. Using the governing equation of the structural dynamic system given in Equation (3.2), aeroelastic equation of motion without damping can be defined as:

$$[M]\{\ddot{h}(t)\} + [K]\{h(t)\} = \{F_h\} \tag{4.10}$$

Following the substitution of Equation (4.9) into Equation (4.10) and each term is multiplied by $[\phi]^T$ from left side resulting in,

$$[\bar{M}]\{\ddot{\xi}\} + [\bar{K}]\{\xi\} = [\phi]^T\{F_h\} \tag{4.11}$$

where generalized mass ($[\bar{M}]$) and stiffness ($[\bar{K}]$) matrices are defined as:

$$[\bar{M}] = [\phi]^T[M][\phi] \tag{4.12}$$

$$[\bar{K}] = [\phi]^T[K][\phi] \tag{4.13}$$

Substituting Equation (4.8) into Equation (4.11) using Equation (4.9) gives Equation (14).

$$[\bar{M}]\{\ddot{\xi}\} + [\bar{K}]\{\xi\} = q_\infty [\phi]^T [G]^T [AIC(ik)][G][\phi]\{\xi\} \tag{4.14}$$

To be able to model the kinematic motion of control surfaces and aerodynamic force and moments due to control surfaces in aeroservoelastic analysis, the modal matrix of the system includes control surface modes that are computed internally by ZAERO. Therefore, modal matrix of the system can be represented as a combination of structural mode shapes or modal matrix ($[\phi_h]$) and control surface kinematic mode ($[\phi_c]$). The right side of the Equation (4.14) can be divided into two parts as,

$$[\bar{M}]\{\ddot{\xi}\} + [\bar{K}]\{\xi\} = q_\infty [Q_{hh}(ik)]\{\xi\} + q_\infty [Q_{hc}(ik)]\{\delta\} \tag{4.15}$$

where,

$$[Q_{hh}(ik)] = [\phi_h]^T [G]^T [AIC(ik)][G][\phi_h] \tag{4.16}$$

$$[Q_{hc}(ik)] = [\phi_h]^T [G]^T [AIC(ik)][G][\phi_c] \tag{4.17}$$

and GAF matrix can also be represented as,

$$[Q] = [Q(ik)] = [Q_{hh}(ik)] + [Q_{hc}(ik)] \tag{4.18}$$

Here, $[Q_{hh}]$ and $[Q_{hc}]$ are generalized aerodynamic force (GAF) matrices due to structural modes and control surface modes, respectively.

The conversion of GAF matrices into state-space equations is done using the rational function approximation (RFA). This process has an intermediate step which is the transformation of GAF matrices that are defined in frequency domain into Laplace (s) domain. Although the calculated GAF matrices are defined at specific Mach numbers or velocities and reduced frequencies, Laplace domain is continuous. Therefore, following expression is assumed,

$$g + ik = \frac{sL}{V} \tag{4.19}$$

where g is the non-dimensional damping which expands the unsteady aerodynamics from the imaginary axis (g=0) to the entire Laplace domain [46], and it is not described during the calculation of GAF matrices, and it was taken as zero. However, transformation from frequency domain into time domain requires this damping parameter. At this point, the new challenge is to expand unsteady aerodynamic matrices, which are defined on the red line in Figure 4.7, to the entire Laplace domain.

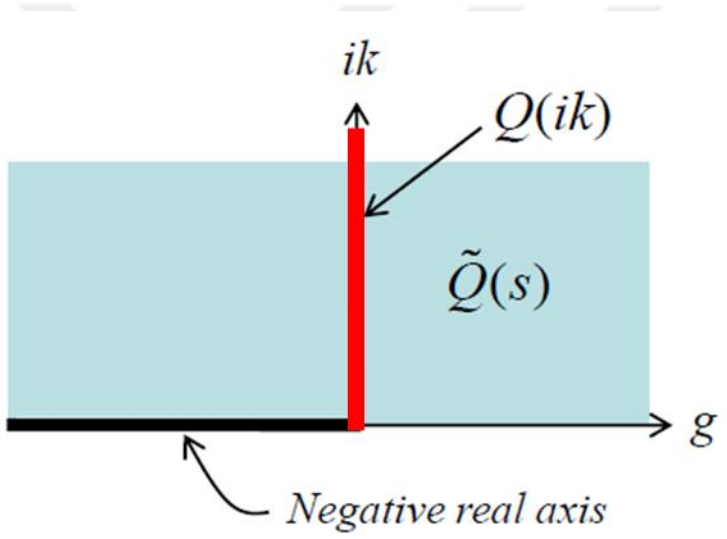

Figure 4.7 Representation of Transformation of GAF from Frequency Domain to Laplace Domain [46]

The calculated GAF matrices are defined at discrete complex reduced frequency numbers. On the other hand, in order to perform nonlinear aeroservoelastic analysis, elements of GAF matrices should be defined in a continuous Laplace domain which includes damping that corresponds to the negative real axis in Figure 4.7. However, the classic GAF matrices are defined only for different reduced frequencies which correspond to positive imaginary axis in the same figure. According to given non-dimensional damping formula in Equation (4.19), for the transformation from

discrete frequency domain to continuous Laplace domain, a set of roots on negative axis which are named as aerodynamic lag roots are required and they are the corresponding damping terms. Then, calculated GAF matrices will be continuous in Laplace domain, and they can easily be transformed to time domain by Inverse Fourier Transform methods. To remove the discontinuity on the negative axis, a set of lag roots are located, as shown in Figure 4.8 [46].

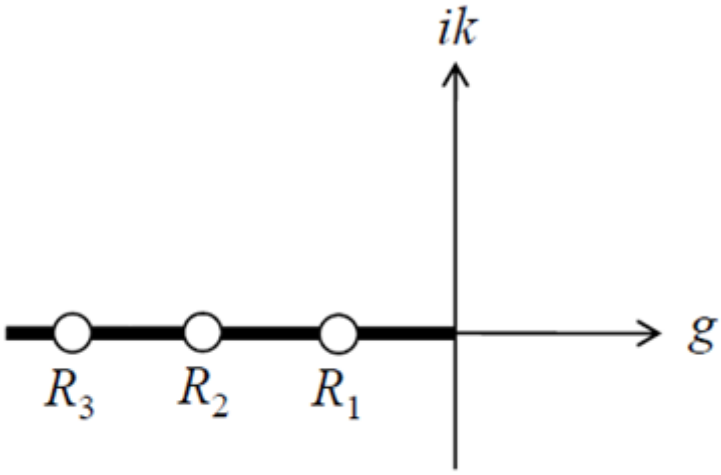

Figure 4.8 Aerodynamic Lag Roots [45]

On negative real axis, the non-dimensional damping is negative which is related to aerodynamic lag. Aerodynamic lag roots represent the delay of the flow since their reduced frequency is zero and they have only non-dimensional damping term.

On the other hand, there is no method or rule of thumb for the selection of the number of aerodynamic lag roots and their location. Hereby, this decision depends on the trial-error procedure. The numbers of aerodynamic lag roots and locations can be determined by comparing the frequency and time-domain GAF matrices. In this comparison, since the conversion is an approximation, calculated aerodynamic matrices in frequency domain can be assumed exact.

Generalized aerodynamic force and moments due to structural mode shapes and kinematic control surface modes can be expressed [45] as:

$$\left[\tilde{Q}(s)\right] = [A_0] + \frac{L}{V}[A_1]s + \frac{L^2}{V^2}[A_2]s^2 + [D]\left[s[I] - \frac{V}{L}[R]\right]^{-1}[E]s \qquad (4.20)$$

here, [A_0], [A_1], and [A_2] represent aerodynamic stiffness, damping and apparent mass matrices of the unsteady aerodynamics respectively. [D] matrix is either identity matrix or treated as a free variable according to least square fit method which is mentioned in the following, [E] matrix is a free variable and [R] stands for aerodynamic lag root matrix where the lag roots are positioned diagonally. In this equation, only known matrix is R and other matrices are found by least square fit procedure utilizing Equations (4.21) and (4.22). This method is based on minimizing the difference between the frequency domain GAF matrices [Q] and approximated GAF matrices [$\tilde{Q}$] in the state-space domain.

$$\varepsilon = \sqrt{\sum_{p,q,r}^{p_{max},q_{max},r_{max}} \varepsilon_{p,q,r}^2} \qquad (4.21)$$

$$\varepsilon_{p,q,r} = \left|\tilde{Q}(ik_r) - Q(ik_r)\right| W_{p,q,r} \qquad (4.22)$$

here, p and q correspond to mode shapes of the structure and r is the reduced frequency index of the GAF matrix respectively. p_{max} and q_{max} denote the total number of mode shapes and r_{max} is the total number of reduced frequencies. W is the weight factor which is used to increase or decrease weight of the mode shapes and reduced frequencies. In this study, weighting factor for all mode shapes and reduced frequencies are taken as equal.

In Equation (4.20) unknown matrices, [A_0], [A_1], and [A_2] for both solution methods and [E] matrix in Roger's Method and [D] and [E] matrices in Minimum State Method are solved using the least square fit procedure.

4.3.1 Roger's Method

Roger's method [46] assumes [*E*] as a free variable and [*D*] and [*R*] are fixed. In this method, [*D*] and [*R*] have the following form,

$$[D] = [[I]_{hh}, [I]_{hh} .. [I]_{hh}]_{N_h x\, N_{lag}} \tag{4.23}$$

$$[R] = -\begin{bmatrix} \begin{bmatrix} \mathrm{R}_1 & & \\ & . & \\ & & \mathrm{R}_{\mathrm{N_{lag}}} \end{bmatrix}_1 & & & \\ & \begin{bmatrix} \mathrm{R}_1 & & \\ & . & \\ & & \mathrm{R}_{\mathrm{N_{lag}}} \end{bmatrix}_2 & & \\ & & . & \\ & & & \begin{bmatrix} \mathrm{R}_1 & & \\ & . & \\ & & \mathrm{R}_{\mathrm{N_{lag}}} \end{bmatrix}_{N_h} \end{bmatrix} \tag{4.24}$$

here *h* denotes the h^{th} mode shape, N_h and N_{lag} are the number of mode shapes and aerodynamic lag terms. Therefore, the size of the [*R*] matrix is N_hxN_{lag} by N_hxN_{lag}.

4.3.2 Minimum State Method

Karpel's minimum state method [8] takes the [*D*] and [*E*] matrices as free variables and [*R*] matrix is assumed as:

$$[R] = -\begin{bmatrix} R_1 & & & \\ & R_2 & & \\ & & . & \\ & & & R_{N_{lag}} \end{bmatrix}_{N_{lag} x N_{lag}} \tag{4.25}$$

4.3.3 Comparison of Roger's and Minimum State Methods

When Equations (4.24) and (4.25) are compared, although number of aerodynamic lag terms in Karpel's minimum state method is only N_{lag}, in Roger's method this number is multiplied with the number of structural modes (N_h x N_{lag}). Since [*D*] and [*E*] matrices are unknowns or free variables in the least square procedure in Karpel's method and it has an iterative solution for these matrices, this method is a nonlinear least square procedure in order to achieve more accurate approximation.

The comparison of the Roger's and Karpel's methods can be conducted on the generalized aerodynamic force matrix of the very light aircraft. It should be noted that generalized aerodynamic force matrices (GAF) are non-dimensionalized with respect the mode shapes and they are calculated at specific Mach number and reduced frequency. This comparison is conducted for all Mach numbers, reduced frequencies and mode shapes by visual inspection. For the calculated AIC matrix at 0.2 Mach which is generalized with the 1st symmetric wing bending mode shape, the comparison of real and imaginary parts of GAF matrices is given in Figure 4.9 for all reduced frequencies. This comparison is made for the Q_{77} element of the GAF matrix. From the visual inspection of this figure, it can be concluded that Roger's method has a better fit to the frequency domain approach than the minimum state method. Therefore, in this study Roger's method is used to transform GAF matrices into state-space format.

In Figure 4.9, the data points on the lines correspond to the reduced frequencies of aerodynamic model since generalized aerodynamic force (GAF) matrices are calculated at discrete Mach numbers and reduced frequencies.

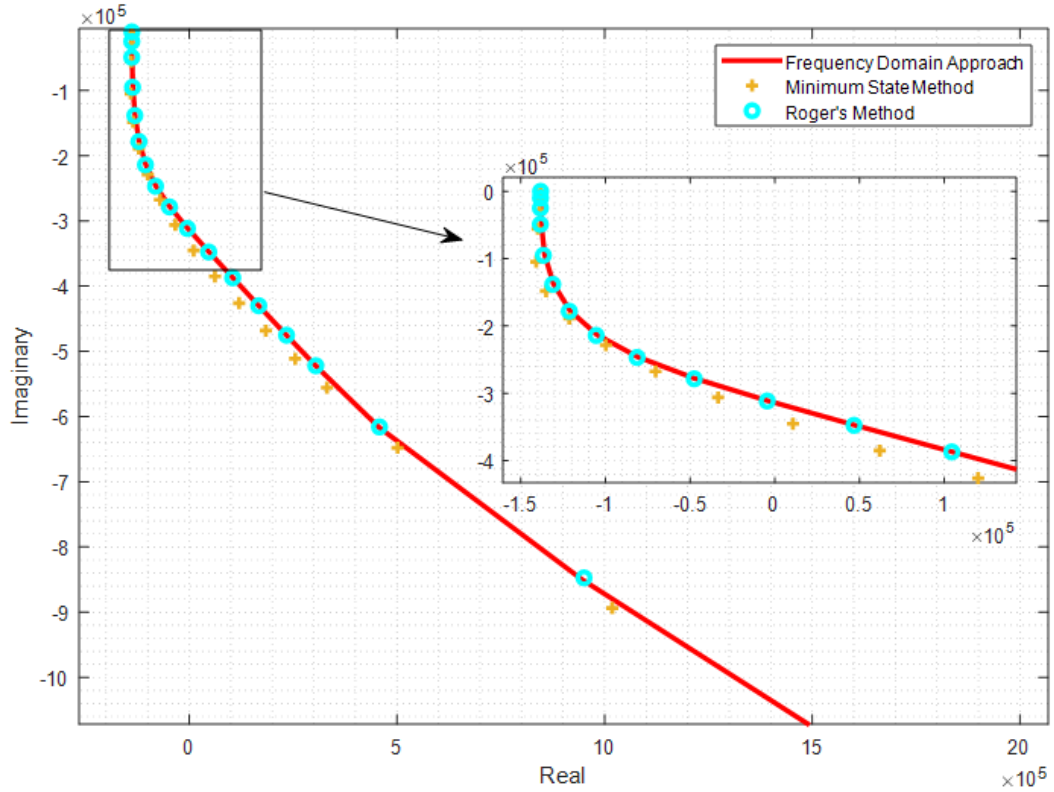

Figure 4.9 Comparison of Roger's and Karpel's Method of GAF (Q_{77}) at 0.2 Mach for Several k

4.4 Conclusion

In this chapter, unsteady aerodynamic model of the aircraft is introduced firstly. In order to conduct aeroservoelastic analysis in time domain and time marching nonlinear aeroelastic analysis, aerodynamic force and moments calculated in frequency domain are transformed into state space via RFA. In this approximation, different methods are compared, and Roger's method approximation is seen fit better to the frequency domain results which can be assumed exact solution. Comparison of Roger's and Karpel's methods is performed for a specific element of the GAF matrix in Figure 4.9, but in general comparison shows that for all elements of the GAF matrix, Mach numbers and reduced frequencies Roger's method gives a better for the frequency domain approach.

CHAPTER 5

AEROELASTIC MODELLING AND ANALYSIS

5.1 Introduction

In this chapter, using the structural dynamic model in modal domain introduced in CHAPTER 3 and aerodynamic model in frequency domain referred in CHAPTER 4, aeroelastic modelling is introduced. In order to couple the structural and the aerodynamic model, spline methodology is presented and then governing equations are introduced. Finally, open-loop flutter analysis is conducted in ZAERO environment and flutter analysis results are presented.

5.2 Spline Methodology

Aeroelasticity phenomenon is a multi-disciplinary phenomenon, and it requires to define the interaction between the structural and aerodynamic models. In other words, the change in aerodynamic force and moments acting on the aircraft due to structural displacements should be calculated. Therefore, in order to transform the modal displacement into the aerodynamic model, spline matrix generation is essential. Constructing spline matrix with ZAERO is nothing but selection of certain structural grids and matching with them with corresponding aerodynamic panels or bodies. It should be noted that the selected structural grids, whose displacements are transformed to aerodynamic model, must belong to hard points of the aircraft in order to prevent the interaction of local mode shapes and the aerodynamic model. Therefore, the structural grids used in spline matrix generation are chosen from grids on frames, ribs and spars of the aircraft, as shown in Figure 5.1 and their positions on the aerodynamic model are shown in Figure 5.2.

Figure 5.1 Spline Grids Selected from the Structural Model

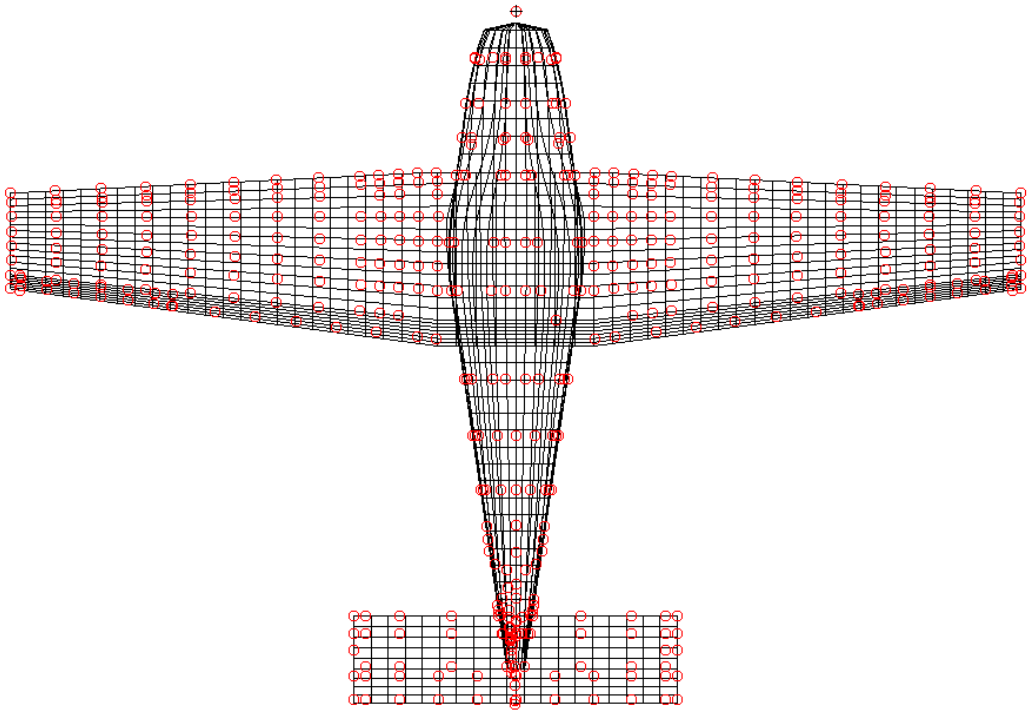

Figure 5.2 Spline Grids Presentation on the Aerodynamic Model

The equation of interaction between the structural deformation and aerodynamic displacement can be expressed in Section 4.3.

5.3 Spline Verification

In order to confirm that selected structural grids used in the spline are adequate, spline verification is necessary for all type of aeroelastic analysis. To do a spline verification, aerodynamic model is checked if the deformation of the aerodynamic model follows the primary structural mode shapes. In Figure 5.3, comparisons are given for some structural modes. For all mode shapes, comparisons are given in Appendix B. Based on the spline verification study, it is concluded that for all structural mode shapes, the deformation of the aerodynamic model followed the structural modes in conformance; therefore, selected structural spline grids are sufficient to build an interaction between the structural and the aerodynamic model.

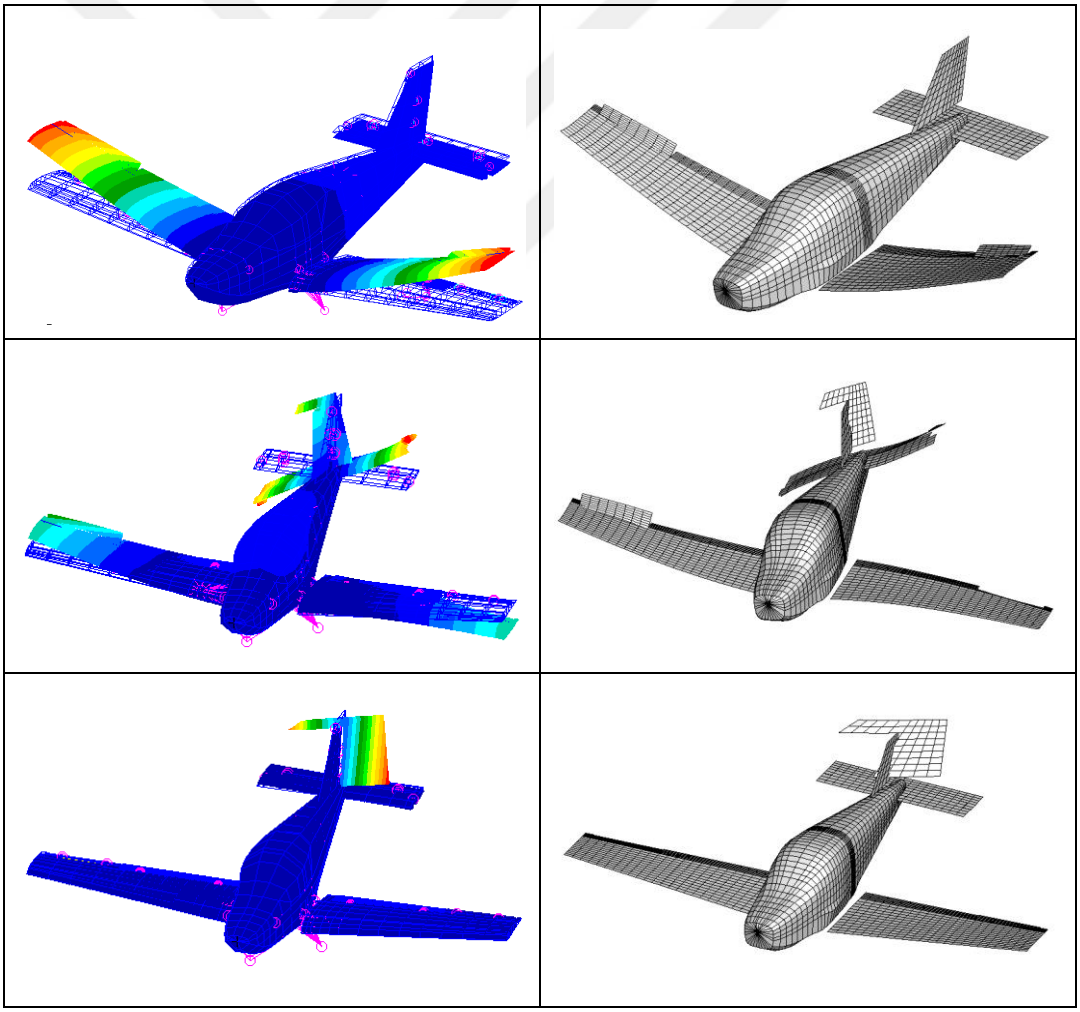

Figure 5.3 Spline Verification for the First Three Elastic Modes

5.4 Governing Equations of Aeroelastic Analysis

Using equations of motions aeroelastic system given in Equation (4.15) and removing one part of the GAF contribution due to control surface modes since this chapter is related with open-loop aeroelastic analysis, governing equation of motion for open-loop aeroelastic system reads:

$$[\bar{M}]\{\ddot{\xi}\} + [\bar{K}]\{\xi\} = q_\infty[Q_{hh}(ik)]\{\xi\} \tag{5.1}$$

where, modal generalized coordinates (ξ) can be re-written by assuming harmonic motion.

$$\{\xi\} = \{\bar{\xi}\}e^{i\omega t} \tag{5.2}$$

Substituting Equation (5.2) into Equation (5.1) yields.

$$-\omega^2[\bar{M}]\{\bar{\xi}\}e^{i\omega t} + [\bar{K}]\{\bar{\xi}\}e^{i\omega t} = q_\infty[Q_{hh}(ik)]\{\bar{\xi}\}e^{i\omega t} \tag{5.3}$$

Simplifying Equation (5.3) reads,

$$\left[-\omega^2[\bar{M}] + [\bar{K}] - q_\infty[Q_{hh}(ik)]\right]\{\bar{\xi}\} = \{0\} \tag{5.4}$$

where $[\bar{M}]$ are $[\bar{M}]$ are the generalized structural mass and stiffness matrices according to Equation (4.12) and (4.13) respectively, $[Q_{hh}(ik)]$ is generalized aerodynamic force (GAF) matrix with respect to structural mode shapes ($[\phi_h]$) only, and ω and q_∞ are the natural frequency and free stream dynamic pressure. In order to measure damping of the aeroelastic system, artificial structural damping, g, is added to the equation which is proposed by Theodorsen [9] and it is widely accepted in the aeroelasticity field, and it is called as K-method flutter equation. It is consistent mathematically with the simple harmonic motion assumption. In the K-method solution, damping is artificial, and it does not have any physical meaning; therefore flutter speed is exact only at the zero damping. Using the K-method flutter solution

method, Equation (5.4) can be rewritten including non-dimensional damping term (g):

$$\left[-\omega^2[\bar{M}] + (1+ig)[\bar{K}] - q_\infty[Q_{hh}(ik)]\right]\{\bar{\xi}\} = 0 \tag{5.5}$$

Dynamic pressure can be written in terms of reduced frequency, *k*, as shown in Equation (5.6).

$$q_\infty = \frac{1}{2}\rho V^2 = \frac{1}{2}\rho\left(\frac{\omega L}{k}\right)^2 \tag{5.6}$$

Inserting Equation (5.6) into Equation (5.5) and dividing the whole equation with square of natural frequency gives the eigenvalue problem for flutter analysis in the K-method:

$$\left[[\bar{M}] + \frac{\rho}{2}\left(\frac{L}{k}\right)^2 + [Q_{hh}(ik)] - \lambda[\bar{K}]\right]\{\bar{\xi}\} = 0 \tag{5.7}$$

where λ is the complex eigenvalue which is determined by an eigenvalue problem after some iterations. Complex eigenvalue is defined by Equation (5.8).

$$\lambda = \left(\frac{1+ig}{\omega^2}\right) \tag{5.8}$$

The K method in aeroelastic analysis is not a matched solution method, in another saying, resultant flutter velocity does not correspond to the Mach number which is used in calculation of AIC matrices. Therefore, P-K method, which is a matched solution method, is used in this study. This method is proposed by Hassig [47] and it is expressed as,

$$\left[\left(\frac{V}{L}\right)^2[\bar{M}]\tilde{p}^2 + [\bar{K}] - \frac{1}{2}\rho V^2[Q_{hh}(ik)]\right]\{\bar{\xi}\} = 0 \tag{5.9}$$

where, $\tilde{p}$ is the non-dimensional Laplace parameter, and it is expanded as:

$$\tilde{p} = g + ik \tag{5.10}$$

where non-dimensional damping is assumed as a function of transient decay rate coefficient (γ) and reduced frequency (k) shown in Equation (5.11).

$$g = \gamma k \tag{5.11}$$

In the iterative solution algorithm of the P-K method, reduced frequency k and the imaginary part of $\tilde{p}$ is matched; hence the solution is a matched point solution. The imaginary part of the solution gives the resultant frequency of the system, and the real part of the system gives the estimated damping at each velocity. Finally, the eigenvalue problem solution of Equation (5.9) gives velocity versus damping (V-g) and velocity versus frequency (V-f) curves which are the general outputs of flutter analysis.

5.5 Flutter Analysis Results

Based on aerodynamic and structural models which are introduced in Chapter 3 and Chapter 4 respectively, flutter analysis is conducted within ZAERO environment using the P-K method. The list of velocities and the corresponding Mach numbers and the reduced frequencies used to calculate the AIC matrices are listed in Table 5.1. In this table, velocities and Mach numbers correspond to each other since all analyses are conducted at the sea level altitude. It should be noted that for each 22 velocities or corresponding Mach numbers, AIC matrices are calculated and saved for 20 reduced frequencies by using ZAERO. According to ZAERO file management system, each of the saved AIC matrix files contains required reduced frequencies within. Therefore, totally 22 AIC matrix files are saved whereas 440 Mach-k pair AIC matrices are used in this study.

Table 5.1 Parameters of AIC Matrices

#	*Velocities (m/s)*
1	0.000
2	10.000
3	20.000
4	30.000
5	40.000
6	50.000
7	60.000
8	70.000
9	80.000
10	90.000
11	100.000
12	110.000
13	120.000
14	130.000
15	140.000
16	150.000
17	160.000
18	170.000
19	180.000
20	190.000
21	200.000
22	210.000

#	*Mach Numbers (M)*
1	0.000
2	0.030
3	0.060
4	0.090
5	0.120
6	0.150
7	0.170
8	0.200
9	0.230
10	0.260
11	0.290
12	0.320
13	0.350
14	0.380
15	0.410
16	0.440
17	0.470
18	0.500
19	0.520
20	0.550
21	0.580
22	0.610

#	*Reduced Frequencies (k)*
1	0.000
2	0.020
3	0.050
4	0.100
5	0.200
6	0.300
7	0.400
8	0.500
9	0.600
10	0.700
11	0.800
12	0.900
13	1.000
14	1.100
15	1.200
16	1.300
17	1.500
18	2.000
19	2.500
20	3.000

The results of flutter analysis are presented as velocity-damping (V-g) and velocity-frequency (V-f) plots in the velocity range of interest given in Table 5.1 and at the sea level. Velocity-damping and velocity-frequency plots are given in Figure 5.4 and Figure 5.5, respectively.

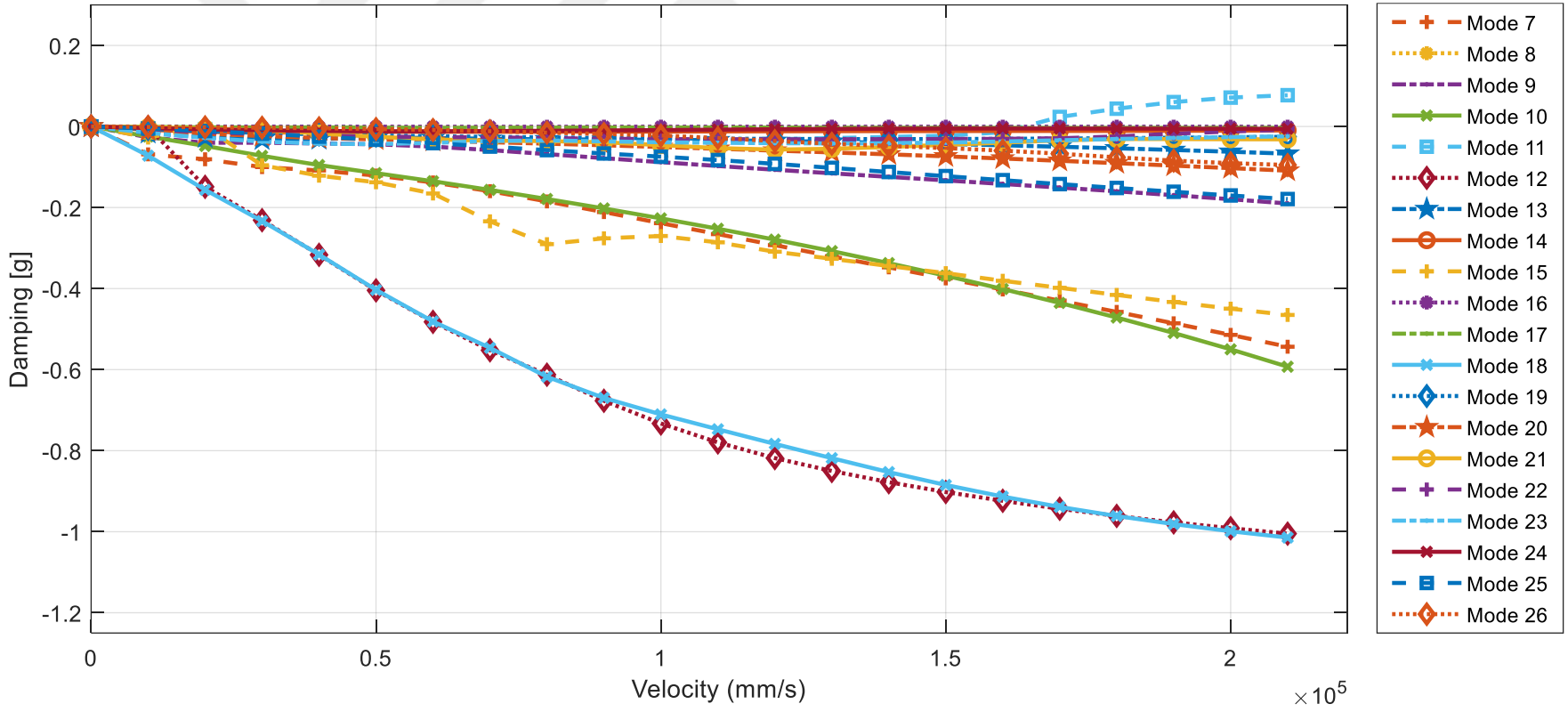

Figure 5.4 Velocity vs Damping Plot

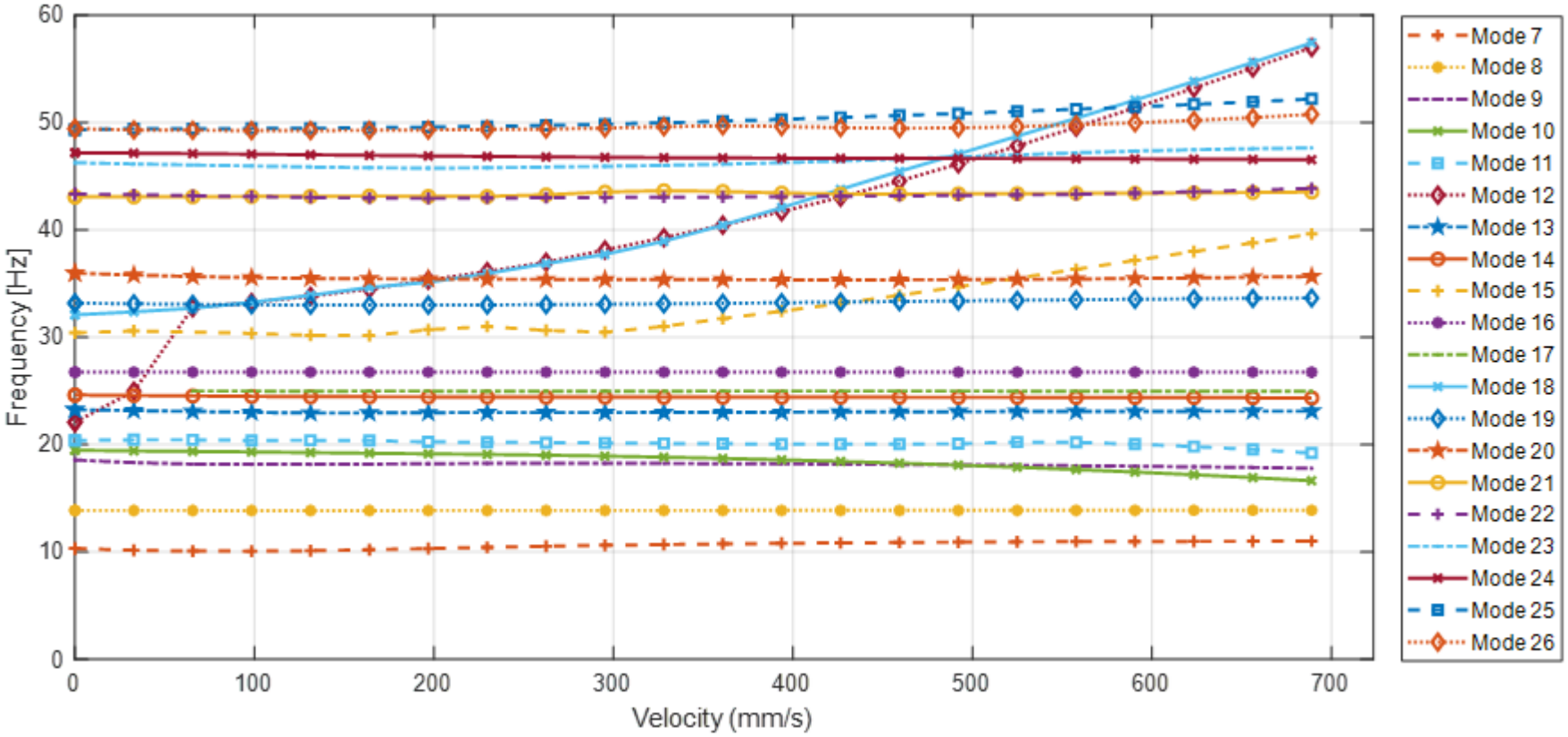

Figure 5.5 Velocity vs Frequency Plot

It should be noted that, matched point flutter solution algorithm is used during the flutter analysis. Moreover, because of the unrestrained aircraft model, aeroelastic behavior of rigid body modes are excluded from results. The starting point for undamped oscillatory solutions of the structure is the flutter speed; thus, this is referred to as the vehicle's flutter speed. It can be concluded from flutter result graphs that the aircraft is free from flutter within its flight regime. Beyond the dive speed of the very light aircraft which is 70.736 m/s, flutter instability is observed at 163 m/s. The flutter mode shape is dominated with mode shape of 1st symmetric elevator bending and mode shapes of aileron antisymmetric bending and wing in-plane bending slightly contribute to this flutter mode shape. It should be also noted that, there is also a slight contribution of the local flap mode. The flutter mode shape is given in Figure 5.6.

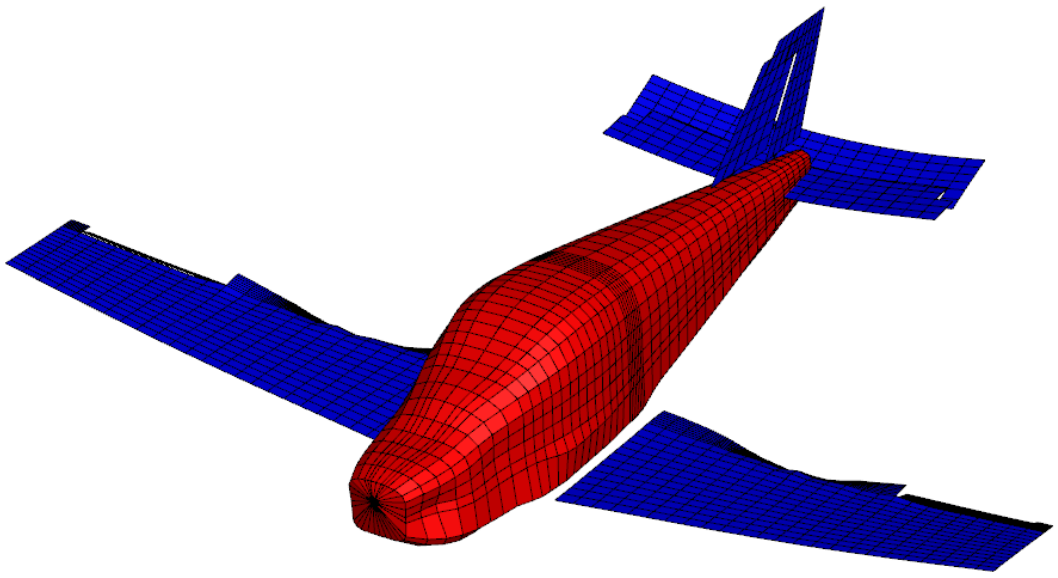

Figure 5.6 Flutter Mode Shape at 163 m/s

5.6 Conclusion

In this chapter, firstly spline methodology and verification study are introduced in order to couple the aerodynamic and the structural models. Then, governing equations belonging to the classic flutter analysis are presented and finally, the results of the analysis are shared.

The results show that aircraft is free from flutter instability within the flight regime. In the structural modal analysis, structural damping of the aircraft is assumed as zero which is unrealistic and conservative approach in aeroelastic analysis; therefore, the instability of the aircraft is determined by the positive damping. Mode 11 which is the mode shape of 1st symmetric elevator bending has a positive damping starting from V_f =163 m/s which indicates the flutter instability. However, flutter speed (V_f) is outside of flight regime and also beyond of the 1.15 times of dive speed (V_D), of the aircraft which is as a required flutter clearance velocity for safety margin in aerospace field [48]. For the very light aircraft, 1.15 times the dive speed is 81.346 m/s.

CHAPTER 6

NONLINEAR AEROSERVOELASTIC MODELLING AND ANALYSIS

6.1 Introduction

In this chapter of the thesis, nonlinear aeroservoelastic modelling analysis procedures are presented. Firstly, actuator model implementation is introduced; because actuator dynamic behavior is necessary for control law implementation in ASE analysis. After the implementation of the actuator model and consequently of its states in the state-space representation of the aeroelastic model, this system became the plant level in the aeroelastic system. Then, including control law modeling to aeroelastic system, aeroservoelastic modelling is obtained and this is called as the vehicle level model.

Then, nonlinearity which originates from the freeplay in the control surfaces is included in ASE analysis and nonlinear system dynamic equations are obtained. In order to implement nonlinearity more accurately, fictitious mass approach is used. Governing equations of motion of nonlinear aeroservoelastic system with fictitious mass approach and freeplay are introduced.

Finally, time marching solutions of presented nonlinear aeroservoelastic system are calculated via ZAERO and they are presented. For each control surface i.e., ailerons, elevator, and rudder, freeplay motion is treated separately and also when freeplay exist in more than one control surface. Time marching solutions are conducted at different flight conditions.

6.2 Actuator Modelling

The aim of the actuation system is to deflect the control surface to the commanded position by the flight control system. Actuation system has its own control system, and it needs electricity or hydraulic pressure for actuation and a phase and lag generally occurs between the command and the control surface motion. The imperfection of this system can be represented by a transfer function and this dynamic behavior can affect the aeroservoelastic system significantly. However, since the purpose of this study is not to investigate the effect of the dynamic behavior of the actuator on the aeroservoelastic analysis, a third-order dummy transfer function is assigned between the control surface deflection and the actuator command. The reason of third order is that ZAERO requires actuator transfer functions to be at least third order. Third order transfer function can be expressed as:

$$\frac{\delta_{cs}(s)}{u_{ac}(s)} = \frac{A_3}{s^3 + A_1 s^2 + A_2 s + A_3} \tag{6.1}$$

where δ_{cs} and u_{ac} are the control surface deflection and the actuator command in Laplace domain, respectively. In order to prevent the effect of the actuator dynamic on the aeroservoelastic model, the parameters of the third-order dummy transfer function, i.e., A_1, A_2, A_3 are taken as listed in Table 6.1. These parameters are chosen by a trial-error procedure so that gain and phase margins are minimized within the frequency range of interest.

Table 6.1 Actuator Transfer Function Parameters

Parameter	*Value*
A_1	1409.690
A_2	132.4820 E+4
A_3	830.036 E+5

As it can be seen in Figure 6.1, the magnitude and phase of the transfer function are very close to 0 dB and 0 degree implying that the dummy actuator transfer function does not influence the dynamic behavior of the aircraft in the frequency range of interest between the 0 and 50 Hz.

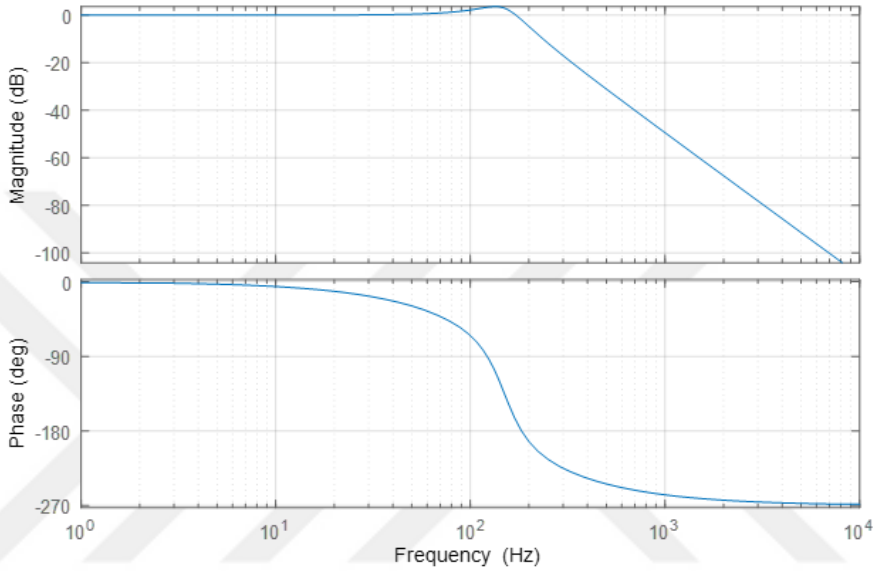

Figure 6.1 Bode Diagram of the Actuator Transfer Function

The actuator transfer function given in Equation (6.1) can be defined in state-space representation in the following forms:

$$\{\dot{x_{act}}\} = \begin{bmatrix} 0 & 1 & 0 \\ 0 & 0 & 1 \\ -A_3 & -A_2 & -A_1 \end{bmatrix} \{x_{act}\} + \begin{Bmatrix} 0 \\ 0 \\ A_3 \end{Bmatrix} u_{act} \tag{6.2}$$

$$\{\dot{x_{act}}\} = [A]\{x_{act}\} + [B]u_{act} \tag{6.3}$$

where x_{act} is the actuator transfer function states and it can be expressed as:

$$\{x_{act}\} = \begin{Bmatrix} \delta \\ \dot{\delta} \\ \ddot{\delta} \end{Bmatrix} \tag{6.4}$$

6.3 Aeroservoelastic Modelling

Before constructing the aeroservoelastic model, aeroelastic Equation (5.1) should be expressed in state space form by utilizing the RFA and transforming the frequency domain solution into time domain. Firstly, rational function approximation of the GAF matrices is expressed as contribution of both structural mode shapes {ξ} and control surface deflections {δ},

$$\left[\tilde{Q}\right] = \left[\tilde{Q}_{hh}(\xi)\right] + \left[\tilde{Q}_{hc}(\delta)\right] \tag{6.5}$$

$$\left[\tilde{Q}_{hh}(\xi)\right] = q_\infty \left[\left[A_{hh_0}\right]\{\xi\} + \frac{L}{V}\left[A_{hh_1}\right]\{\dot{\xi}\} + \frac{L^2}{V^2}\left[A_{hh_2}\right]\{\ddot{\xi}\}\right] \tag{6.6}$$

$$\left[\tilde{Q}_{hc}(\delta)\right] = q_\infty \left[\left[A_{hc_0}\right]\{\delta\} + \frac{L}{V}\left[A_{hc_1}\right]\{\dot{\delta}\} + \frac{L^2}{V^2}\left[A_{hc_2}\right]\{\ddot{\delta}\} + [D]x_a\right] \tag{6.7}$$

where, A matrices in Equation (6.6-6.7) are the submatrices of A matrices given Equation (4.20) and x_a is the aerodynamic state vector due to the rational function approximation which can be expressed as:

$$x_a = \left[s[I] - \frac{V}{L}[R]\right]^{-1} \left[[E_h]\{\xi\} + [E_c]\{\delta\}\right] \tag{6.8}$$

Then, re-expressing Equation (4.15) by using Equation (6.6-6.7), one gets,

$$[\bar{M}]\{\ddot{\xi}\} + [\bar{K}]\{\xi\} + [M_{hc}]\{\ddot{\delta}\} = q_\infty\left[\tilde{Q}_{hh}(\xi) + \tilde{Q}_{hc}(\delta)\right] \tag{6.9}$$

where, $[\bar{M}]$ and $[\bar{K}]$ are the generalized mass and stiffness with respect to modal matrix ($[\phi_h]$) respectively. These matrices are also given in Equation (4.12-4.13). It should be noted that, approximated GAF matrix with RFA ($\left[\tilde{Q}\right]$) is denoted as $[Q]$ to simplify the editing of equations through the rest of the study. $[M_{hc}]$ is the generalized mass matrix with respect to modal matrix ($[\phi_h]$) and control surface mode shapes ($[\phi_c]$), which is expressed as in Equation (6.10).

$$[M_{hc}] = [\phi_h][M][\phi_c] \tag{6.10}$$

Then assuming aeroelastic state as combination of structural mode shape vector, the first derivative of it with respect to time and aerodynamic state respectively:

$$\{x_{ae}\} = \begin{Bmatrix} \xi \\ \dot{\xi} \\ x_a \end{Bmatrix} \tag{6.11}$$

State space form of the aeroelastic system of equations can be expressed in the following form according to state-space representation of linear time independent (LTI) systems [49]:

$$\{\dot{x_{ae}}\} = [A_{ae}]\{x_{ae}\} + [B_{ae}]\{u_{ae}\} \tag{6.12}$$

$$\{y_{ae}\} = [C_{ae}]\{x_{ae}\} \tag{6.13}$$

where

$$[A_{ae}] = \begin{bmatrix} 0 & I & 0 \\ -\left[\widetilde{M}\right]^{-1}\left[[\bar{K}] - q_\infty\left[A_{hh_0}\right]\right] & \left[\widetilde{M}\right]^{-1}\left[\frac{q_\infty L}{V}\left[A_{hh_1}\right]\right] & q_\infty\left[\widetilde{M}\right]^{-1}[D] \\ 0 & E_h & \frac{V}{L}[R] \end{bmatrix} \tag{6.14}$$

$$[B_{ae}] = \begin{bmatrix} 0 & 0 & 0 \\ q_\infty\left[\widetilde{M}\right]^{-1}\left[A_{hc_0}\right] & \frac{q_\infty L}{V}\left[\widetilde{M}\right]^{-1}\left[A_{hc_1}\right] & -[M_{hc}]^{-1}\left[M_{hc} - \frac{q_\infty L^2}{V^2}\right]\left[A_{hc_2}\right] \\ 0 & E_c & 0 \end{bmatrix} \tag{6.15}$$

$$\left[\widetilde{M}\right] = \left[[\bar{M}] - \frac{q_\infty L^2}{V^2}\left[A_{hh_2}\right]\right] \tag{6.16}$$

In Equations (6.12) and (6.13), x_{ae} is the aeroelastic state vector, ξ and $\dot{\xi}$ are the structural mode shape vector and its first derivative with respect to time, respectively. A_{ae} and B_{ae} include generalized aerodynamic force and moments due to structural

deformation and control surface rotation. u_{ae} is the input vector of the system which defines control surface deflections, i.e., aileron, elevator and rudder deflections. y_{ae} is the output vector of the aeroelastic system which corresponds to sensor states, and they are the rotational rates of the aircraft in 3 axes, and they are denoted as p, q and r. C_{ae} matrix represents the sensor model in the structural dynamics model since it is necessary for the control algorithm. In ZAERO, the location of the sensor on aircraft is provided by a structural node in the FE model. It should be noted that a structural grid point at the center of gravity of the aircraft is created and it is selected as a sensor grid for the aeroservoelastic model. This sensor model measures the necessary inputs of flight control algorithm. The input to the flight control algorithm corresponds to the output of the aeroelastic plant system (y_{ae}). In this study, since the sensors measure the velocity of a structural grid, $[C_{ae}]$ matrix can be defined as:

$$C_{ae} = \begin{bmatrix} [0] \\ [\phi_{h_i}] \\ [0] \end{bmatrix} \tag{6.17}$$

where, $[\phi_{h_i}]$ represents the modal displacement of structural modes at the ith grid in the FE model corresponding to the sensor grid.

Appending the third order actuator dynamic states given in Equations (6.3) into aeroelastic state space equations which is given in Equations (6.12-6.13), state-space plant model is obtained as,

$$\{\dot{x_p}\} = [A_p]\{x_p\} + [B_p]\{u_p\} \tag{6.18}$$

$$\{y_p\} = [C_p]\{x_p\} + [D_p]\{u_p\} \tag{6.19}$$

$$\{x_p\} = \begin{Bmatrix} x_{ae} \\ \delta \\ \dot{\delta} \\ \ddot{\delta} \end{Bmatrix} \tag{6.20}$$

where, δ, $\dot{\delta}$ and $\ddot{\delta}$ are control surface actuator states and their first and second derivative with respect to time respectively. u_p is the input of the plant system and it corresponds to control surface actuator inputs in the plant model and y_p is the output vector and it is identical to y_{ae}. It should be noted that, the plant-level aeroelastic system includes aerodynamic, structure, actuator and sensor models, and the only difference from vehicle-level aeroelastic or aeroservoelastic model is the flight control algorithm.

6.3.1 Trim Analysis and Rigid Body Aircraft Stability Derivatives

In order to obtain the flight control law algorithm, stability derivatives of the rigid aircraft are necessary. Therefore, static aeroelastic or trim analysis is conducted in ZAERO environment. It should be noted that, although static aeroelastic analysis is not within the scope of this thesis, the result of trim analysis yields flexible and rigid stability coefficients and also their derivatives. The governing equations of static aeroelastic analysis is expressed as [45]:

$$[K]\{h\} = \{F_a\} - \{F_I\} \tag{6.21}$$

where, K is global structural stiffness matrix, F_a and F_I are aerodynamic and inertia force and moment vectors respectively. ZAERO solves Equation (6.16) while balancing aerodynamic and inertial forces acting on the flexible aircraft. Moreover, F_a is expressed as the superposition of the rigid body forces, F_R, due to rigid body or control surface motion and flexible forces, F_f, due to the structural deformation, as shown by Equation (6.9).

$$\{F_a\} = \{F_f\} + \{F_R\} \tag{6.22}$$

In order to obtain rigid body stability derivatives, flexible forces on the aircraft assumed as zero and rigid body forces on aircraft are expressed with respect to control law algorithm inputs, p, q and r, and also control surface deflections, i.e., δ_{ail}, δ_{elev} and δ_{rud}.

$$\{F_a\} = \{F_R\} = F_R(p, q, r, \delta_{ail}, \delta_{elev}, \delta_{rud}) \quad (6.23)$$

The inputs and outputs of the trim analysis are listed in Table 6.2. It should be noted that rates are nondimensionalized. In this table, *b*, *S* and *c* correspond to half-span, reference area of the wing and span length respectively. Moreover, *M* denotes the moment, q_∞ is the dynamic pressure.

Table 6.2 Trim Analysis Inputs and Outputs

#	*Trim Inputs*	*Units*	*Trim Outputs*
1	p rate	[pb/2V]	Drag Coefficient ($\mathbf{\Delta}C_x$)
2	q rate	[qc/2V]	Side Force Coefficient ($\mathbf{\Delta}C_y$)
3	r rate	[rb/2V]	Lift Coefficient ($\mathbf{\Delta}C_z$)
4	Aileron Deflection	degree	Roll Moment Coefficient ($\mathbf{\Delta}C_l$)
5	Elevator Deflection	degree	Pitch Moment Coefficient ($\mathbf{\Delta}C_m$)
6	Rudder Deflection	degree	Yaw Moment Coefficient ($\mathbf{\Delta}C_n$)

In Table 6.2, trim inputs are defined in an unconventional way which is required in static aeroelastic analysis in ZAERO. Normally, *p* rate described for the roll acceleration of the aircraft with respect to x axis and its unit is radian per second (radian/second). Since ZAERO requires these parameters in non-dimensionalized form, *p*, *q* and *r* rates are non-dimensionalized with respect to their *p*, *q* and *r* angles, respectively, half-span (b), chord (c) and the velocity (V). On the other hand, the trim outputs which are coefficients of the aircraft are in conventional units. In the following Table 6.3 and Table 6.4, the trim analysis results which are the delta coefficients of the aircraft are given with respect to unit p rate input and unit aileron input, respectively. These analyses are conducted for several Mach numbers, but in Table 6.3 and 6.4, the results are given for only four different Mach numbers.

Table 6.3 Coefficients of Aircraft for a Unit p Rate Input in Static Trim Analysis

Mach #	ΔC_x	ΔC_y	ΔC_z	ΔC_l	ΔC_m	ΔC_n
0.050	0.00100	-0.01537	-0.45415	-0.46016	1.17622	-0.02747
0.111	0.00287	-0.01382	-0.43735	-0.46170	1.14900	-0.02297
0.134	0.00288	-0.01403	-0.43893	-0.46236	1.15341	-0.02306
0.156	0.00289	-0.01427	-0.44072	-0.46312	1.15845	-0.02316

Table 6.4 Coefficients of Aircraft for a Unit Aileron Input in Static Trim Analysis

Mach #	ΔC_x	ΔC_y	ΔC_z	ΔC_l	ΔC_m	ΔC_n
0.050	0.00000	-0.00026	0.00060	0.00267	-0.00150	0.00006
0.111	0.00000	-0.00027	0.00055	0.00267	-0.00145	0.00005
0.134	0.00000	-0.00027	0.00056	0.00268	-0.00146	0.00005
0.156	0.00000	-0.00027	0.00056	0.00268	-0.00147	0.00005

It should be noted that all delta coefficients found in static aeroelastic analysis are calculated with respect to the aerodynamic center of the aircraft. However, the motion of the aircraft is governed according to the force and moments acting about the center of gravity; therefore, calculated forces and moments at the aerodynamic center should be translated to the center of gravity. The positions of the aerodynamic center and the center of gravity as measured from the nose of the aircraft are given in Table 6.5.

Table 6.5 Position of Center of Gravity and Aerodynamic Center

Point	*x (mm)*	*y (mm)*	*z (mm)*
Center of Gravity	1898.000	0.000	-425.700
Aerodynamic Center	2007.000	-0.560	-119.200

Since the delta coefficients of the aircraft are the response to corresponding unit inputs, they are also the derivatives of the aircraft at the same time. For example, for a unit aileron input corresponding to 1 degree in trim analysis, the change in the aerodynamic coefficients is the result of the analysis. Since the inputs of the analysis are unit and the results are the change in coefficients, the delta coefficients determined are the derivatives of the aircraft with respect to input of the analysis. The derivatives of the VLA are compared with the derivatives of a similar aircraft CESSNA 182 [50] and presented in Table 6.6 . It is seen that the derivatives of these two aircraft match well which means that stability derivatives of the VLA are reasonable and they can be directly used to model the rigid body motion of the aircraft.

Table 6.6 Comparison of CESSNA 182 [50] and METU-VLA Stability Derivatives

Stability Derivative	CESSNA 182	METU-VLA
c_{L_α}	4.4100	4.8140
c_{L_q}	3.9000	4.4410
c_{m_α}	-0.6130	-0.9250
c_{m_q}	-12.4000	-12.6040
c_{n_r}	-0.0930	-0.0780
c_{n_p}	-0.0278	-0.0274

Next step is expressing equation of motion of the rigid aircraft in state-space [49] domain as,

$$\{\dot{x_R}\} = [A_R]\{x_R\} + [B_R]\{u_R\} \tag{6.24}$$

$$\{y_R\} = [C_R]\{x_R\} + [D_R]\{u_R\} \tag{6.25}$$

where C_R and D_R are identity and zero matrices and,

$$x_R = \begin{bmatrix} p \\ q \\ r \end{bmatrix} \tag{6.26}$$

$$u_R = \begin{bmatrix} \delta_{ail} \\ \delta_{elev} \\ \delta_{rud} \end{bmatrix} \tag{6.27}$$

$$[A_R] = \begin{bmatrix} \frac{d(c_l)}{dp} & \frac{d(c_l)}{dq} & \frac{d(c_l)}{dr} \\ \frac{d(c_m)}{dp} & \frac{d(c_m)}{dq} & \frac{d(c_m)}{dr} \\ \frac{d(c_n)}{dp} & \frac{d(c_n)}{dq} & \frac{d(c_n)}{dr} \end{bmatrix} \tag{6.28}$$

$$[B_R] = \begin{bmatrix} \frac{d(c_l)}{d\delta_{ail}} & \frac{d(c_l)}{d\delta_{elev}} & \frac{d(c_l)}{d\delta_{rud}} \\ \frac{d(c_m)}{d\delta_{ail}} & \frac{d(c_m)}{d\delta_{elev}} & \frac{d(c_m)}{d\delta_{rud}} \\ \frac{d(c_n)}{d\delta_{ail}} & \frac{d(c_n)}{d\delta_{elev}} & \frac{d(c_n)}{d\delta_{rud}} \end{bmatrix} \tag{6.29}$$

Since the outputs of static aeroelastic analysis yield the rigid body derivatives of aircraft with respect to inputs of the analysis, all derivatives in A_R and B_R matrices are acquired. Once the A_R and B_R matrices are obtained, control algorithm can be included in the equations of motion of rigid body dynamics, and this study is presented in the following section.

6.3.2 Control Law Modelling

Using the A_R and the B_R matrices, given by Equations (6.23) and (6.24), at specific Mach numbers a simple flight control algorithm with feedback gain technique is developed by the pole placement [51] using the "*place"* command in MATLAB®. With this technique, the negative or near zero eigenvalues or poles of the matrix A_R are transformed to negative and away from zero since the stability criteria for

stability of rigid body aircraft system is to have negative eigenvalues for the A_R matrix.

Utilizing a simple flight control algorithm with linear feedback gain matrix *K* which is developed in MATLAB environment, Simulink model of the flight control algorithm is shown in Figure 6.2.

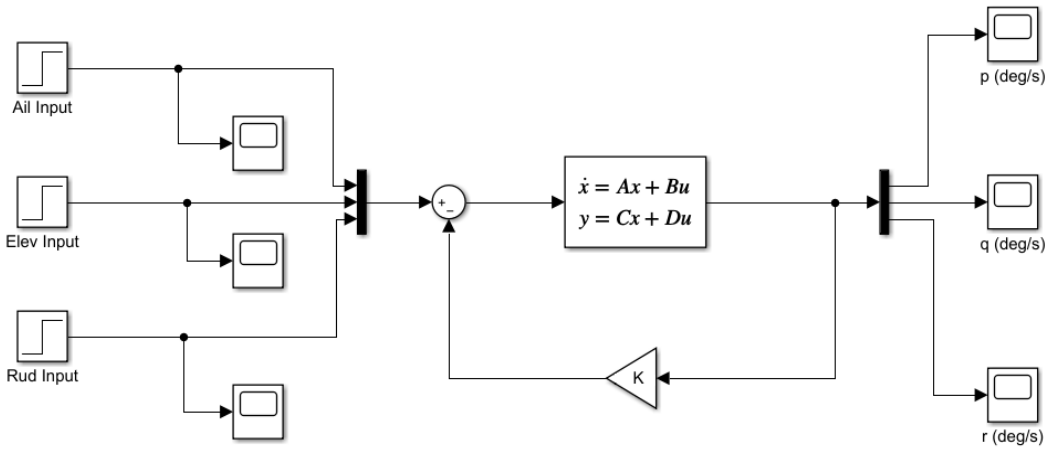

Figure 6.2 Simulation Model of the Flight Control Algorithm

The poles of the system before the control algorithm implementation are determined from Equation (6.25).

$$\det|sI - A_R| = 0 \tag{6.30}$$

The poles of the system after the control algorithm implementation are determined from Equation (6.26). The gain matrix $[K]$ as been selected according to the pole placement process. With the "place" command, desired eigenvalues of the closed-loop system can be easily obtained, and the output of this command is the $[K]$ matrix.

$$\det|sI - (A_R - B_R K)| = 0 \tag{6.31}$$

Open-loop system poles are investigated for several Mach numbers which are given in Table 5.1 at sea level and it is seen that there are no positive poles, which means

that the open-loop model of the aircraft is stable at these flight conditions. During the pole placement method, the poles of the closed-loop system are taken as twice the poles of the open-loop system of the corresponding each flight condition. In other words, the open-loop poles are doubled just to increase stability of the aircraft and obtain a simple flight control algorithm and used in the analysis.

In order to check feedback control algorithm, the aeroelastic plant model which is computed at 0.3 Mach number and at sea level, is placed into the Simulink model given in Figure 6.2. Total state number of this aeroelastic plant model is 139 and it is composed of 26 structural, 104 aerodynamic lag and 9 sensor states.

This system is simulated by a 5^o control surface rotation impulse input with a duration of one second for each control surface; antisymmetric ailerons, elevator and rudder inputs, respectively. The input of the simulation is given in Figure 6.3.

The output of this simulation with aileron input is the angular velocity about the x-axis (p), with elevator input is the angular velocity about the y-axis (q) and with rudder input is the angular velocity about the z-axis (r). Simulation is performed for the open-loop system by breaking the feedback loop and also for the closed-loop system. The results are presented in between Figure 6.4 and Figure 6.6 and it can be concluded that, flight control algorithm works well with the aeroelastic plant model without any divergent behaviour in terms of oscillations and it decreases the amplitude of the open-loop oscillations, therefore it can be used in aeroservoelastic analysis.

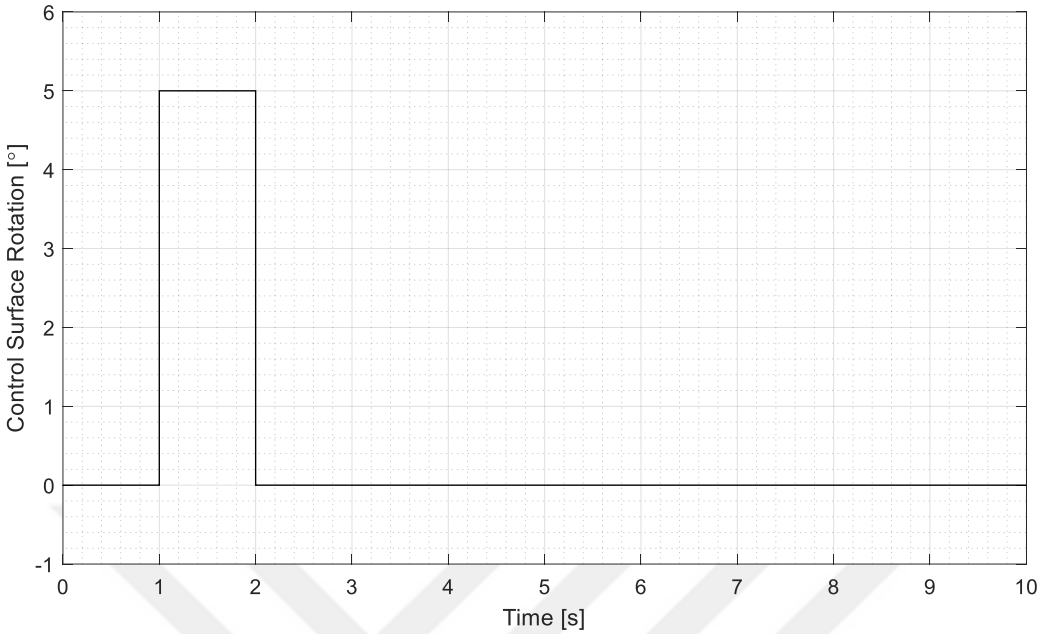

Figure 6.3 Control Surface Rotations Used in Simulations

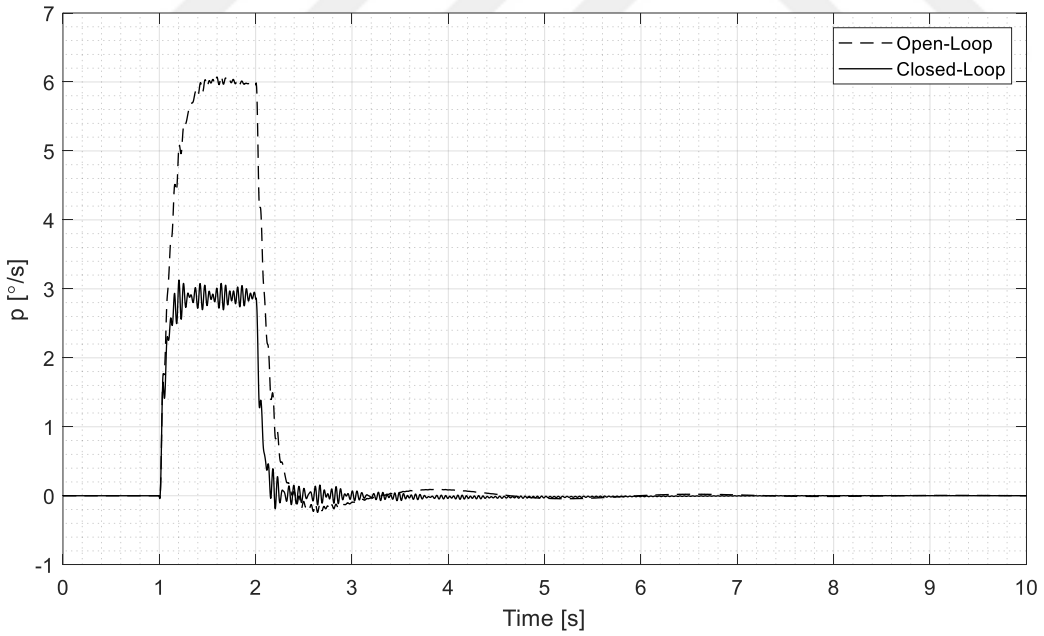

Figure 6.4 Simulation Results of Angular Velocity about x-axis (p) vs Time

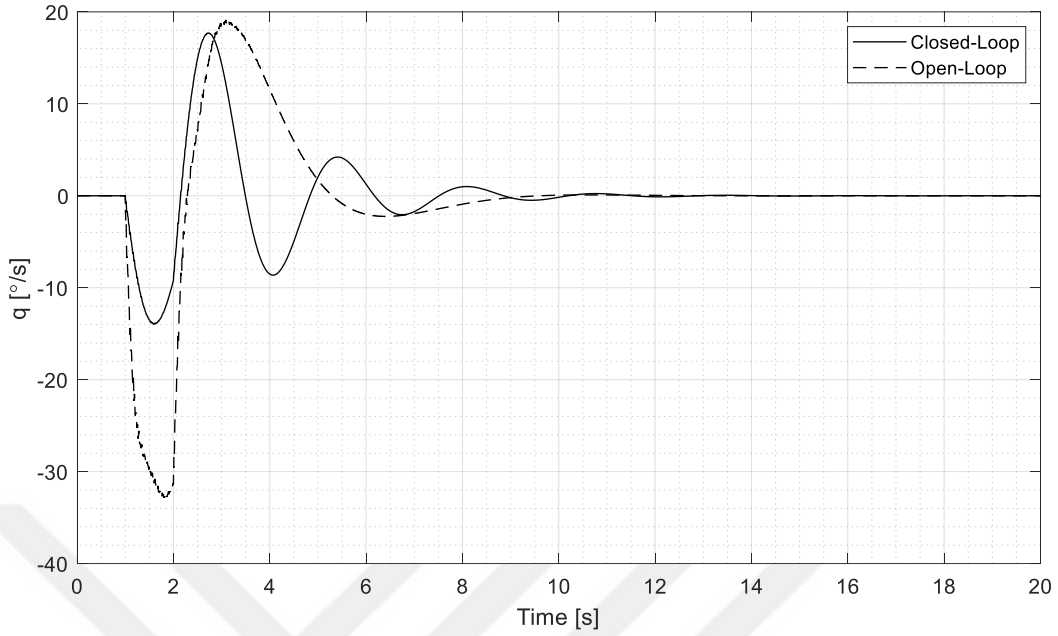

Figure 6.5 Simulation Results of Angular Velocity about y-axis (q) vs Time

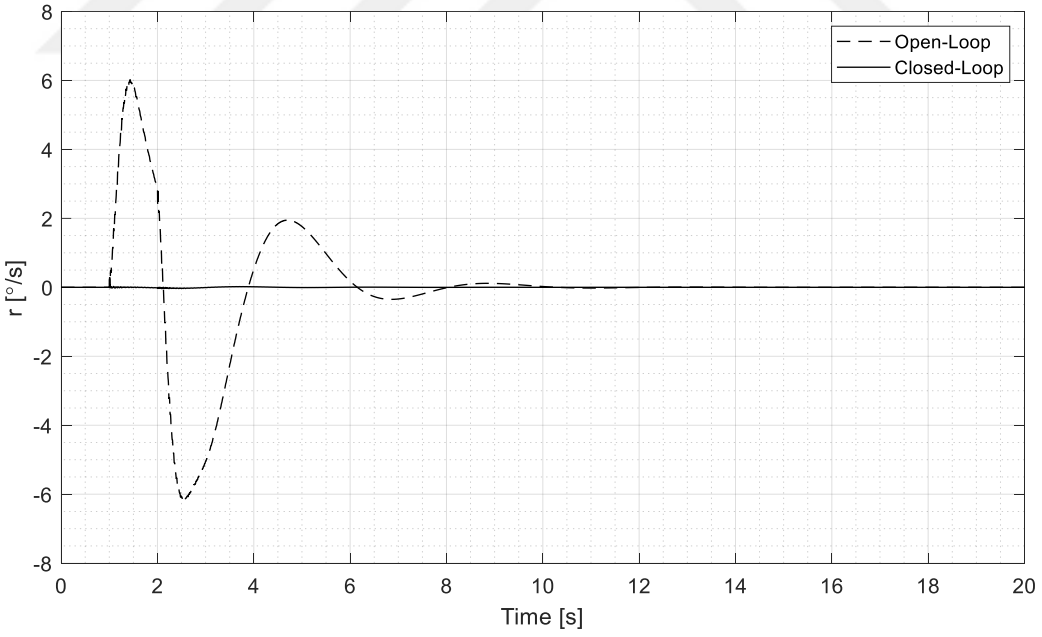

Figure 6.6 Simulation Results of Angular Velocity about z-axis (r) vs Time

6.4 Freeplay Implementation

The mathematical modeling of the freeplay nonlinearity is the first major subtopic in the theoretical research of freeplay [26]. In literature, many methods have been introduced and used [22], [52], [53], [30]. In this study, most common approach is utilized with the correction of the offset moment [20]. The schematic diagrams of freeplay modelling without offset moment are shown in Figure 6.7.

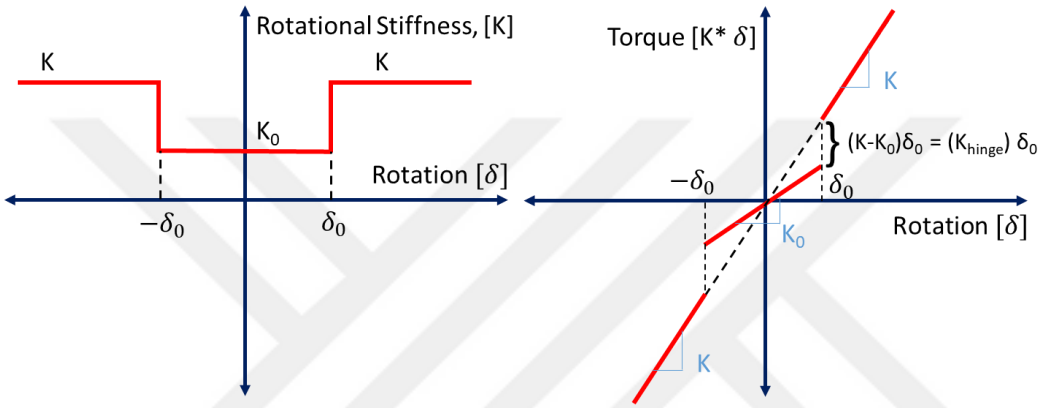

Figure 6.7 Schematic Diagram of Freeplay Modelling without Offset Moment

In Figure 6.7, δ_0 is the freeplay angle, K and K_0 are the nominal and freeplay stiffness values, respectively. As one can see from Figure 6.7, at the freeplay boundaries ($-\delta_0$ and $+\delta_0$) there are jump discontinuities in the stiffness and this can lead to unrealistic bigger limit cycle oscillation. For this reason, freeplay modelling needs to be modified [54] with the inclusion of offset moment, as shown in Figure 6.8.

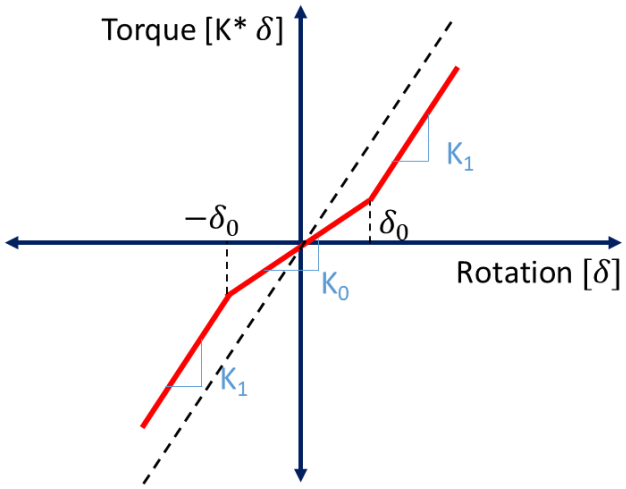

Figure 6.8 Schematic Diagram of Freeplay Modelling with Offset Moment

The governing equations of aeroelastic problem without damping can be re-written by using Equation (4.15) and simplifying the right side of the equation such as:

$$[\bar{M}]\{\ddot{\xi}\} + [\bar{K}]\{\xi\} - q_\infty[Q(ik)]\{\xi\} = \{0\} \tag{6.32}$$

where, the right side of the Equation (6.32) can be expanded as:

$$[Q] = [Q(ik)] = [Q_{hh}(ik)] + [Q_{hc}(ik)] \tag{6.33}$$

It should be noted that, the terms are in Equation (6.32-6.33) are generalized terms with the mode shape matrix ($[\phi]$) of the aircraft structure without any freeplay. Therefore, $[\bar{M}]$,$[\bar{K}]$ and $[Q]$ matrices are the generalized mass, stiffness and aerodynamic force matrix respectively. $\{\xi\}$ is generalized coordinates which is given in Equation (4.9). In order to overcome nonlinearity and implement freeplay nonlinear behaviour to aeroservoelastic system, Equation (6.32) is written in three linear regions as given by Equations (6.34)-(6.36). Then, with the inclusion of the offset moment corrections at the right side of the equations, the three governing equations of nonlinear aeroelastic problem becomes,

$$[\bar{M}]\{\ddot{\bar{\xi}}\} + [\bar{K}]\{\xi\} - q_\infty[Q]\{\xi\} = [\phi]^T\left[K_{hinge}\right]\{\delta_0\} \qquad \text{for } \delta > \delta_0 \quad (6.34)$$

$$[\bar{M}]\{\ddot{\bar{\xi}}\} + [\overline{K_0}]\{\xi\} - q_\infty[Q]\{\xi\} = 0 \qquad \text{for } \delta_0 \geq \delta \geq -\delta_0 \quad (6.35)$$

$$[\bar{M}]\{\ddot{\bar{\xi}}\} + [\bar{K}]\{\xi\} - q_\infty[Q]\{\xi\} = -[\phi]^T\left[K_{hinge}\right]\{\delta_0\} \qquad \text{for } \delta < -\delta_0 \quad (6.36)$$

where $[\overline{K_0}]$ denotes the generalized stiffness matrix in freeplay region which can be obtained the changing nominal control surface rotational stiffness with respect to hinge axis which is given in Table 3.3, and $[\phi]^T\left[K_{hinge}\right]\{\delta_0\}$ terms are the offset moment corrections inside and outside of the freeplay regions with respect to control surface rotation δ_0. K_{hinge} stiffness matrix can be obtained by subtracting the non-generalized stiffness matrix in freeplay region from nominal non-generalized stiffness matrix as given in Equation (6.37).

$$\left[K_{hinge}\right] = [K] - [K_0] \quad (6.37)$$

The sizes of these three different stiffness matrices are identical and $\left[K_{hinge}\right]$ is a full of zero matrix except the corresponding degree of freedom which is related with the control surface rotational stiffness. $[K_0]$ matrix differs from $[K]$ only at the relevant degree of freedom.

With this offset moment correction, the nonlinearity explained in Figure 6.7 is eliminated and smooth stiffness change by allocating restoring moments according to the freeplay region, in control surface rotation is obtained, which is represented in Figure 6.8. Equations (6.34)-(6.36) can be used in the solution of aeroelastic problems with freeplay and this method of solution may be named as the direct method.

6.5 Fictitious Mass Implementation

Fictitious mass approach was firstly presented by Karpel et. al. [16] and there are several usages in the literature [17],[18],[19]. Nowadays, this approach is widely accepted in order to represent large structural deformations such as freeplay. Although nonlinear aeroelastic or aeroservoelastic analysis with freeplay motion can be performed without using fictitious mass approach which is called as direct approach. Fictitious mass approach has advantages such as decreasing computational time and increasing accuracy.

In order to implement the fictitious mass approach to represent the freeplay at the control surfaces, a large inertial mass is placed at the hinge of the control surfaces to the nominal structural dynamics model. This insubstantial inertial mass corresponds to the rotational axis of the control surface with respect to its hinge axis and the existence of this large inertia enforces control surface rotational mode shapes to occur at lower frequencies. Fictitious mass approach in FE modelling is a trial-error procedure and in its implementation, one has to be sure about that the frequency of the rigid body rotation of the control surface is near zero and the associated mode shape does not interact with the other aircraft mode shapes. In this study, the rotational inertia value of the fictitious mass is 10^5 kg.mm^2 for aileron freeplay case, 10^6 kg.mm^2 for elevator and rudder freeplay cases. In the case of two different control surface freeplay, which is elevator and right aileron case in this study, two different fictitious masses are placed to these control surfaces. Fictitious masses of the single control surface freeplays are used in the case of multiple freeplay case.

Then, a modal analysis is conducted with fictitious mass and mass normalized mode shape matrix ($[\phi_{FM}]$) is obtained. Using the nominal mass and stiffness matrices which refer to the nominal structural dynamics model, generalized mass and stiffness matrices are determined according to Equations (6.38-6.39).

$$[\bar{M}_{FM}] = [\phi_{FM}]^T [M_{nom}][\phi_{FM}] \tag{6.38}$$

$$[\overline{K}_{FM}] = [\phi_{FM}]^T [K_{nom}][\phi_{FM}] \tag{6.39}$$

In this equations, nominal mass and stiffness matrices are denoted by M_{nom} and K_{nom} respectively. $\overline{M}_{FM}$ and $\overline{K}_{FM}$ are generalized version of the nominal mass and stiffness matrices with respect to mass normalized mode shape vector of the aircraft model with the fictitious mass ($[\phi_{FM}]$). If fictitious mass approach is not utilized, outside of the freeplay region, Equations (6.38-6.39) can be written as given by Equations (6.40-6.41).

$$[\overline{M}_{nom}] = [\phi_{nom}]^T [M_{nom}][\phi_{nom}] \tag{6.40}$$

$$[\overline{K}_{nom}] = [\phi_{nom}]^T [K_{nom}][\phi_{nom}] \tag{6.41}$$

It can be concluded by comparing Equation (6.38) and Equation (6.40) that, whether the fictitious mass approach is utilized or not, same global mass matrix is used in both approaches. The only difference is the modal matrix which is used in generalization. Then, Equations (6.34-6.36) can be rewritten by using the generalized mass and stiffness matrix which are obtained by the fictitious mass approach as,

$$[\overline{M}_{FM}]\{\ddot{\xi}_{FM}\} + [\overline{K}_{FM}]\{\xi_{FM}\} - q_\infty [Q_{FM}]\{\xi_{FM}\} = [\phi_{FM}]^T [K_{hinge}]\{\delta_0\} \qquad \boldsymbol{\delta > \delta_0} \tag{6.42}$$

$$[\overline{M}_{FM}]\{\ddot{\xi}_{FM}\} + [\overline{K}_{0/FM}]\{\xi_{FM}\} - q_\infty [Q_{FM}]\{\xi_{FM}\} = 0 \qquad \boldsymbol{\delta_0 \geq \delta \geq -\delta_0} \tag{6.43}$$

$$[\overline{M}_{FM}]\{\ddot{\xi}_{FM}\} + [\overline{K}_{FM}]\{\xi_{FM}\} - q_\infty [Q_{FM}]\{\xi_{FM}\} = -[\phi_{FM}]^T [K_{hinge}]\{\delta_0\} \quad \boldsymbol{\delta < -\delta_0} \tag{6.44}$$

where,

$$[\overline{M}_{FM}] = [\phi_{FM}]^T [M_{nom}][\phi_{FM}] \tag{6.45}$$

$$[\overline{K}_{FM}] = [\phi_{FM}]^T [K_{nom}][\phi_{FM}] \tag{6.46}$$

$$[Q_{FM}] = [\phi_{FM}]^T [G]^T [AIC(ik)][G][\phi_{FM}] \tag{6.47}$$

$$[\overline{K}_{0/FM}] = [\phi_{FM}]^T [K_0][\phi_{FM}] \tag{6.48}$$

The objective of the FM method is to generate one set of modes that contain elastic modes outside and inside the freeplay region. Some advantages of using the fictitious mass approach are explained in the following. When there is a structural modification such as freeplay, stiffness or mass change, if the modal matrix of the original system without this structural modification is used in obtaining the generalized equations of the system with the structural modification, then to achieve a reasonable level of accuracy in the output such as frequencies of the system or any aeroelastic analysis output, then relatively high number of modes of the system without the structural modification has to be used. In the direct method of solution, modal matrix ($[\phi]$) used in Equations (6.42-6.44) is the one used in generalizing the equations both in the regions without freeplay, hence without structural modification, and in the region with freeplay, hence with structural modification. In this case very high number of modes of the system without any structural modification has to be used to generate the modal matrix [17]. In large scale problems such as the one in aircraft level, this increases the computational time significantly if a sufficient level of accuracy is desired.

Another way of implementing the direct method is to use separate modal matrices in the region without the freeplay and in the region with the freeplay. In this case, corresponding equations for Equations (6.49-6.51) would be in the following forms:

For $\delta > \delta_0$:

$$[\bar{M}_{nom}]\{\ddot{\xi}_{nom}\} + [\bar{K}_{nom}]\{\xi_{nom}\} - q_\infty[Q_{nom}]\{\xi_{nom}\} = [\phi_{nom}]^T[K_{hinge}]\{\delta_0\} \qquad (6.49)$$

for $\delta_0 \geq \delta \geq -\delta_0$:

$$[\bar{M}_{free}]\{\ddot{\xi}_{free}\} + \left[\bar{K}_{0_{free}}\right]\{\xi_{free}\} - q_\infty[Q_{free}]\{\xi_{free}\} = 0 \qquad (6.50)$$

for $\delta < -\delta_0$:

$$[\bar{M}_{nom}]\{\ddot{\xi}_{nom}\} + [\bar{K}_{nom}]\{\xi_{nom}\} - q_\infty[Q_{nom}]\{\xi_{nom}\} = -[\phi_{nom}]^T[K_{hinge}]\{\delta_0\} \qquad (6.51)$$

where,

$$[\bar{M}_{free}] = [\phi_{free}]^T [M_{nom}][\phi_{free}] \tag{6.52}$$

$$\left[\bar{K}_{0_{free}}\right] = [\phi_{free}]^T [K_0][\phi_{free}] \tag{6.53}$$

$$[\bar{Q}_{free}] = [\phi_{free}]^T [G]^T [AIC(ik)][G][\phi_{free}] \tag{6.54}$$

Equations (6.49)-(6.51) would suitably be used for flutter analysis in separate regions with and without freeplay. For dynamic response type analysis, time domain solution would require switching of the modal matrix used for the generalization of the equations from $[\phi_{nom}]$ to $[\phi_{free}]$ and vice versa. Moreover, stiffness matrices in both regions would have to be switched from $[K_{nom}]$ to $\left[\bar{K}_{0_{free}}\right]$ and vice versa. On the other hand, when the fictitious mass approach is used, as given by Equations (6.42-6.44), only a single modal matrix $[\emptyset_{FM}]$ is used. Moreover, the number of modes to be included in the modal matrix of the system with the fictitious mass is considerably less than the number of modes to be included in the modal matrix of the system in the direct method without freeplay and fictitious mass.

Wing bending mode shape, one of the primary mode shapes, are presented in Figure 6.9 and Figure 6.10. In Figure 6.9, wing bending mode shape calculated by the direct approach is shown in the freeplay region. As seen in Figure 6.9, the freeplay control surface deflection is very high in the wind bending mode. In Figure 6.10, wing bending mode shape calculated by the fictitious mass approach is shown in the freeplay region. In this case, because of the large fictitious mass added to the hinge axis, control surface deflection cannot be observed in the wing bending mode.

The comparison of the natural frequencies of the modal solution inside the freeplay region with the direct approach and FM approach is given in Table 6.7. The aileron symmetric bending and antisymmetric rigid body rotations occur around 32 Hz in nominal case, because in the nominal case there is no freeplay.

Table 6.7 Comparison of Natural Frequencies between the FM and Direct Method Approaches for the Aileron Freeplay

Mode Shape #	*Nominal Case*[1] *[Hz]*	*FM Approach*[2] *[Hz]*	*Direct Approach*[3] *[Hz]*
The First Wing Bending	10.328	10.334	10.423
2	18.568	18.589	18.630
3	19.476	19.476	19.477
4	20.392	20.391	20.392
5	22.083	22.083	22.083
6	23.225	23.298	23.336
7	24.624	24.636	24.639
8	24.988	24.999	24.997
9	30.414	30.426	30.427
Aileron Symmetric Bending	**32.083**	**1.589**	**1.217**
Aileron Antisymmetric Bending	**32.120**	**1.592**	**1.223**
12	33.173	33.166	33.166
13	35.974	35.969	35.969

From Table 6.7, it can be concluded that, FM approach allows the correct calculation of the frequencies of the aircraft both in the freeplay region and outside the freeplay region.

[1] In the nominal case, the structural dynamic FE model without any freeplay that is used in Section 3 is used.
[2] The natural frequencies are obtained without any modal reduction for the case of aileron freeplay with direct approach.
[3] The natural frequencies are obtained without any modal reduction for the case of aileron freeplay with FM approach.

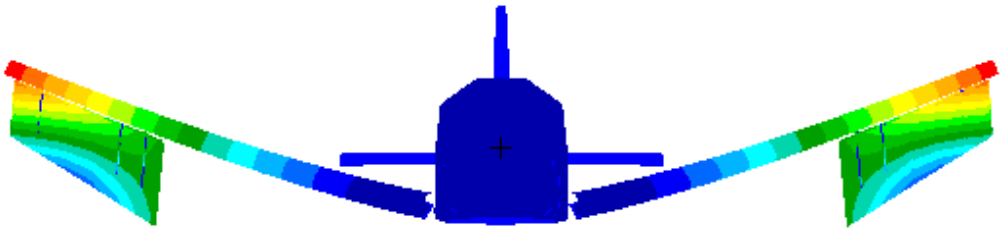

Figure 6.9 Mode Shape of the Wing Bending with the Direct Approach

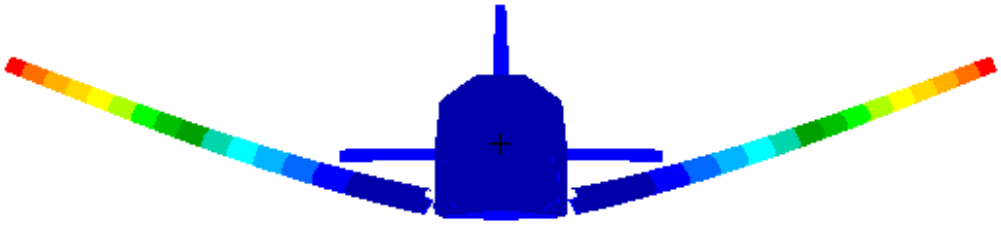

Figure 6.10 Mode Shape of the Wing Bending with the Fictitious Mass Approach

The structural dynamic models in Equations (6.42-6.44) can also be represented as two discrete models, inside and outside the freeplay zone as,

$$\left[-\omega_{FM}^2[\bar{M}_{FM}] + [\bar{K}_{FM}]\right]\{\bar{\xi}_{FM}\} = 0 \qquad for \quad \delta > |\delta_0| \tag{6.55}$$

$$\left[-\omega_{FM/free}^2[\bar{M}_{FM}] + \left[\bar{K}_{0/FM}\right]\right]\{\bar{\xi}_{FM}\} = 0 \qquad for \quad \delta \leq |\delta_0| \tag{6.56}$$

where, $\omega_{FM/free}$ and ω_{FM} represent the natural frequencies of the system in freeplay zone and outside the freeplay zone, which is the nominal case, respectively. In direct approach case, the structural dynamic models in Equations (6.49-6.51) can be expressed in following form:

$$\left[-\omega_{nom}^2[\bar{M}_{nom}] + [\bar{K}_{nom}]\right]\{\bar{\xi}_{nom}\} = 0 \qquad for \quad \delta > |\delta_0| \tag{6.57}$$

$$\left[-\omega_{nom/free}^2\left[\bar{M}_{free}\right] + \left[\bar{K}_{0_{free}}\right]\right]\{\bar{\xi}_{free}\} = 0 \qquad for \quad \delta \leq |\delta_0| \tag{6.58}$$

here, ω_{nom} and $\omega_{nom/free}$ represent the natural frequencies of the system in the freeplay zone and outside the freeplay zone, which is the nominal case, respectively. The natural frequencies obtained by the fictitious mass approach and the direct method) are solved numerically by using the relevant generalized mass and stiffness matrices in these equations and they are compared in Table 6.8 for the case of rudder freeplay.

Table 6.8 Comparison of Natural Frequencies between the FM and Direct Method Approaches with and without Rudder Freeplay

#	Mode Shape	Exact Solution		Direct Approach		FM Approach	
		Without Freeplay	With Freeplay	ω_{nom} (Hz)	$\omega_{nom/free}$ (Hz)	ω_{FM} (Hz)	$\omega_{FM/free}$ (Hz)
1		10.328	10.328	10.319	10.319	10.319	10.319
2		18.568	18.587	18.576	18.584	18.587	18.591
3	Rudder Rotation	**19.476**	**0.162**	**19.823**	**0.175**	**19.571**	**1.716**
4		20.392	20.390	20.392	20.392	20.400	20.400
5		22.083	22.082	22.083	22.083	22.101	22.101
6		23.255	23.253	23.255	23.255	23.261	23.259
7		24.624	24.604	24.632	24.616	24.657	24.627
8		24.988	24.982	24.988	24.988	24.988	24.988
9		30.414	30.413	30.452	30.452	30.414	30.414
10		32.083	32.083	32.083	32.083	32.083	32.083
11		32.120	32.119	32.120	32.120	32.120	32.120
12		33.173	33.139	33.173	33.148	33.361	33.349
13	Vertical Tail Bending	**35.974**	**35.894**	**34.835**	**35.896**	**35.982**	**35.982**

In Table 6.8, the exact solution of the natural frequencies is obtained with full-sized (not generalized) mass and stiffness matrices of the structural dynamic system; hence it is referred as the exact solution. In this example, FM is used to represent the rudder

freeplay, therefore natural frequencies of the rudder rotation and vertical tail bending mode shapes are the most affected ones in this case. Firstly, the natural frequency of the rudder rotation mode shape outside the freeplay region (19.476 Hz in exact solution) is captured accurately with the FM approach (19.571 Hz). Moreover, the natural frequency of vertical tail bending mode shape outside of freeplay region (35.974 Hz in exact solution) is also captured accurately with FM the approach (35.982 Hz).

6.6 Governing Equation of Motion

The aeroelastic model equations given in Equations (6.12-6.13)includes the mass, stiffness and aerodynamic models of the very light aircraft. Then, aeroelastic plant model is obtained by adding actuator states of the control surfaces to aeroelastic model and state-space representation of aeroelastic plant model is presented in Equations (6.18-6.19). Aeroelastic plant model contains the aeroelastic model as well as control surface states with their dynamic behavior.

In this study, to solve nonlinear system with freeplay in control surfaces, the aeroelastic plant model is divided into three sub-linear aeroelastic regions by utilizing the offset moment correction and fictitious mass approach as given by Equations (6.42-6.44). Therefore, for a specific flight condition, Mach number and altitude, and a control surface with freeplay, three aeroelastic plant models are obtained.

The next step is to include flight control algorithm states into aeroelastic plant equations to obtain the vehicle or aeroservoelastic level equations, which are denoted with subscript *v*, in state-space domain as,

$$\{\dot{x_v}\} = [A_v]\{x_v\} + [B_v]\{u_v\} \tag{6.59}$$

$$\{y_v\} = [C_v]\{x_v\} \tag{6.60}$$

$$\{x_v\} = \begin{Bmatrix} x_p \\ x_c \end{Bmatrix} \tag{6.61}$$

where, x_c is the flight control algorithm states. It should be noted that, nonlinearity due to the freeplay requires more than one plant algorithm to be included; however, flight control algorithm does not change with respect to the plant model. On the other hand, each aeroservoelastic vehicle model corresponds to combination of an aeroelastic plant model and the flight control algorithm which depends only on the flight condition and independent from control surface nonlinearity.

It is worth to mention that all aeroservoelastic vehicle models are obtained in state-space or time domain. Therefore, these vehicle models, which include the freeplay motion of the control surface, can be simulated in discrete time domain directly. Time domain simulation requires time step or time resolution value which determines the time interval between the solution points and also initial condition of the aircraft. In this study, time resolution (*dt*) is used as 0.001 s in all nonlinear aeroelastic analyses and initial condition of the aircraft is taken as level flight, which means that the aircraft is not in a maneuver and it has zero angle of attack and zero side-slip angle. The initial condition of vehicle level equations is given by Equation (6.62).

$$\{x_v\} = \{\dot{x}_v\} = \{0\} \tag{6.62}$$

In this study, to represent the nonlinear aeroservoelastic behaviour, different plant models are used according to the freeplay zone and flight condition with fixed flight control algorithm which also changes with the flight condition. For a specific flight condition with specific control surface with freeplay, the solution algorithm used in this study can be expressed as a schematic diagram as shown in Figure 6.11.

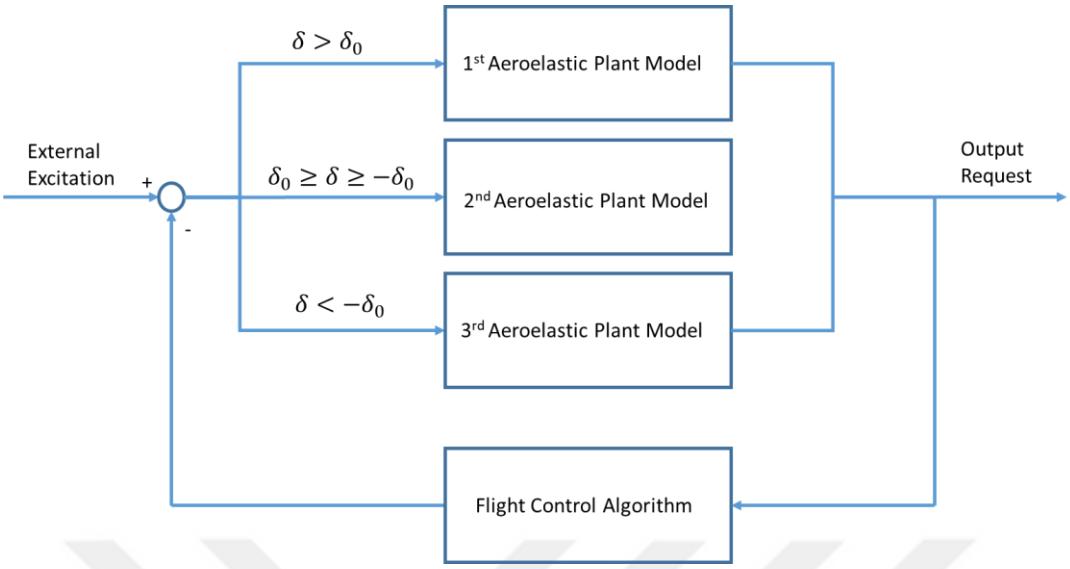

Figure 6.11 Representation of the Nonlinear Aeroservoelastic Analysis

In this figure, as it is stated previously, there are three sub-linear aeroelastic plant model in order to represent the nonlinearity. In the time simulation at any discrete solution point, according to the control surface position at that instant, related aeroelastic plant model is chosen and used. These aeroelastic plant models are nothing but the state-space representation of Equations (6.42-6.44).

The flight control algorithm in this closed-loop system is free from the freeplay motion and it depends only on the flight condition. The inputs of the flight control algorithm are the outputs of aeroelastic plant systems which are obtained by artificially placed sensors at the center of gravity of the aircraft and included in the C_{ae} matrix in Equation (6.13).

6.7 Nonlinear Aeroservoelastic Analysis Results

The results of the nonlinear aeroservoelastic analysis are selected as deformations of some structural grids which are the left or right wing tip, center of gravity (CG) of the aircraft and the hinge axis rotation of the investigated control surface with freeplay. The external excitation of the analysis is selected as a sinusoidal external pilot input for all control surfaces as shown in Figure 6.12.

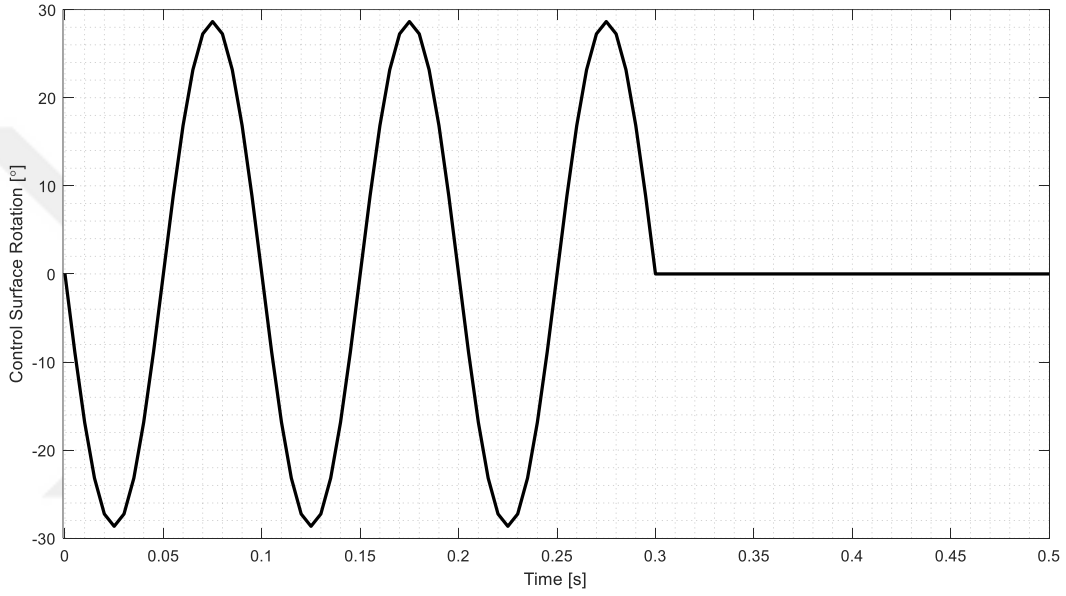

Figure 6.12 Sinusoidal External Excitation

6.7.1 Aileron Freeplay

For the aileron with freeplay, for different freeplay angles (δ_0=0.01º, 0.05º, 0.20º, 0.50º, 1.0º and 2.5º), nonlinear aeroservoelastic analyses are conducted for different Mach numbers at the sea level. The nonlinear dynamic behavior of the aileron due to freeplay at 59.00 m/s which corresponds to 0.173 Mach number is given in Figure 6.13.

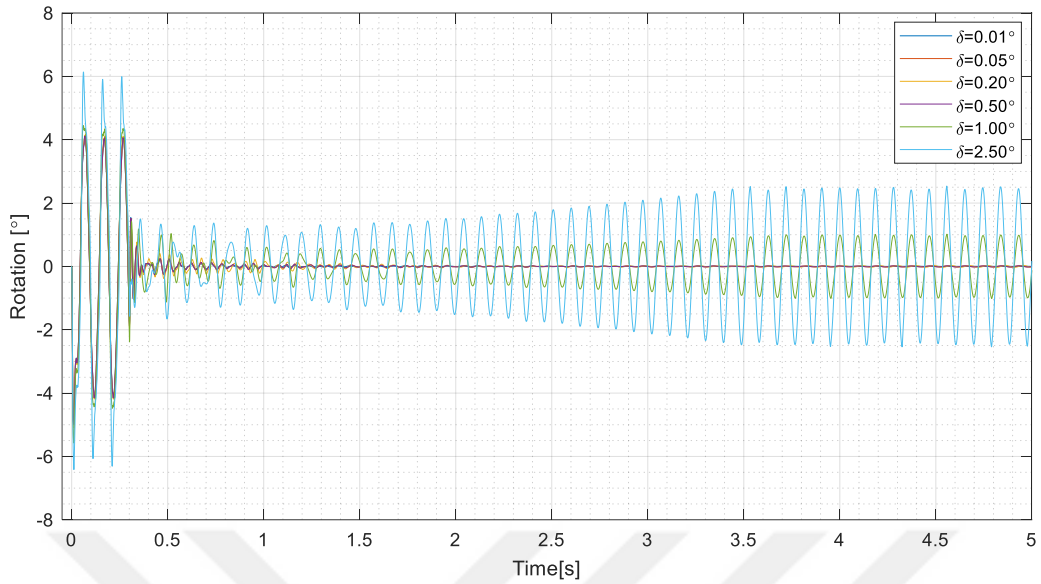

Figure 6.13 Right Aileron Rotation about the Hinge Axis at 59.00 m/s for Different Freeplay Angles

From Figure 6.9, it is observed that for the 59.00 m/s aircraft velocity the disturbance given by the pilot damps out for all aileron freeplay angles except 1.00 º and 2.50 º. These freeplays does not have any divergent behaviour and their damping are very low. However, increasing the velocity of the aircraft to 60.00 m/s, aircraft shows divergent behavior for freeplay angles 1.00 º and 2.50 º only as shown in Figure 6.14. Therefore, limit-cycle oscillation (LCO) behaviour is captured at 59.00 m/s for only freeplay angles which are 1.00 º and 2.50 º. Displacements of the center of gravity of the aircraft in 3 translational degrees of freedom at 59.00 m/s are given in Figure 6.15-6.17. Displacements of the left wing tip in the y and z directions are given in Figure 6.18–6.19.

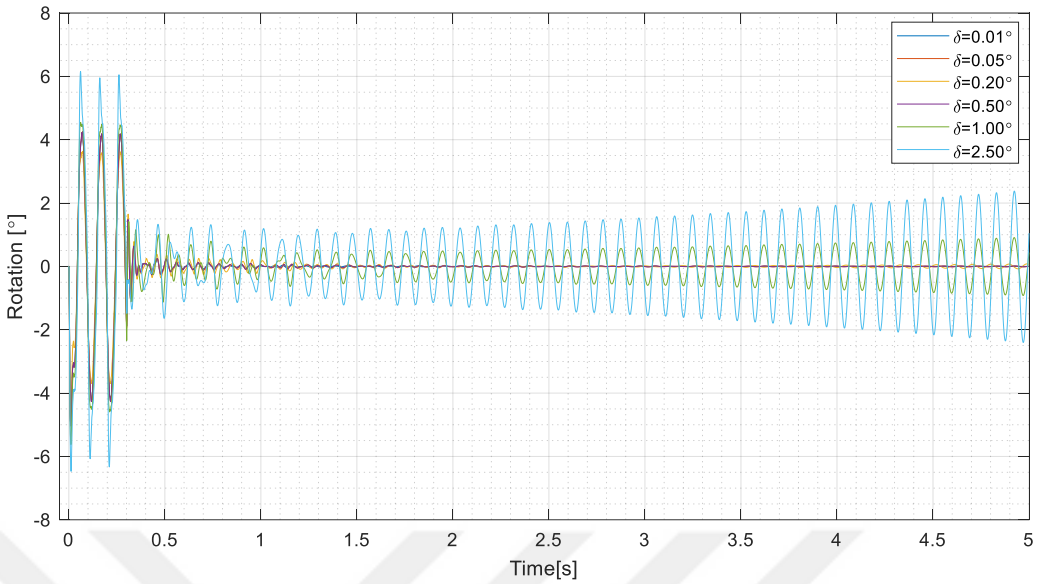

Figure 6.14 Right Aileron Rotation about the Hinge Axis at 60.00 m/s for Different Freeplay Angles

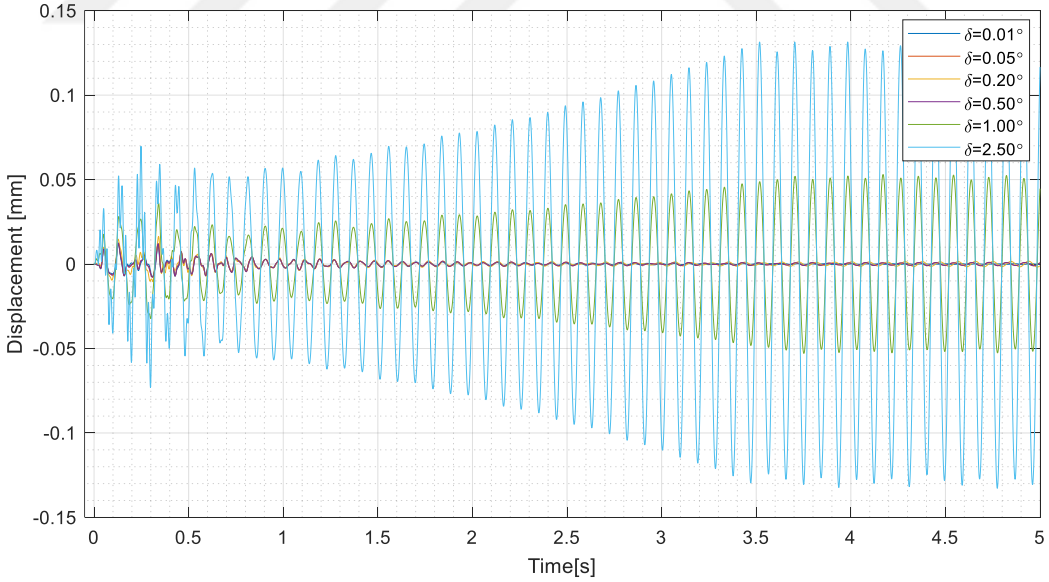

Figure 6.15 Center of Gravity Displacement at 59.00 m/s in the x-direction for Different Aileron Freeplay Angles

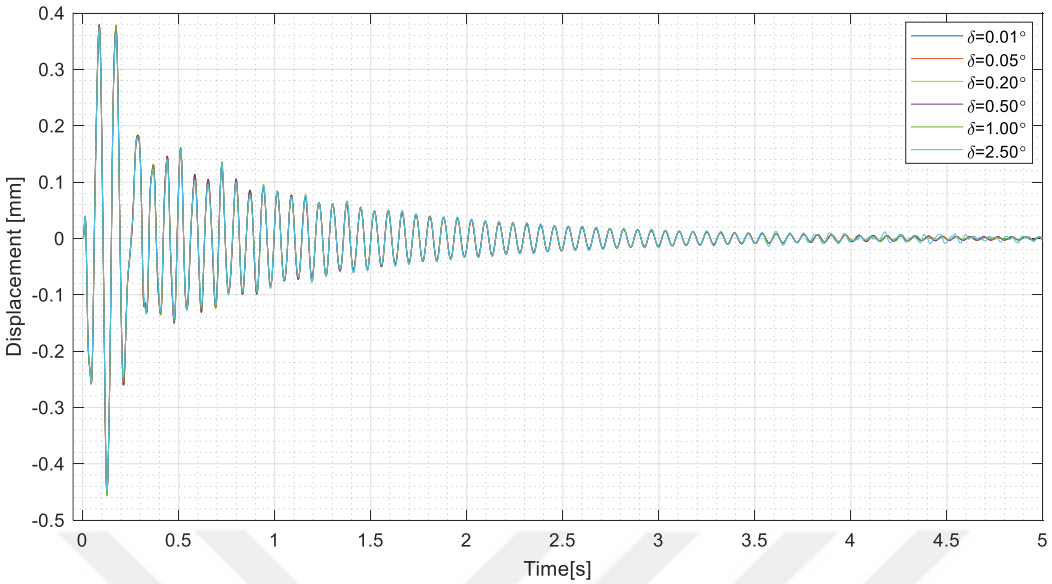

Figure 6.16 Center of Gravity Displacement at 59.00 m/s in y-direction for Different Aileron Freeplay Angles

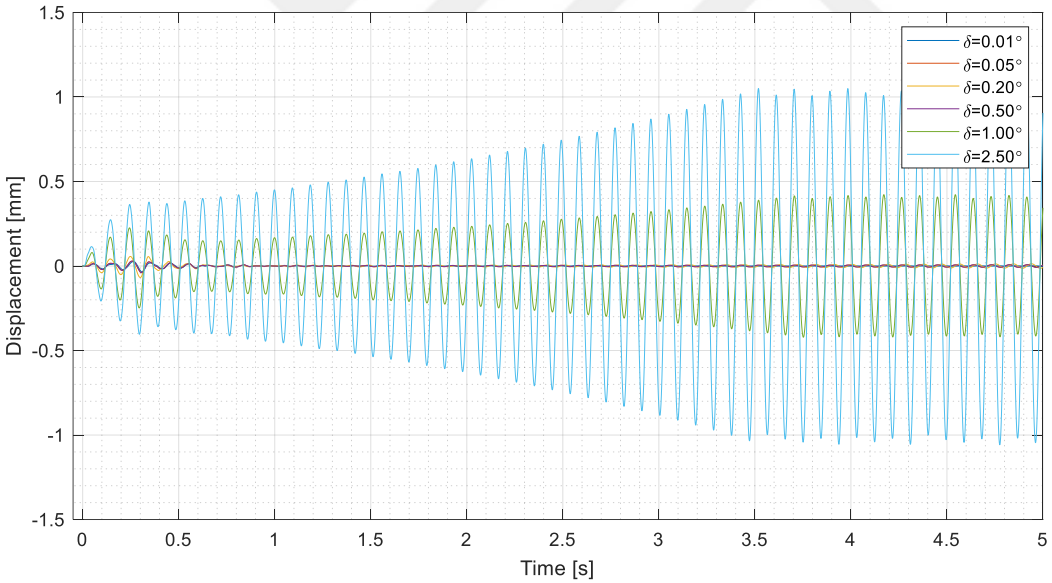

Figure 6.17 Center of Gravity Displacement at 59.00 m/s in z-direction for Different Aileron Freeplay Angles

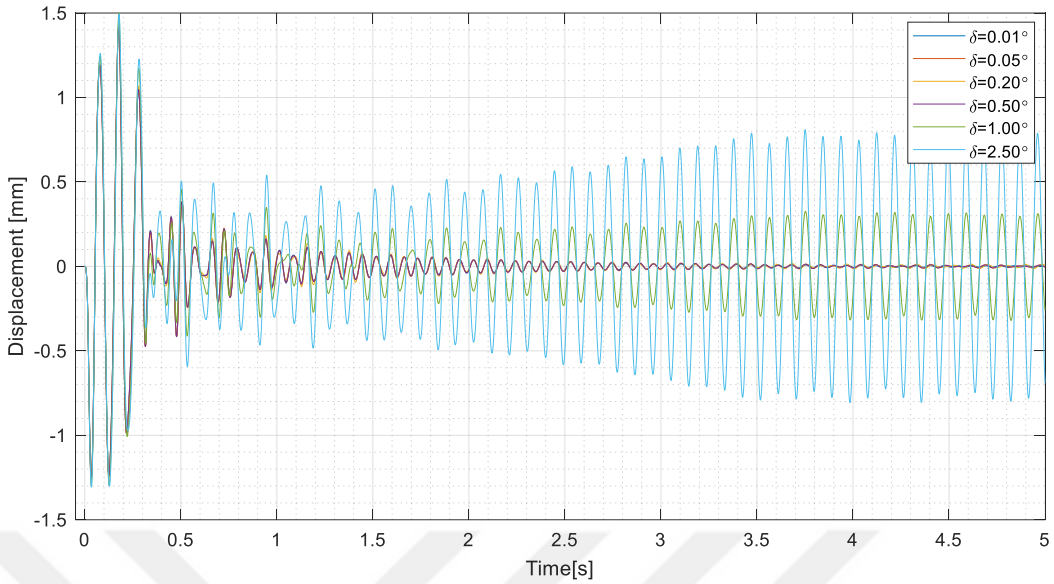

Figure 6.18 Left Wing Tip Displacement at 59.00 m/s in y-direction for Different Aileron Freeplay Angles

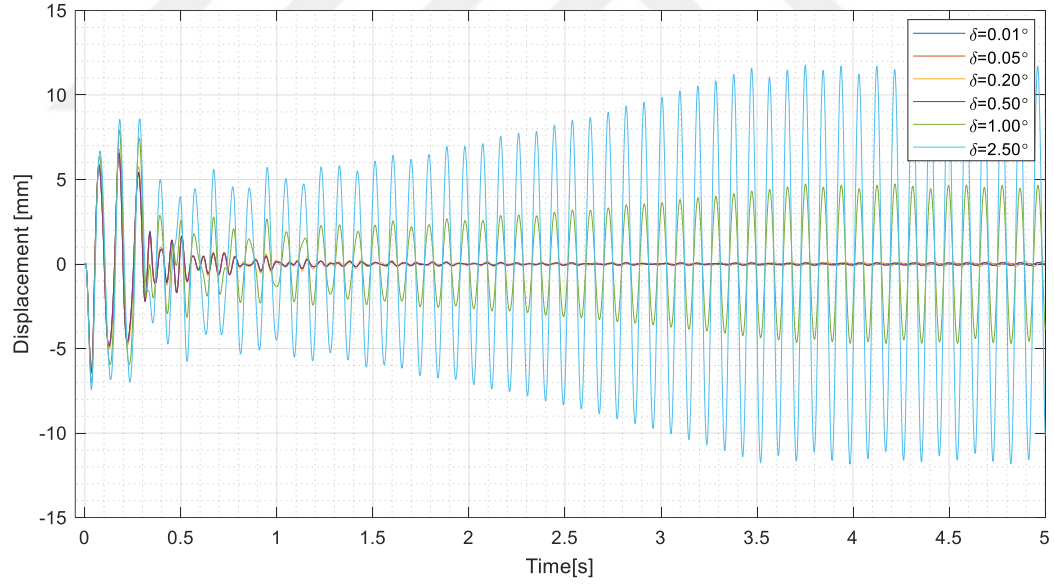

Figure 6.19 Left Wing Tip Displacement at 59.00 m/s in z-direction for Different Aileron Freeplay Angles

6.7.2 Elevator Freeplay

For the elevator with freeplay, for different freeplay angles (δ_0=0.01º, 0.05º, 0.20º, 0.50º, 1.0º and 2.5º), nonlinear aeroservoelastic analyses are conducted for different Mach numbers at the sea level. The elevator rotation about the hinge axis at 245.00 m/s which corresponds to 0.720 Mach number is given in Figure 6.20.

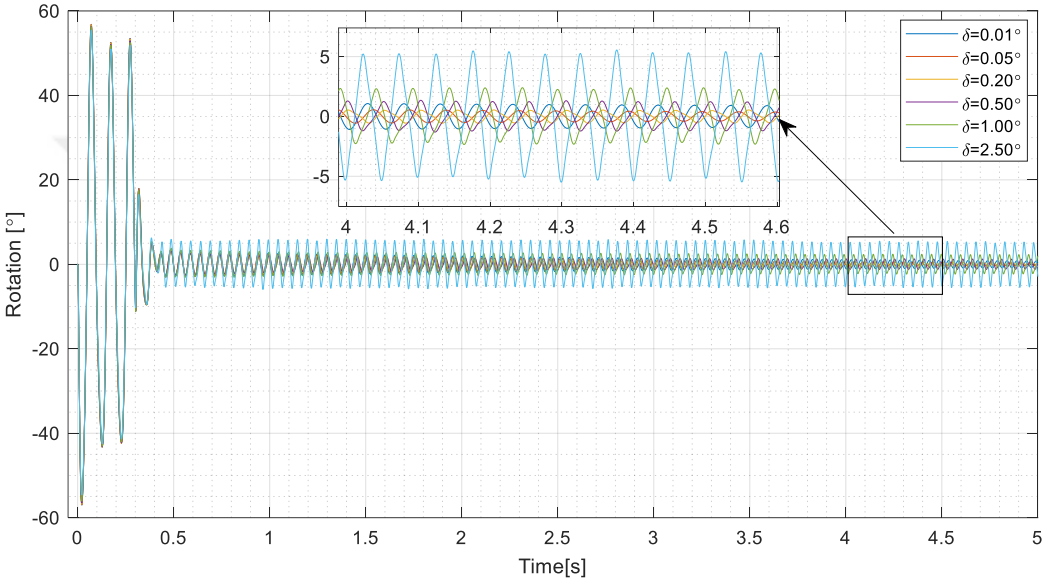

Figure 6.20 Elevator Rotation about the Hinge Axis at 245.00 m/s for Different Freeplay Angles

When the velocity of aircraft is increased to 246.00 m/s, the observed oscillations are getting large and not damping out as seen in Figure 6.21. Therefore, the maximum velocity of the aircraft with LCO behaviour is 245.00 m/s, beyond that velocity, aircraft starts to diverge. Displacements of center of gravity of the aircraft in 3 translational degrees of freedom at 245.00 m/s are given in Figure 6.22-6.24 and the left wing tip displacements in the y and z direction are given in Figure 6.25.

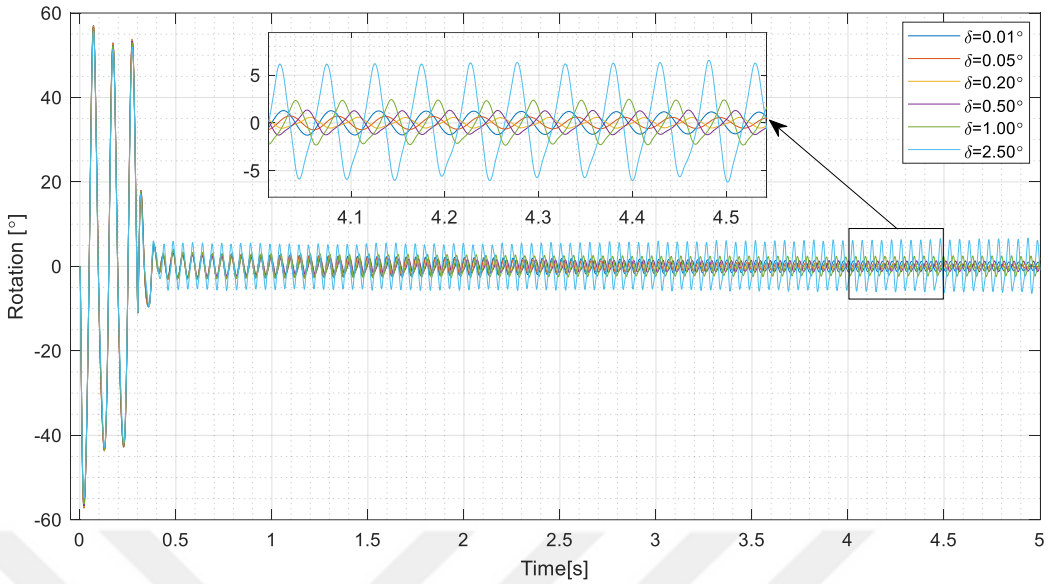

Figure 6.21 Elevator Rotation about the Hinge Axis at 246.00 m/s for Different Freeplay Angles

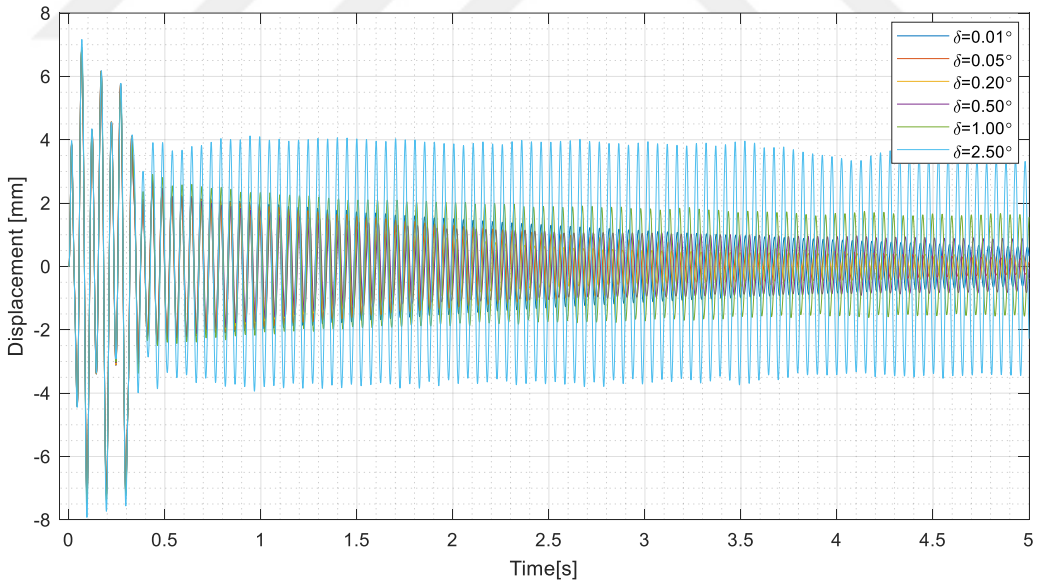

Figure 6.22 Center of Gravity Displacement at 245.00 m/s in the x-direction for Different Elevator Freeplay Angles

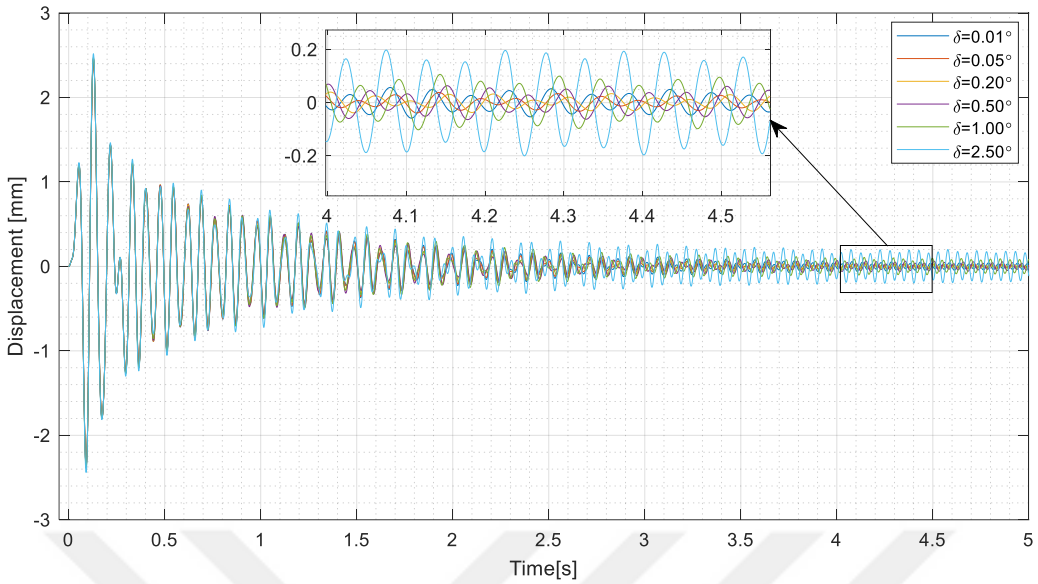

Figure 6.23 Center of Gravity Displacement at 245.00 m/s in the y-direction for Different Elevator Freeplay Angles

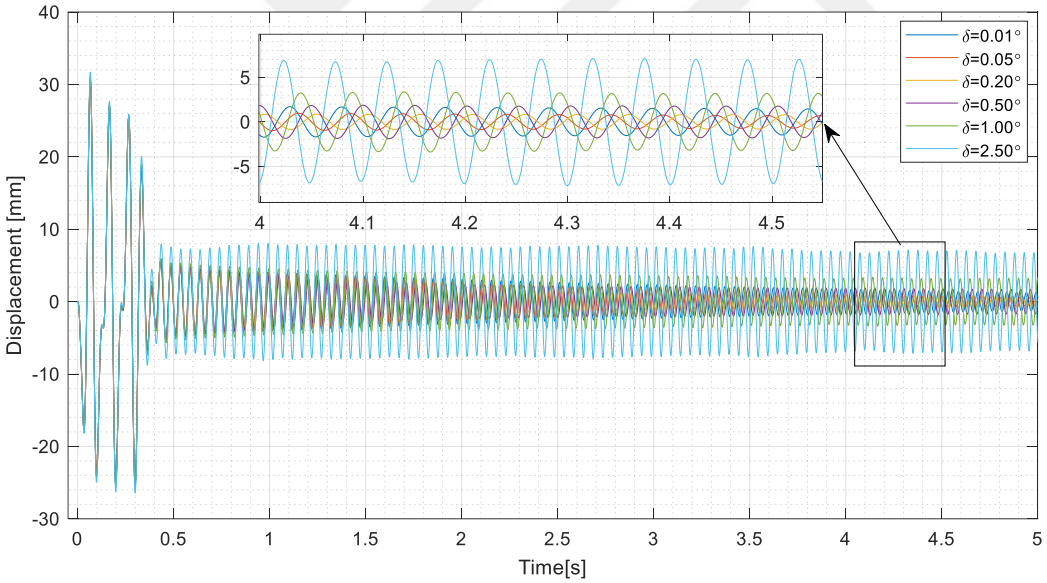

Figure 6.24 Center of Gravity Displacement at 245.00 m/s in the z-direction for Different Elevator Freeplay Angles

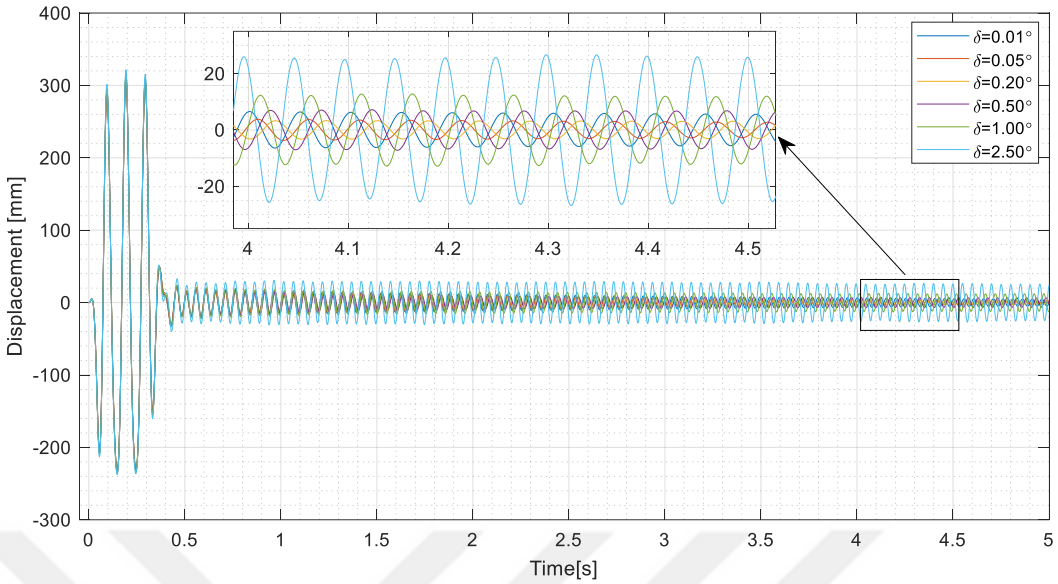

Figure 6.25 Wing tip Displacement at 245.00 m/s in the z-direction for Different Elevator Freeplay Angles

It is noted that when there is freeplay in the elevator, freeplay motion has an effect on the pitch motion of the aircraft resulting in a change in the lift distribution on the wing. Hence, it is deemed that this effect promotes limit cycle oscillation behavior. After the initial excitation, oscillations with constant amplitudes start to occur at about t=0.5 seconds at the center of gravity and wing tip of the aircraft.

It should be also noted that the elevator rotation in Figure 6.21, also causes elastic bending of the horizontal tail. Hence, the elevator rotation has bigger amplitude than the related freeplay angle.

6.7.3 Rudder Freeplay

For the rudder with freeplay, for different freeplay angles (δ0=0.01º, 0.05º, 0.20º, 0.50º, 1.0º and 2.5º), nonlinear aeroservoelastic analyses are conducted for different Mach numbers at the sea level. The nonlinear aeroservoelastic results for different freeplay angles at 68.050 m/s which corresponds to 0.20 Mach is given in Figure 6.26.

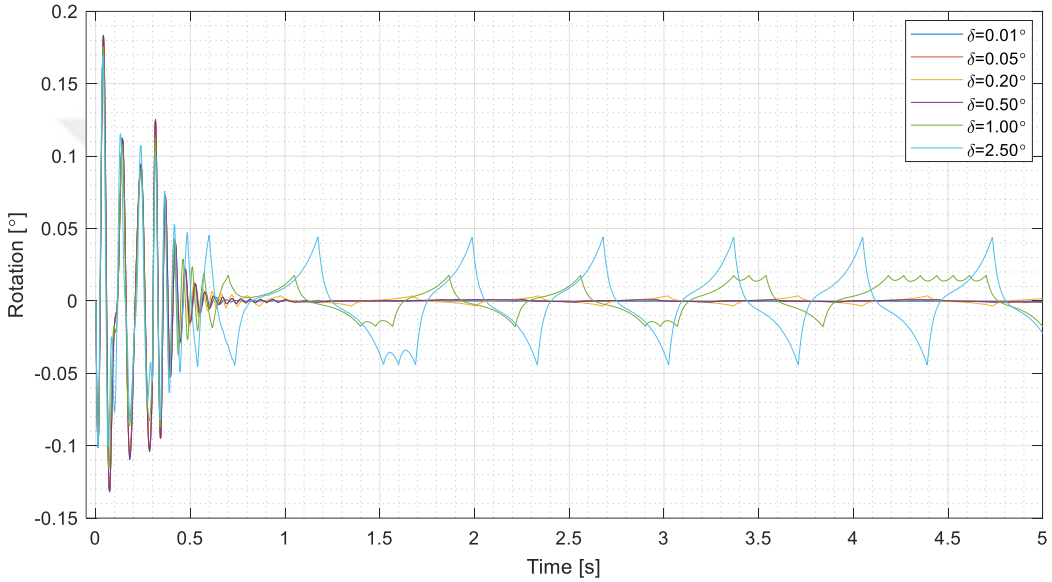

Figure 6.26 Rudder Rotation about the Hinge Axis at 68.050 m/s for Different Freeplay Angles

Displacements of the center of gravity of the aircraft in 3 translational degrees of freedom at 68.050 m/s are given in Figure 6.27-6.29 and wing tip displacement in the z-direction is given in Figure 6.30.

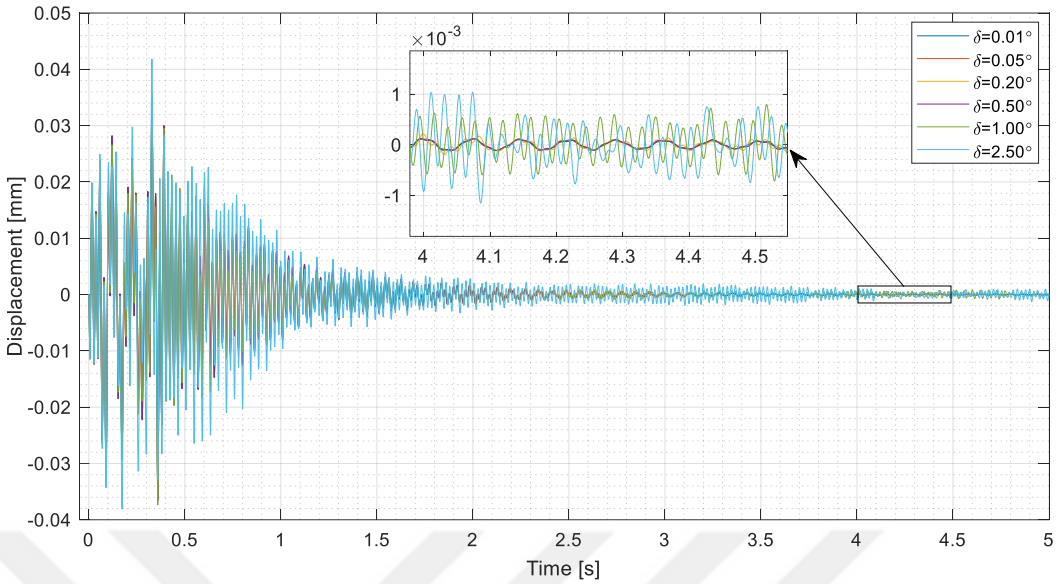

Figure 6.27 Center of Gravity Displacement at 68.050 m/s in x-direction for Different Rudder Freeplay Angles

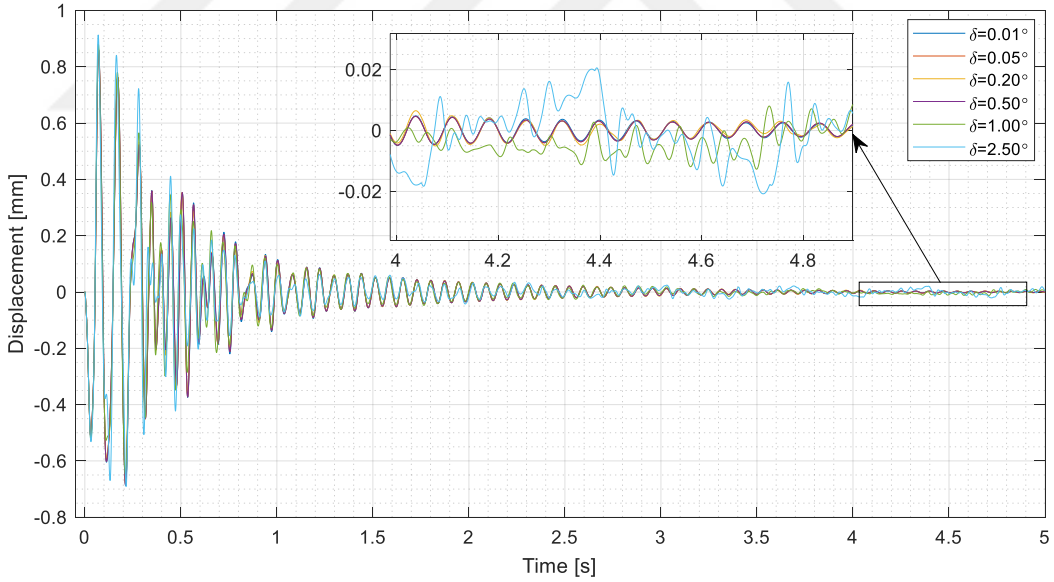

Figure 6.28 Center of Gravity Displacement at 68.050 m/s in y-direction for Different Rudder Freeplay Angles

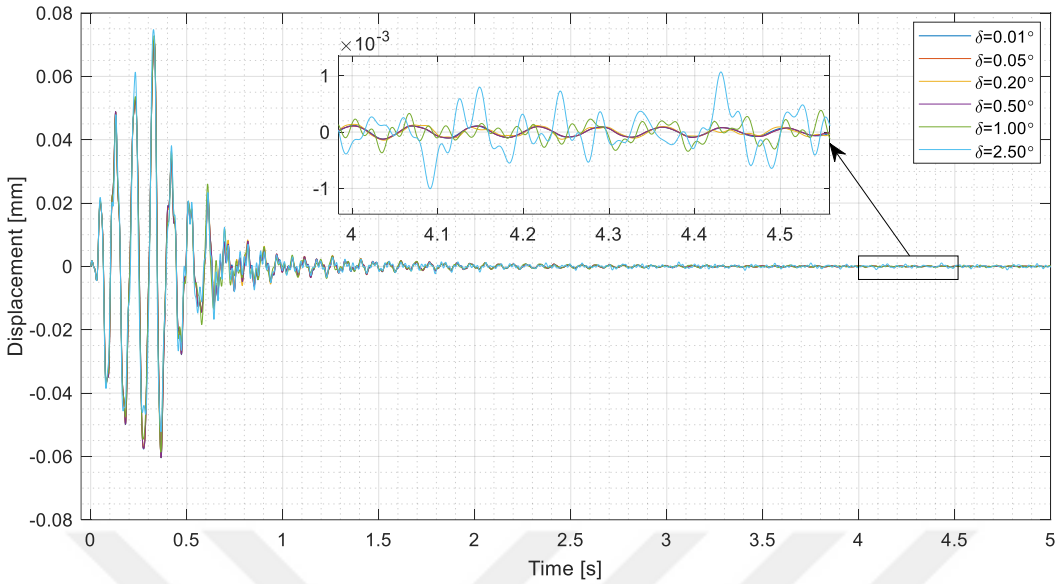

Figure 6.29 Center of Gravity Displacement at 68.050 m/s in z-direction for Different Rudder Freeplay Angles

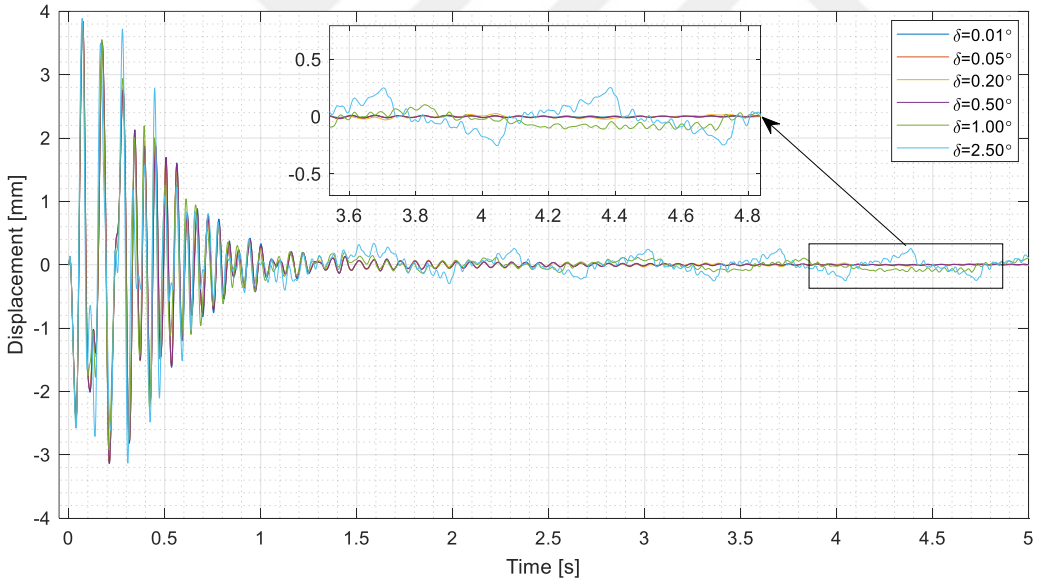

Figure 6.30 Wing tip Displacement at 68.050 m/s in z-direction for Different Rudder Freeplay Angles

On account of the yaw characteristic of the aircraft, freeplay motion of the rudder did not lead to a clear limit cycle oscillations as in elevator. The amplitudes of displacements and rotations are relatively small with respect to aileron and elevator freeplay cases. However, as seen in Figure 6.26, at high freeplay angles amplitude

of the rudder rotation did not diminish in the time interval analyzed and this may be a sign of limit cycle oscillation.

6.7.4 Aileron and Elevator Freeplay

For the right aileron and elevator with freeplay, for different simulataneous freeplay angles ($\delta 0$=0.01^o, 0.05^o, 0.20^o, 0.50^o, 1.0^o and 2.5^o) with same freeplay angles for both control surfaces, nonlinear aeroservoelastic analyses are conducted for different Mach numbers at the sea level. The nonlinear aeroservoelastic analysis results with elevator and right aileron freeplay at the 159.00 m/s are given in Figure 6.31 and Figure 6.32 respectively.

The results at 159.00 m/s show that nonlinear motion of the aircraft is sustained and damped. Therefore, in order to observe limit-cycle oscillation behavior, velocity is increased to 162.00 m/s and control surface rotations are presented in Figure 6.33. According to these results, for aileron and elevator freeplay case, the non-divergent LCO behaviour is observed at 159.00 m/s and displacements of the center of gravity of the aircraft in 3 translational degrees of freedom at this velocity are given in Figure 6.34-6.36 and wing tip displacement in the x and z direction are given in Figure 6.37-6.38.

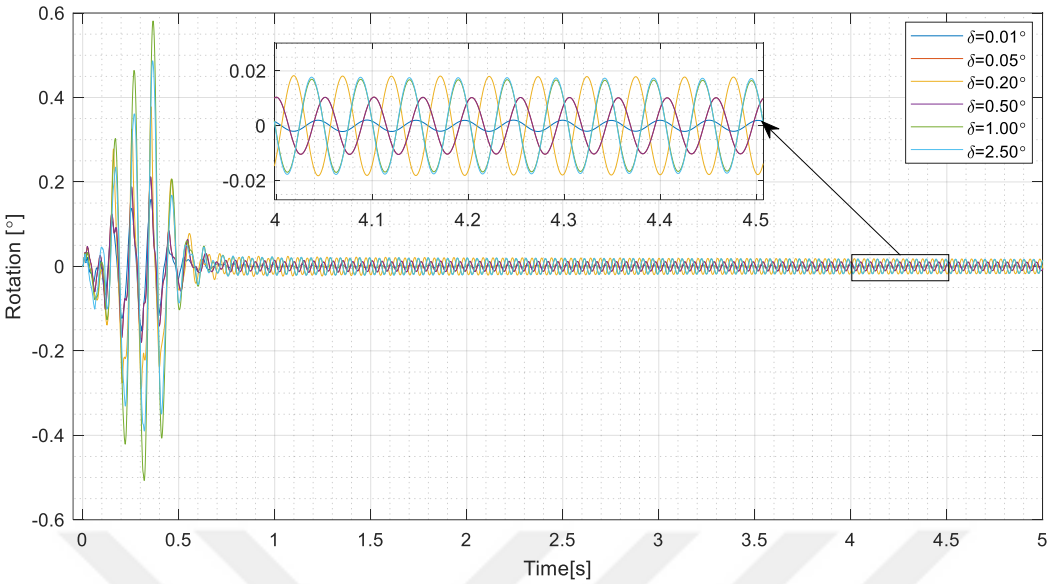

Figure 6.31 Elevator Rotation about the Hinge Axis at 159.00 m/s for Different Freeplay Angles

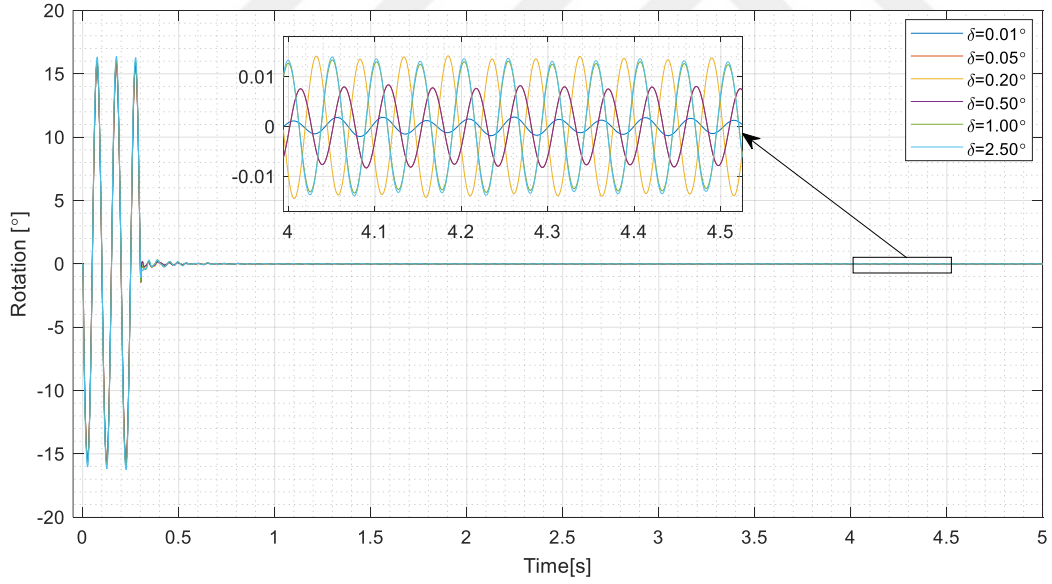

Figure 6.32 Right Aileron Rotation about the Hinge Axis at 159.00 m/s for Different Aileron and Elevator Freeplay Angles

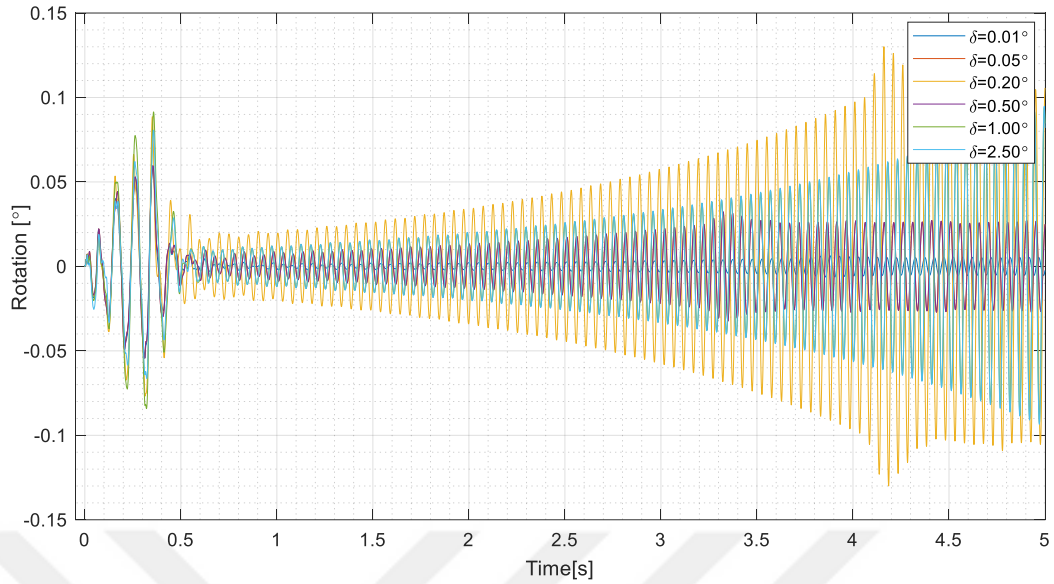

Figure 6.33 Elevator Rotation about the Hinge Axis at 162.00 m/s for Different Different Aileron and Elevator Freeplay Angles

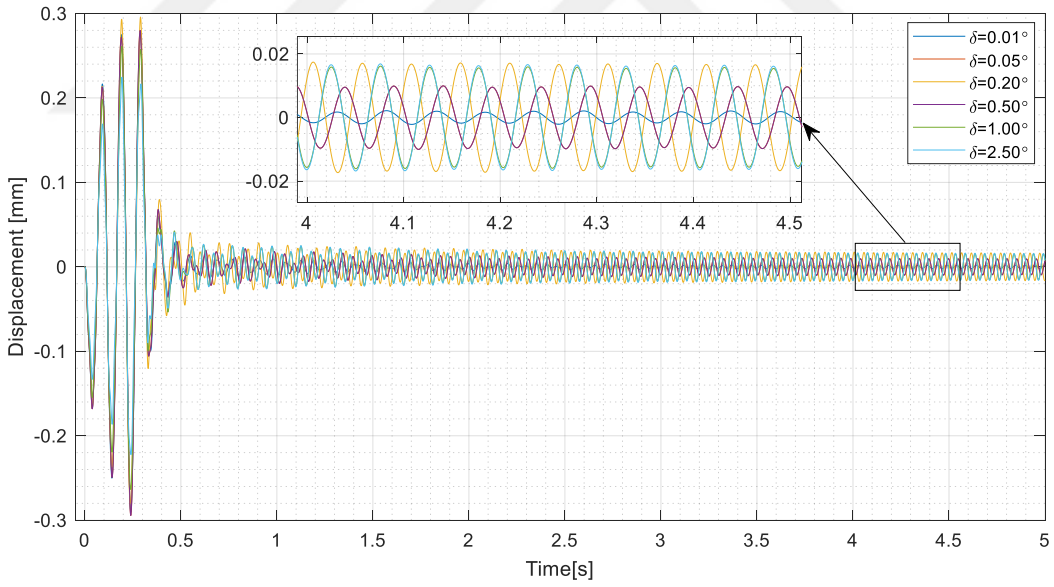

Figure 6.34 Center of Gravity Displacement at 159.00 m/s in x-direction for Different Aileron and Elevator Freeplay Angles

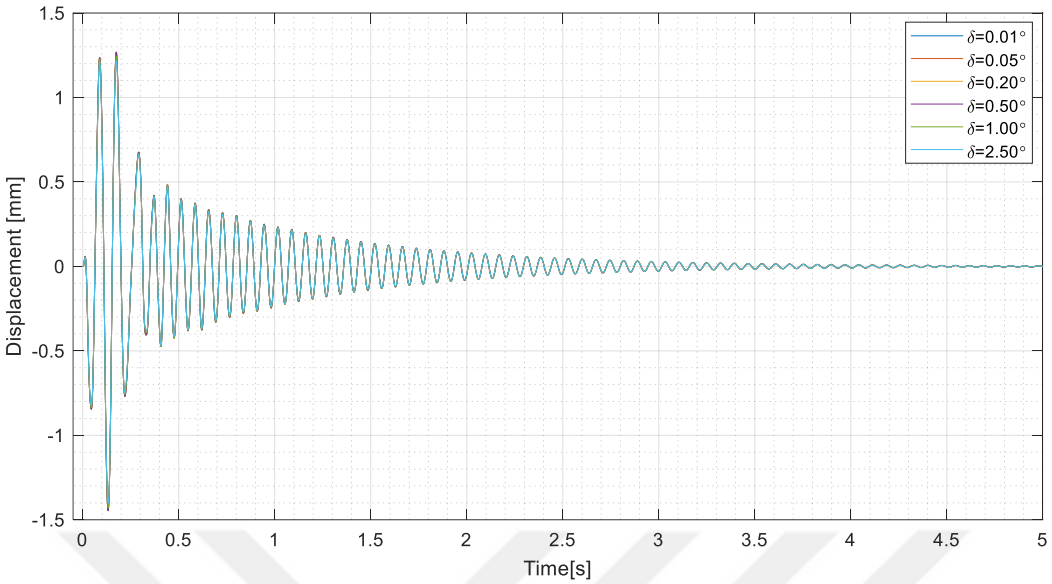

Figure 6.35 Center of Gravity Displacement at 159.00 m/s in y-direction for Different Aileron and Elevator Freeplay Angles

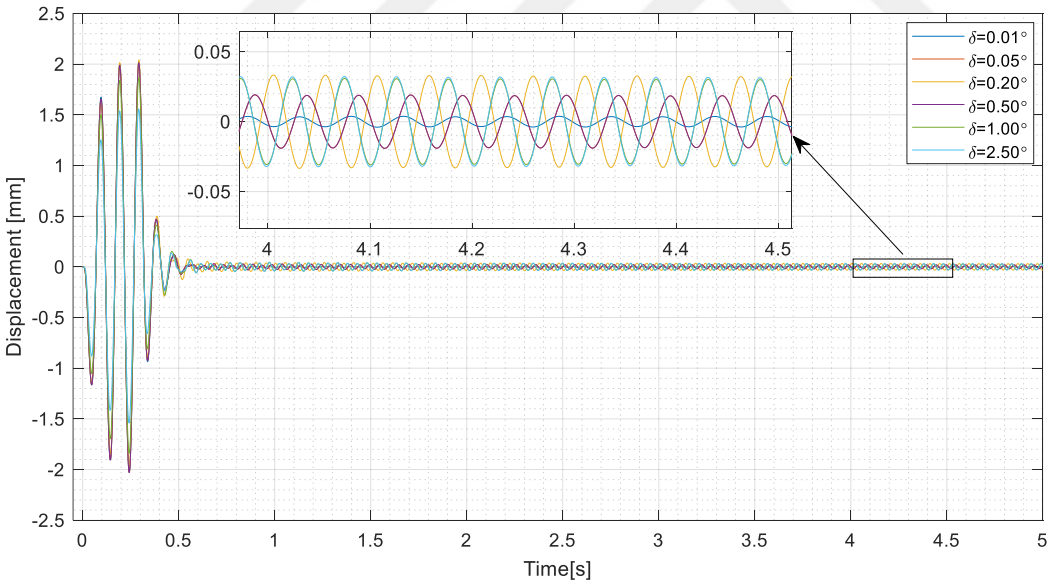

Figure 6.36 Center of Gravity Displacement at 159.00 m/s in z-direction for Different Aileron and Elevator Freeplay Angles

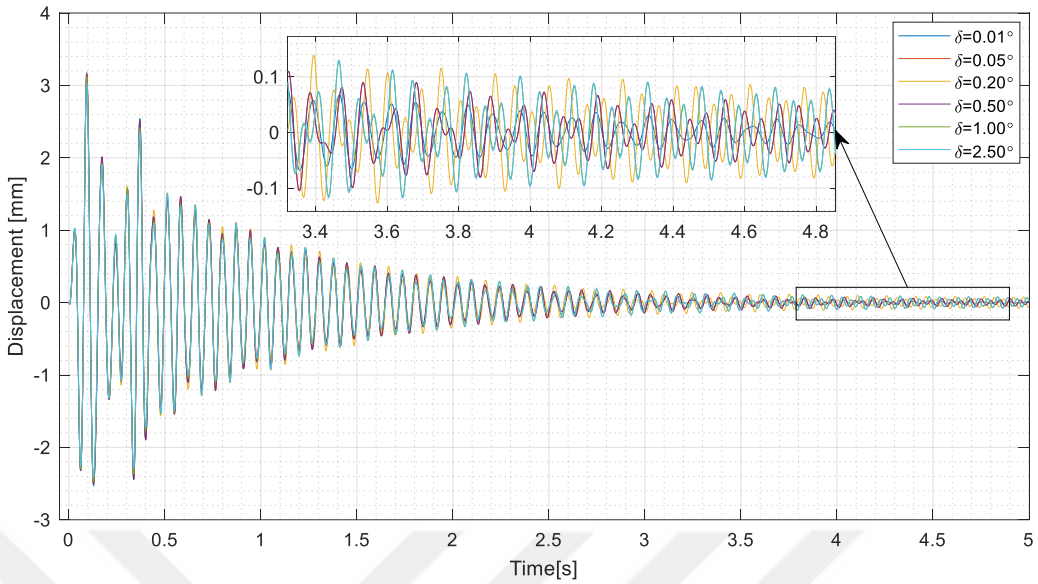

Figure 6.37 Right Wing tip Displacement at 159.00 m/s in the x-direction for Different Aileron and Elevator Freeplay Angles

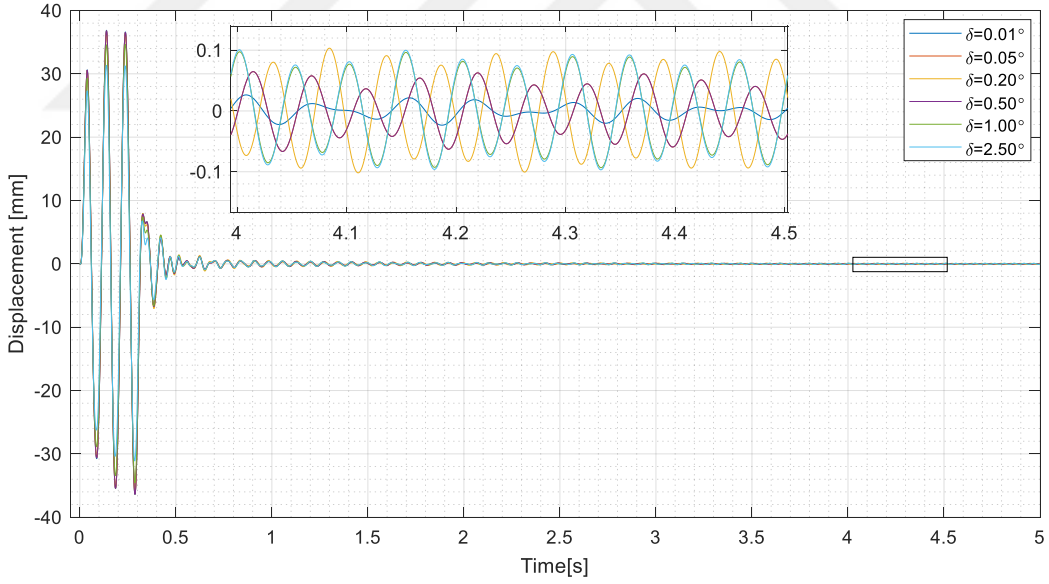

Figure 6.38 Right Wing tip Displacement at 159.00 m/s in the z-direction for Different Aileron and Elevator Freeplay Angles

As it can be inferred from the results, for the elevator freeplay case only, the velocity of LCO is 245 m/s. On the other hand, the velocity of LCO is 159 m/s for the right

aileron and elevator freeplay case. Although the responses are smaller in right aileron and elevator freeplay case, LCO behaviour is clearly seen and compared to the only elevator freeplay case, the velocity of LCO decreased significantly. It should be noted that in the simultaneous aileron-elevator freeplay case, freeplay exists only in the right aileron, not in both left and right aileron. ZAERO has a capability of handling at most 9 freeplay regions, or nonlinear regions in general, therefore both left and right aileron freeplay together with elevator freeplay could not be analyzed. The only way to perform this analysis could be to extract all system matrices outside ZAERO and perform nonlinear aeroelastic analysis outside the ZAERO environment. This could be possible future study.

6.8 Conclusion

In this chapter, studies performed on the nonlinear aeroservoelastic modelling and analysis are presented. Firstly, details of the actuator dynamic model and plant level aeroelastic equations are presented. The aircraft studied in this thesis is not a fly-by-wire (FBW) aircraft; hence the actuators are artificial and in this study interference of the actuator dynamics with the aeroelastic system is not considered and actuator is represented by a dummy transfer function.

Followingly, in order to construct the aeroservoelastic or the vehicle model of the aircraft, flight control law algorithm is incorporated into the aeroelastic model. Since the aircraft does not have any FCC and flight control law, and aircraft rigid body derivatives are required, trim analysis is conducted on rigid body aircraft and stability derivatives are obtained. Then, a simple flight control algorithm is generated by the pole placement method and simulation of the closed-loop system with the aeroelastic plant model is performed and results are presented.

To reflect nonlinearity, which is caused by control surface freeplay, freeplay implementation by adding the offset moments is explained. Later, to approximate the nonlinearity better in the structural dynamic model, fictitious mass approach is

presented. Governing equations of the nonlinear aeroservoelastic model including freeplay nonlinearity and fictitious mass approach are given.

Finally, nonlinear aeroservoelastic analysis is performed for each control surfaces, i.e., ailerons, elevator, rudder and the combination of aileron and elevator, with different freeplay angles at different flight conditions for sinusoidal disturbances of control surfaces. As a result of aeroservoelastic analyses, control surface rotations and the displacements of the center of gravity, wing tip and control surfaces are presented and LCO velocities are determined. It is seen that for the particular aircraft studied, only the elevator and the combination of the aileron/elevator freeplay caused a limit cycle oscillation and rudder freeplay cause a mild LCO of the rudder for all freeplay angles. The freeplay on the aileron caused LCO behaviour for only 1.00° and 2.50° freeplay angles. It is also observed that, when the elevator freeplay has LCO at 245 m/s, simultaneous right aileron and elevator freeplay case resulted in a LCO velocity at 159 m/s. This is a significant reduction in LCO velocity. Simultaneous freeplay in control surfaces must be studied at the aircraft level to evaluate the effect of freeplay on the nonlinear aeroelastic behaviour of aircraft.

CHAPTER 7

CONCLUSION

7.1 General Conclusion

The aim of this study is to introduce modelling and analysis of nonlinear aeroservoelastic model of the aircraft due to freeplay motion of the control surfaces and examining the nonlinear dynamic behavior of the aircraft. Based on the structural dynamics and aerodynamic models of a full-span very light aircraft, aeroelastic model is constructed using the spline methodology. Artificial actuators and flight control algorithm is included into the aeroelastic model and aeroservoelastic model obtained. Implementing freeplay motion of control surfaces into the aeroservoelastic model by the fictitious mass approach, nonlinear aeroservoelastic model is obtained and analyzed. The results of this analysis are presented for different control surface freeplay angles.

First part of the study is on the structural modelling of the aircraft. GFEM of the aircraft which is generated in MSC.Patran® environment is introduced. In order to cover linear and nonlinear dynamic behavior of the aircraft, modal analysis is conducted via MSC.Nastran® and structural mode shapes and frequencies are obtained. Frequency domain results are used to represent the flexibility of the aircraft in aeroelastic and aeroservoelastic analysis later on.

In the second part of the study, aerodynamic model of the aircraft is introduced. Utilizing the CFD model of the aircraft, high fidelity aeroelastic aerodynamic model is generated. Using this model, AIC matrices are calculated and stored in frequency domain via ZONA6 which is submodule of ZAERO. In order to use the calculated AIC matrices in aeroservoelastic analysis, they have to be transformed into time domain in state-space form using the Rational Function Approximation method

which is available in ZAERO. As for the rational function approximation, two different least square fit methods, Roger's and Minimum State, are offered. By comparing the approximation results of the two methods with the frequency domain result, it is seen that Roger's method showed better approximation; hence in the rest of the analysis this method is used.

In the third part of the thesis study, structural and aerodynamic models are integrated with the spline methodology and aeroelastic model of the aircraft is created. By selecting structural grids and pairing them with related aerodynamic elements, ZAERO constructs spline matrices which allows to bring about an interaction between the aerodynamic and structural models. Moreover, for the verification of the spline methodology, structural mode shapes of the FE model of the aircraft and projected mode shapes on the aerodynamic model are compared. The results show that spline grids are well-chosen and coupling of the structural and the aerodynamic model is satisfactory. To examine the flutter instability of the aircraft using the generated aeroelastic model, flutter analysis is conducted. Two solution methods, K and P-K methods are presented. Since the P-K solution algorithm gives matched point solution in flutter analysis, it is chosen and used in rest of the analysis. The flutter analysis of the open-loop aeroelastic model, without any control model, shows that aircraft is free from flutter instability within the flight regime. However, mode shape of elevator bending at 163.590 m/s which corresponds to 0.470 Mach number at the sea level has positive damping which is an indication of flutter instability. Since flutter speed is beyond the aircraft capabilities and regulation limitations, it is concluded that aircraft is free from flutter.

Last chapter is dedicated to nonlinear aeroservoelastic modelling and analysis. Firstly, dynamic behavior of control surface actuators is represented by a transfer function in Laplace domain. On the other hand, since there is no actuator in the aircraft in real life, the effect of phase and lags characteristic of actuators on the aeroelastic and aeroservoelastic analysis is not considered. Although it is out of the scope of thesis, aeroservoelastic analysis requires a flight control algorithm.

Therefore, trim analysis is conducted utilizing the aeroelastic model of the aircraft and rigid body derivatives of the aircraft with respect to control surface deflections and rates in three degrees of freedom are calculated in ZAERO. The equations of rigid body motion of the aircraft are expressed in state-space domain and a simple flight control algorithm is generated by the pole placement method utilizing rigid body aircraft matrices which are based on the stability derivatives of the aircraft obtained previously. Combining the control surface actuator dynamic behavior and the flight control algorithm with the aeroelastic system, linear aeroservoelastic system is constructed and their governing equations are presented. Followingly, freeplay implementation is shared. Modification on off-set moments is utilized to represent the freeplay accurately and provide continuity during the transition of the freeplay regions. Then, fictitious mass approach is introduced and implement in the nonlinear aeroelastic analysis. Nonlinear dynamic behavior of the aircraft due to freeplay is represented in a more convenient way by the fictitious mass approach than the direct method approach regarding the mode shapes and frequencies. Finally, the aeroservoelastic model of the aircraft is created utilizing offset moment correction to include the restoring forces due to freeplay motion into the system of equations and the fictitious mass approach. Related governing equations are presented and time marching nonlinear aeroservoelastic analyses due to different control surface freeplays are conducted and nonlinear responses of the aircraft are presented separately for each control surface freeplay and also for the combination of elevator and aileron freeplays. It should be noted that time marching nonlinear analysis is performed for different flight conditions and characteristics of the effect of freeplay in different control surfaces on the aircraft response are different from each other. The results of time domain analyses showed that limit cycle oscillation occurred only related with the elevator freeplay and combined aileron/elevator freeplay motions for all freeplay angles in the study. For the aileron case, limit cycle oscillation behaviour is captured only for a few freeplay angles. High amplitude rudder freeplay has relatively very small amplitude LCO, which can be ignored since their motions damped out directly. When the velocity of analysis is increased to

cover bigger oscillations, attitude of the aircraft has a tendency to diverge due to rigid body modes. It should be emphasized that simultaneous right aileron and elevator freeplay case resulted in a significant reduction in the LCO velocity compared to the only elevator freeplay case. This study shows that simultaneous freeplay in multiple control surfaces has a significant effect on the nonlinear aeroelastic characteristics of aircraft. Such effects can only be discovered if the nonlinear aeroelastic analyses are performed at the aircraft level.

7.2 Recommendations for Future Work

During structural dynamic representation in aeroelastic and aeroservoelastic analysis, reduced order models can be used such as static and dynamic condensation on stiffness and mass matrices in order to decrease computational time of all analysis.

In this study, rigid body aircraft stability derivatives are obtained via trim analysis performed in ZAERO, and the parameters are limited according to the capabilities of ZAERO. Normally, by using available CFD database or wind tunnel results of the aircraft in the flight regime, full-state feedback theory can be utilized. However, ZAERO is an aeroelastic design and analysis program and all of aircraft stability derivatives could not be obtained. Therefore, full-state feedback theory could not be used in this study; because states are limited to the rates in 3 degrees of freedom which are p, q and r. Using CFD analysis and database, the coefficients and rigid body derivatives of the aircraft can be obtained more accurately and in full state.

Instead of pole placement method during the flight control law algorithm design, Linear Quadratic Regulator (LQR), μ -analysis and synthesis or H_2 -synthesis can be utilized. It should be also noted that, the open-loop poles of the aircraft are negative, and they are doubled and used as closed-loop poles. When the damping of the open-loop system is increased by feedback gain, it is observed that nonlinear LCO behaviour of the aircraft shifts to higher velocities and it can be investigated as a

future study. Moreover, a state observer can be modelled in order to increase the flight control algorithm to full-state feedback.

Finally, simultaneous freeplay in multiple control surfaces can be studied at aircraft level to ascertain the effect of critical freeplay combinations on the LCO velocity.

REFERENCES

[1] R. L. Bisplinghoff, H. Ashley, and R. L. Halfman, *Principles of Aeroelasticity*, 2nd ed. New York: Dover Publications, Inc., 1975.

[2] Z. Wan, B. Zhang, Z. Du, and C. Yang, "Aeroelastic two-level optimization for preliminary design of wing structures considering robust constraints," *Chinese Journal of Aeronautics*, vol. 27, no. 2, pp. 259–265, 2014, doi: 10.1016/j.cja.2014.02.018.

[3] W. Tian *et al.*, "Nonlinear aeroservoelastic analysis of a supersonic aircraft with control fin free-play by component mode synthesis technique," *J Sound Vib*, vol. 493, Feb. 2021, doi: 10.1016/j.jsv.2020.115835.

[4] A. Tewari, *Aeroservoelasticity: Modeling and control*. Springer, 2015. [Online]. Available: http://www.springer.com/series/4988

[5] I. Abel, "Technique for Predicting the Characteristics of a Flexible Wing Equipped With an Active Flutter-Suppression System and Comparison With Wind-Tunnel Data," 1979.

[6] I. Abel, B. Perry, and H. N. Murrow, "Two synthesis techniques applied to flutter suppression on a flight research wing," *Journal of Guidance, Control, and Dynamics*, vol. 1, no. 5, pp. 340–346, 1978, doi: 10.2514/3.55790.

[7] H. J. Dunn, "An Analytical Technique for Approximating Unsteady Aerodynamics in the Time Domain," NASA Technical Paper 1738, 1980.

[8] M. Karpel, "Design for Active and Passive Flutter Suppression and Gust Alleviation," *NASA CR-3482*, 1981.

[9] T. Theodorsen, "General Theory of Aerodynamic Instability and the Mechanism of Flutter," Langley Field. VA, United States, 1949.

[10] J. W. Edwards and J. B. Malone, “Current Status of Computational Methods for Transonic Unsteady Aerodynamics and Aeroelastic Application,” *Computing Systems in Engineering*, vol. 3, no. 5, pp. 545–569, 1992.

[11] D. E. Raveh, “CFD-based models of aerodynamic gust response,” *J Aircr*, vol. 44, no. 3, pp. 888–897, 2007, doi: 10.2514/1.25498.

[12] H. Tijdeman, “Investigations of the transonic flow around oscillating airfoils,” 1977.

[13] J. M. Maciejowski, *Multivariable Feedback Design*. Addison-Wesley, 1989. doi: 10.1017/S0263574700007761.

[14] K. Glover and J. C. Doyle, “State-space formulae for all stabilizing controllers that satisfy an Hoo-norm bound and relations to risk sensitivity,” 1988.

[15] J. C. Doyle, “Structure Uncertanity in Control System Design,” 1985.

[16] M. Karpel and M. Newman, *Accelerated convergence for vibration modes using the substructure coupling method and fictitious coupling masses*. University of Tel-Aviv, 1975.

[17] M. Karpel and C. D. Wieseman, “Modal coordinates for aeroelastic analysis with large local structural variations,” *J Aircr*, vol. 31, no. 2, pp. 396–403, 1994, doi: 10.2514/3.46499.

[18] M. Karpel and D. Raveh, “Fictitious mass element in structural dynamics,” *AIAA Journal*, vol. 34, no. 3, pp. 607–613, 1996, doi: 10.2514/3.13111.

[19] M. Karpel and C. D. Wieseman, “Time simulation of flutter with large stiffness changes,” *J Aircr*, vol. 31, no. 2, pp. 404–410, 1994, doi: 10.2514/3.46500.

[20] G. Dimitriadis, *Introduction to Nonlinear Aeroelasticity*. Wiley, 2017.

[21] D. A. Pereira, R. M. G. Vasconcellos, M. R. Hajj, and F. D. Marques, “Effects of combined hardening and free-play nonlinearities on the response of a typical aeroelastic section,” *Aerosp Sci Technol*, vol. 50, pp. 44–54, Mar. 2016, doi: 10.1016/j.ast.2015.12.022.

[22] W. D. Anderson and S. Mortara, “Maximum Control Surface Freeplay, Design and Flight Testing Approach on the F-22,” 2007.

[23] R. Vasconcellos, A. Abdelkefi, F. D. Marques, and M. R. Hajj, “Representation and analysis of control surface freeplay nonlinearity,” *J Fluids Struct*, vol. 31, pp. 79–91, May 2012, doi: 10.1016/j.jfluidstructs.2012.02.003.

[24] B. Danowsky, P. M. Thompson, and S. Kukreja, “Nonlinear analysis of aeroservoelastic models with free play using describing functions,” in *Journal of Aircraft*, 2013, vol. 50, no. 2, pp. 329–336. doi: 10.2514/1.C031370.

[25] S. He, Z. Yang, and Y. Gu, “Limit cycle oscillation behavior of transonic control surface buzz considering free-play nonlinearity,” *J Fluids Struct*, vol. 61, pp. 431–449, Feb. 2016, doi: 10.1016/j.jfluidstructs.2015.11.014.

[26] J. Panchal and H. Benaroya, “Review of control surface freeplay,” *Progress in Aerospace Sciences*, vol. 127. Elsevier Ltd, Nov. 01, 2021. doi: 10.1016/j.paerosci.2021.100729.

[27] N. R. Hoffman and I. N. Spielberg, “Subsonic Flutter Tests of an Unswept All-Movable Horizontal Tail,” 1954.

[28] D. S. Woolston, H. L. Runyan, and T. A. Byrdsong, “Some Effects of System Nonlinearities in the Problem of Aircraft Flutter,” 1955.

[29] S. F. Shen, “An Approximate Analysis of Nonlinear Flutter Problems,” *Journal of the Aerospace Sciences*, vol. 26, no. 1, pp. 25–32, Jan. 1959, doi: 10.2514/8.7914.

[30] B. H. K. Lee, S. J. Price, and Y. S. Wong, “Nonlinear aeroelastic analysis of airfoils: bifurcation and chaos,” 1999.

[31] P. Gold, M. Karpel, and M. Idan, “Modeling and control of nonlinear aeroservoelasticity due to actuator free play,” in *47th Israel Annual Conference on Aerospace Sciences 2007*, 2007.

[32] R. Huang, H. Hu, and Y. Zhao, “Nonlinear aeroservoelastic analysis of a controlled multiple-actuated-wing model with free-play,” *J Fluids Struct*, vol. 42, pp. 245–269, Oct. 2013, doi: 10.1016/j.jfluidstructs.2013.06.007.

[33] M. Karpel, A. Shousterman, C. Maderuelo, and H. Climent, “Dynamic aeroservoelastic response with nonlinear structural elements,” in *AIAA Journal*, 2015, vol. 52, no. 11, pp. 3233–3239. doi: 10.2514/1.J053550.

[34] F. Roizner and M. Karpel, “Aeroservoelastic Stability Analysis Using Response-Based Parametric Flutter Margins,” *International Forum on Aeroelasticity and Structural Dynamics IFASD*, 2017.

[35] F. Roizner and M. Karpel, “Parametric flutter margin method for aeroservoelastic stability analysis,” *AIAA Journal*, vol. 56, no. 3, pp. 1011–1022, 2018, doi: 10.2514/1.J056514.

[36] U. Yurtsever, M. Şahin, and A. Kayran, “Nonlinear Aeroservoelastic Modelling and Analysis of an Aircraft having Control Surfaces with Freeplay,” *Fırat Üniversitesi Uzay ve Savunma Teknolojileri Dergisi* , vol. 1, no. 1, pp. 201–207, 2022 (*Boşta Hareket Davranışı İçeren Kontrol Yüzeylerine Sahip Bir Uçağın Doğrusal Olmayan Aeroservoelastik Modellenmesi ve Analizi*).

[37] MSC. Software, “MSC Nastran 2022.1 - Reference Guide,” 2022.

[38] J. Wright, “Flutter,” *Encyclopedia of Vibration*, pp. 553–565, 2001, doi: 10.1006/RWVB.2001.0126.

[39] L. Morino and K. Tseng, “Time-Domain Green’s Function Method for Three-Dimensional Nonlinear Subsonic Flows,” 1978.

[40] M. Karpel, B. Moulin, and P. C. Chen, “Dynamic Response of Aeroservoelastic Systems to Gust Excitation,” *J Aircr*, vol. 42, no. 5, pp. 1264–1272, Sep. 2005, doi: 10.2514/1.6678.

[41] M. M. Iovnovich, “Effect Of External Stores Aerodynamics on Analytic Fighter Aircraft Flutter Predictions: Evaluation of a Superposition Modeling Approach,” 2019.

[42] C. Pak, “Aeroelastic Tailoring Study of an N+2 Low-boom Supersonic Commercial Transport Aircraft,” in *16th AIAA/ISSMO Multidisciplinary Analysis and Optimization Conference*, Jun. 2015. doi: 10.2514/6.2015-2791.

[43] J. T. Batina, “Advanced Small Perturbation Potential Flow Theory for unsteady aerodynamic and aeroelastic analyses - NASA technical reports server (NTRS),” *NASA*, 2005. https://ntrs.nasa.gov/citations/20050245109 (accessed Sep. 29, 2022).

[44] L. Katzenmeier, C. Breitsamter, C. Vidy, and M. Winter, “Verification of the Use of Small-Disturbance CFD in Flutter and Gust Analyses for Simple to Highly Complex Configurations,” 2015. [Online]. Available: https://www.researchgate.net/publication/291312307

[45] ZONA Tech., “ZAERO Theoretical Manual V. 9.3,” 2017.

[46] V. J. E. Stark, “General equations of motion for an elastic wing and method of solution,” *AIAA Journal*, vol. 22, no. 8, pp. 1146–1153, 1984, doi: 10.2514/3.8750.

[47] H. J. Hassig, “An Approximate True Damping Solution of the Flutter Equation by Determinant Iteration,” *J Aircr*, vol. 8, no. 11, 1971.

[48] F. A. Administration, “Aeroelastic stability substantiation of transport category Airplanes (AC 25.629-1B),” 2014.

[49] D. Rowell, “2 . 14 Analysis and Design of Feedback Control Systems State-Space Representation of LTI Systems.,” 2002. http://web.mit.edu/2.14/www/Handouts/StateSpace.pdf

[50] M. R. Napolitano, *Aircraft Dynamics: From modeling to simulation*. John Wiley & Sons, Inc., 2012.

[51] M. v. Cook, *Flight dynamics principles: a linear systems approach to aircraft stability and control*. Butterworth-Heinemann, 2013.

[52] H. Dai, X. Yue, J. Yuan, D. Xie, and S. N. Atluri, “A comparison of classical Runge-Kutta and Henon’s methods for capturing chaos and chaotic transients in an aeroelastic system with freeplay nonlinearity,” *Nonlinear Dyn*, vol. 81, no. 1–2, pp. 169–188, Jul. 2015, doi: 10.1007/s11071-015-1980-x.

[53] E. Verstraelen, G. Dimitriadis, G. D. ben Rossetto, and E. H. Dowell, “Two-domain and three-domain limit cycles in a typical aeroelastic system with freeplay in pitch,” *J Fluids Struct*, vol. 69, pp. 89–107, Feb. 2017, doi: 10.1016/j.jfluidstructs.2016.11.019.

[54] M. A. Padmanabhan, “Sliding Wear and Freeplay Growth Due to Control Surface Limit Cycle Oscillations,” *J Aircr*, vol. 56, no. 5, pp. 1973–1979, 2019, doi: 10.2514/1.C035438.

[55] L. Morino, “A General Theory of Unsteady Compressible Potential Aerodynamics,” *NASA CR-2464*, 1974.

APPENDICES

A. Mode Shapes of the Very Light Aircraft

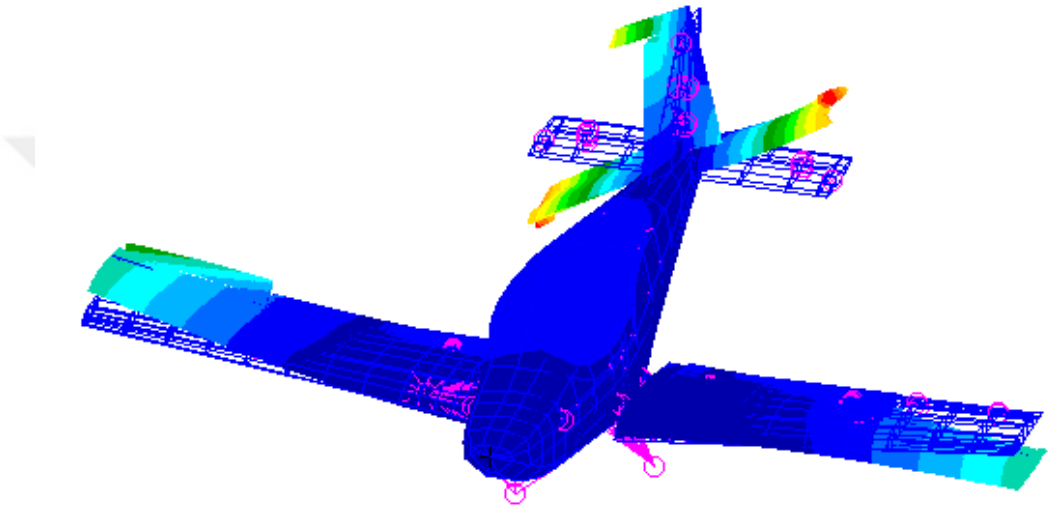

Figure A.1 Antisymmetric Wing Bending + Fuselage Torsion Mode Shape at 18.568 Hz

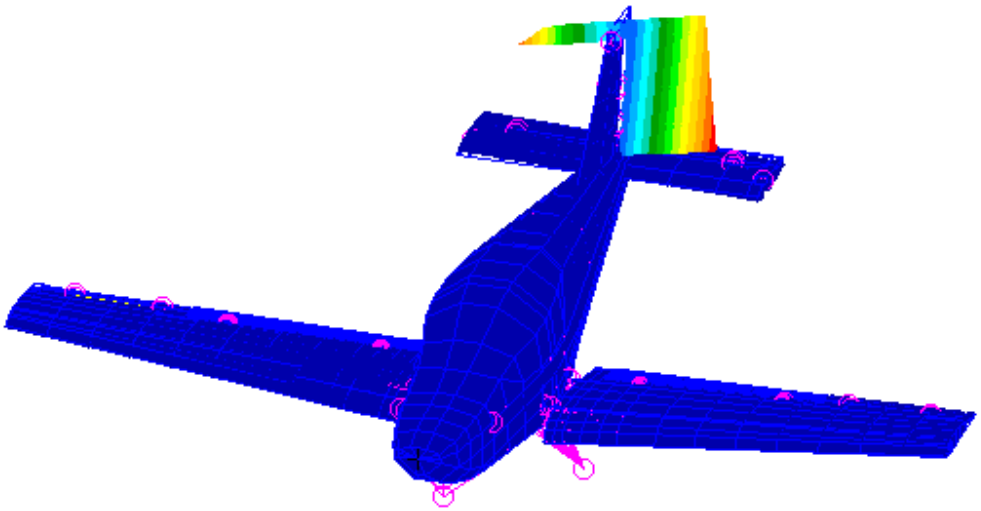

Figure A.2 Rudder Rotation Mode Shape at 19.476 Hz

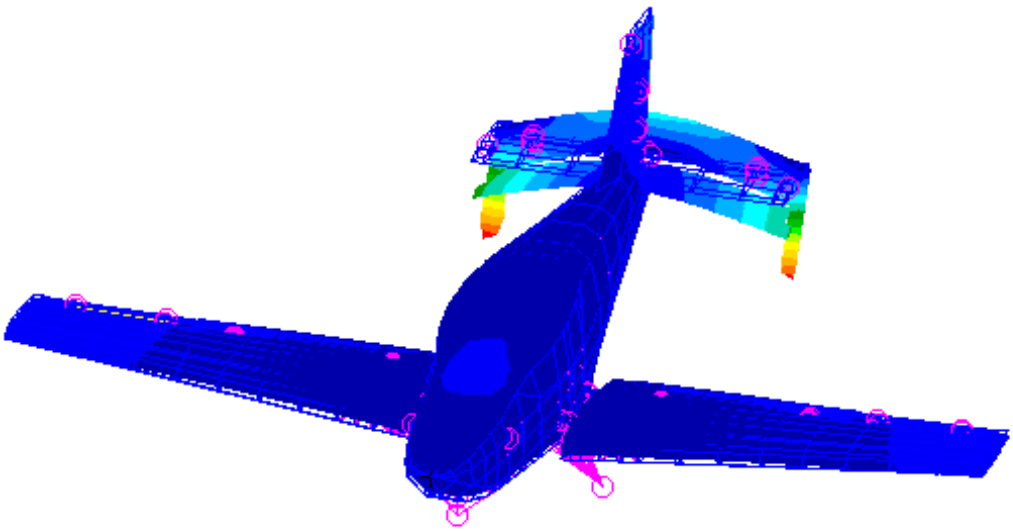

Figure A.3 Horizontal Tail Bending + Elevator Rotation Mode Shape at 20.392 Hz

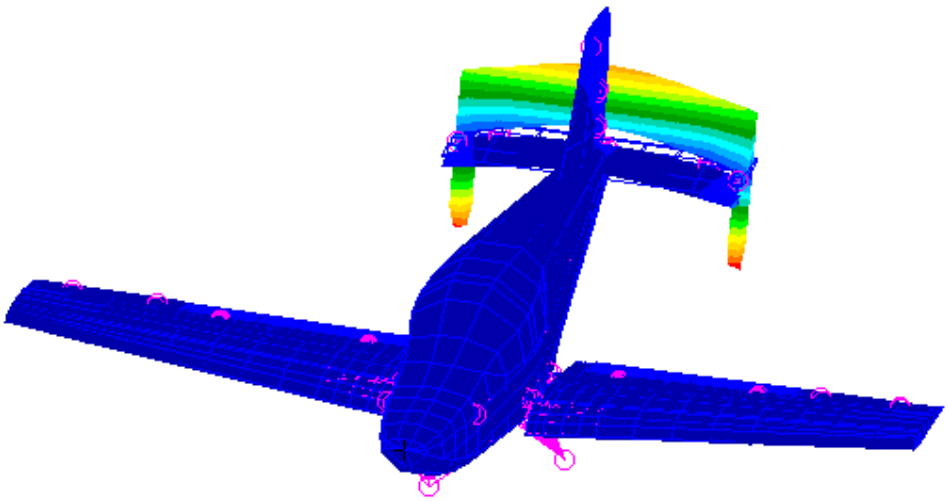

Figure A.4 Elevator Rotation Mode Shape at 22.083 Hz

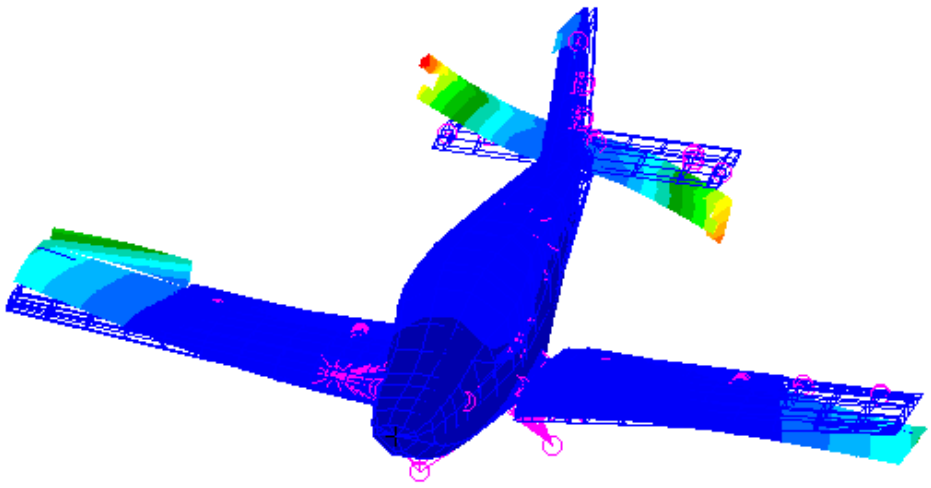

Figure A.5 Wing 2nd Bending + Horizontal Tail Rotation Mode Shape at 23.225 Hz

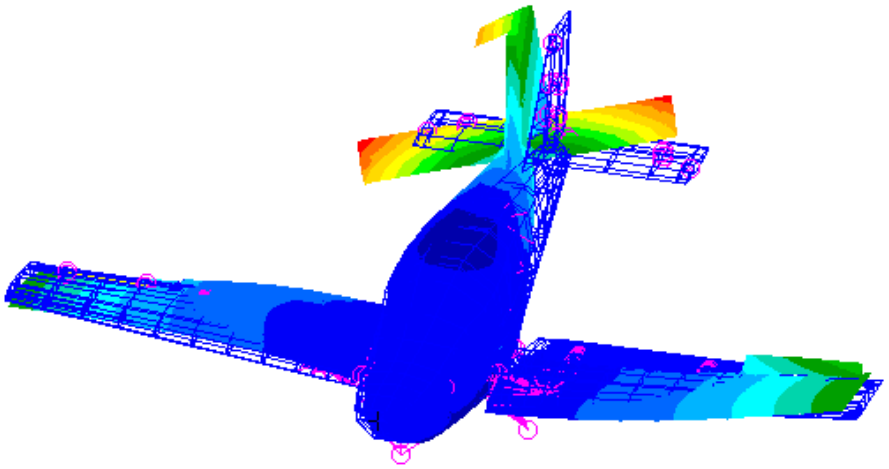

Figure A.6 Wing 2nd Bending + Rear Fuselage Lateral Bending Mode Shape at 24.624 Hz

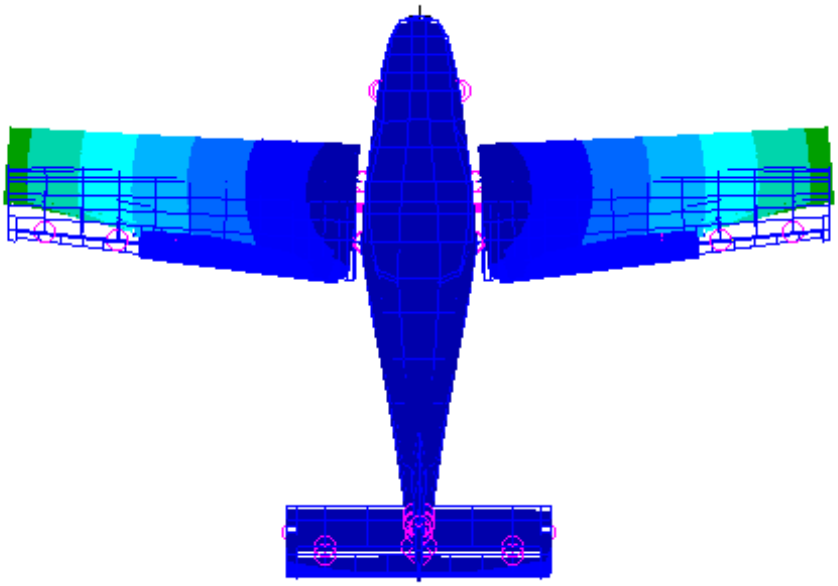

Figure A.7 Wing In-plane Bending Mode Shape at 24.988 Hz

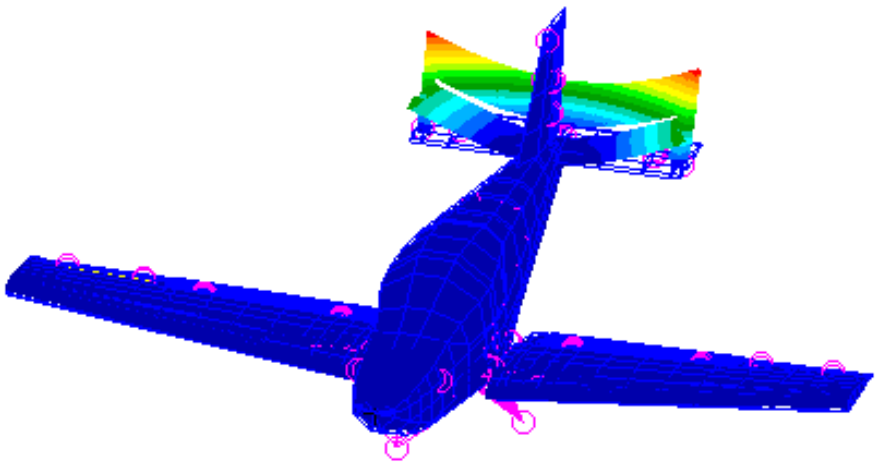

Figure A.8 Elevator Bending Mode Shape at 30.414 Hz

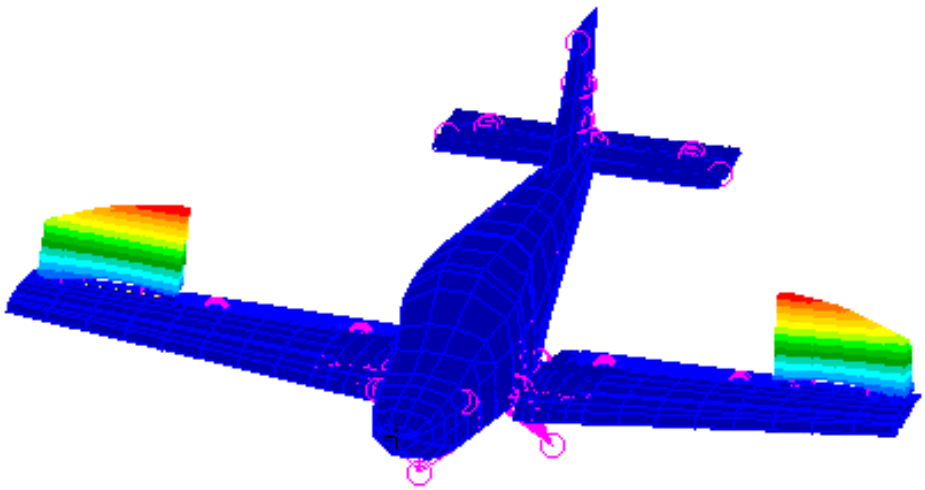

Figure A.9 Aileron Symmetric Bending Mode Shape at 32.083 Hz

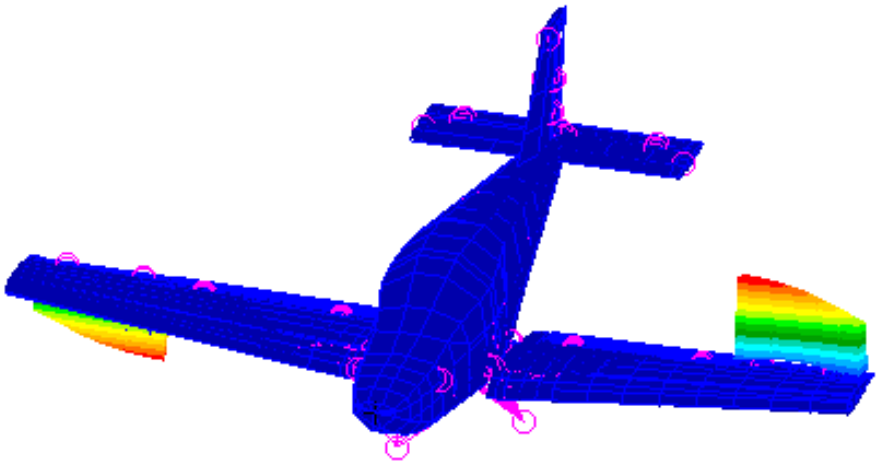

Figure A.10 Aileron Antisymmetric Bending Mode Shape at 32.120 Hz

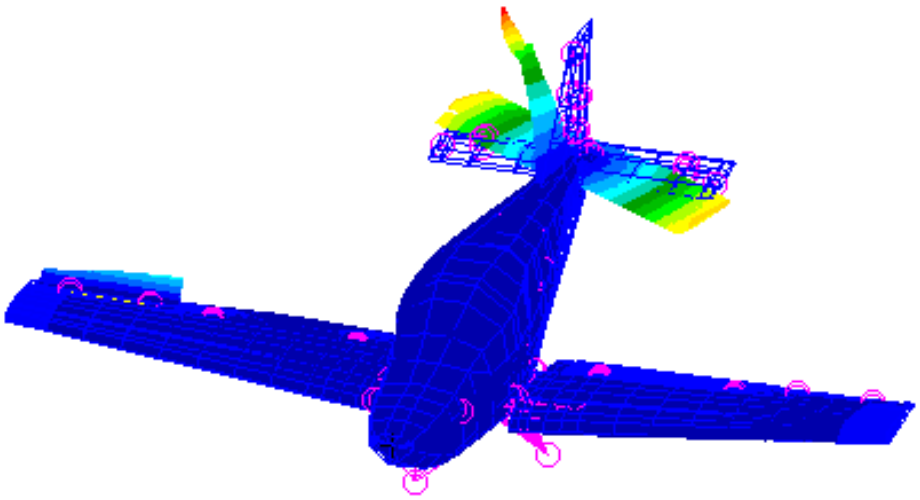

Figure A.11 Horizontal Tail In-plane Bending + Vertical Tail Bending Mode Shape at 33.173 Hz

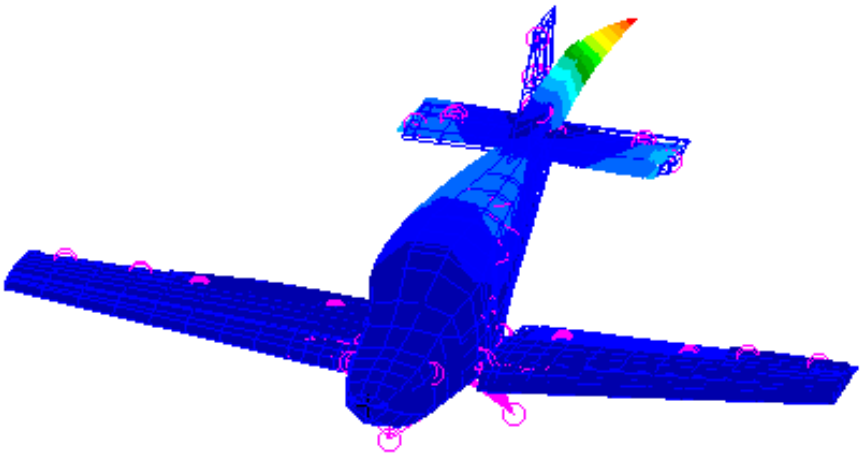

Figure A.12 Vertical Tail Bending Mode Shape at 35.974 Hz

B. Spline Verification

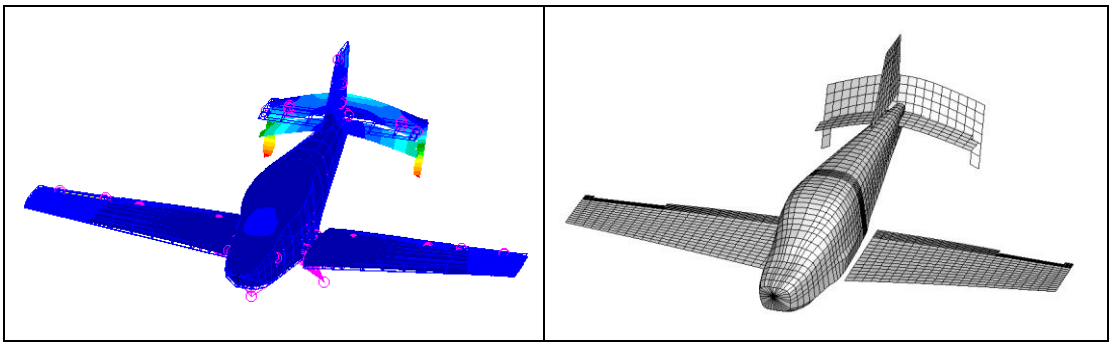

Figure B.1 Spline Verification of Horizontal Tail Bending + Elevator Rotation Mode Shape

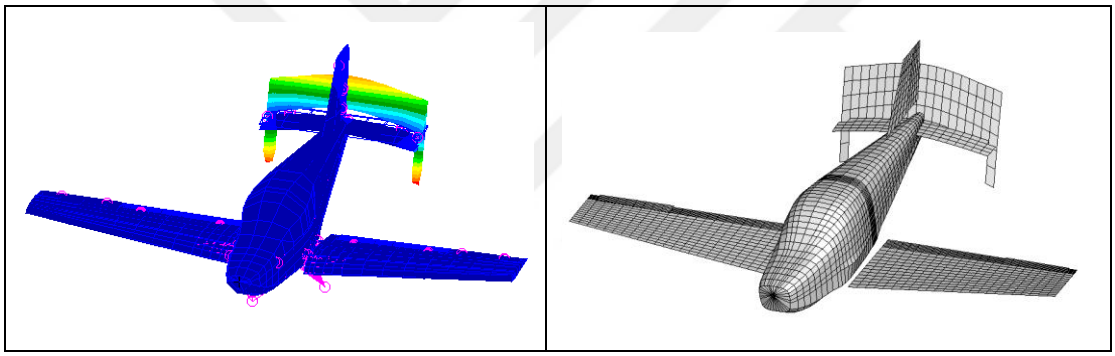

Figure B.2 Spline Verification of Elevator Rotation Mode Shape

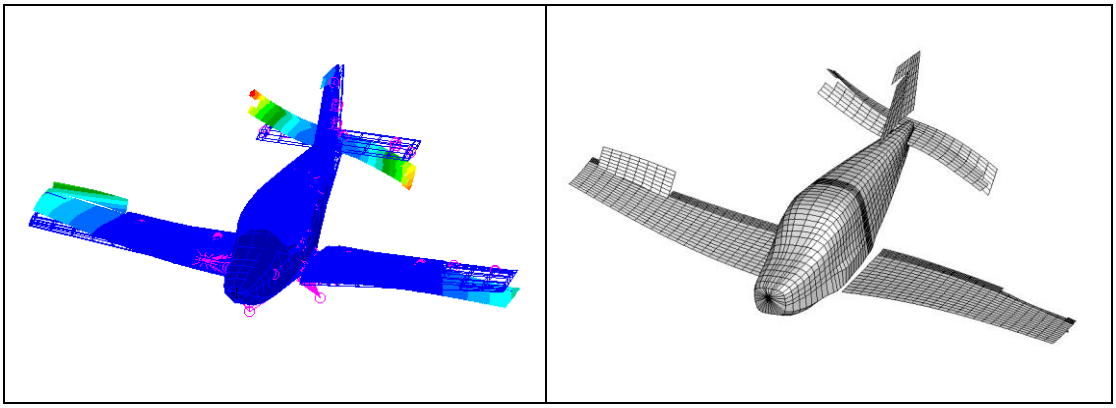

Figure B.3 Spline Verification of Wing 2nd Bending + Horizontal Tail Rotation Mode Shape

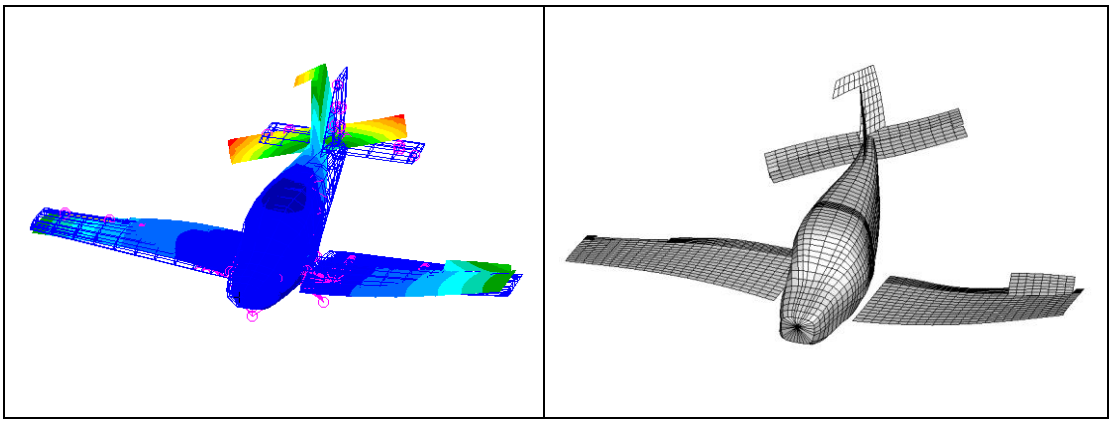

Figure B.4 Spline Verification of Wing 2nd Bending + Rear Fuselage Lateral Bending Mode Shape

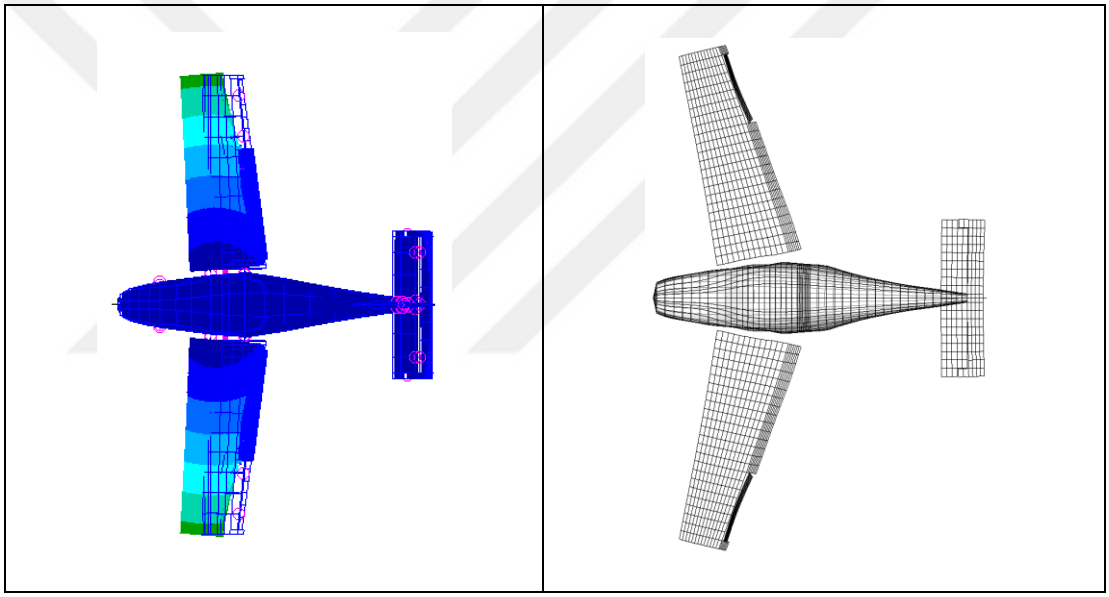

Figure B.5 Spline Verification of Wing In-plane Bending Mode Shape

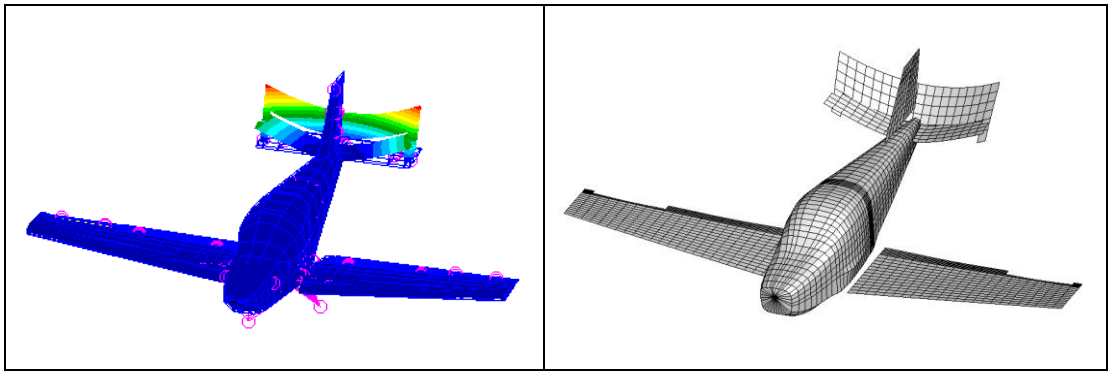

Figure B.6 Spline Verification of Elevator Bending Mode Shape

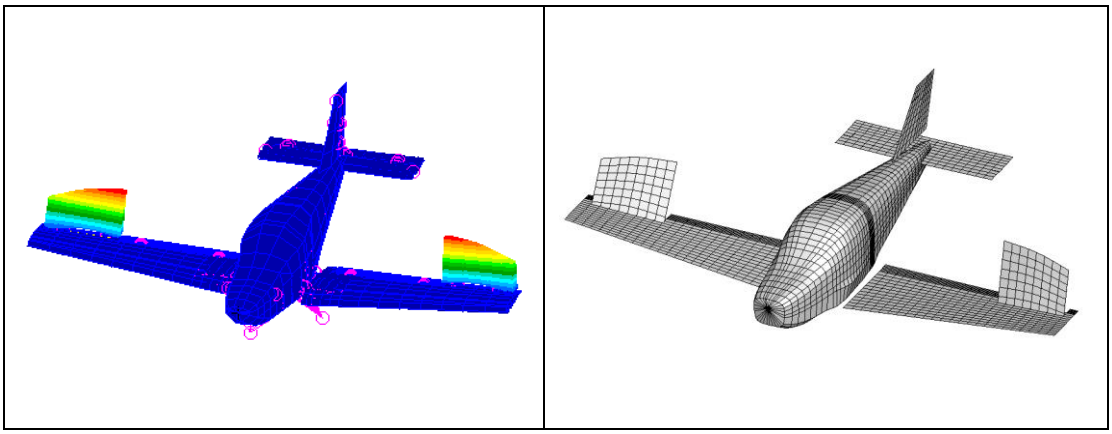

Figure B.7 Spline Verification of Aileron Symmetric Bending Mode Shape

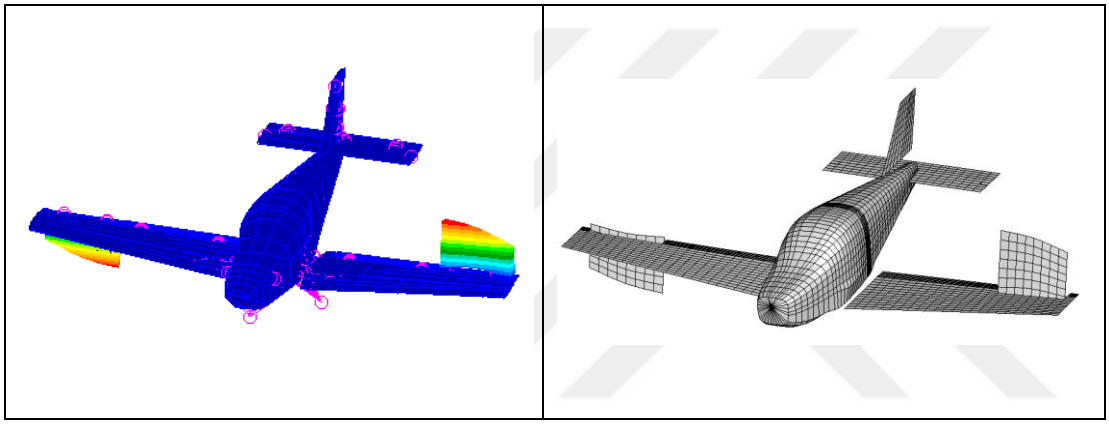

Figure B.8 Spline Verification of Aileron Antisymmetric Bending Mode Shape

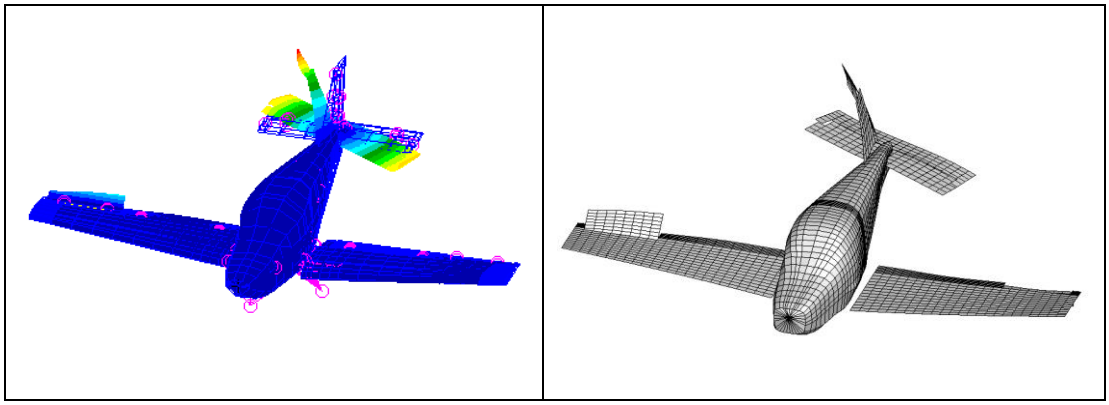

Figure B.9 Spline Verification of Horizontal Tail In-plane Bending + Vertical Tail Bending Mode Shape

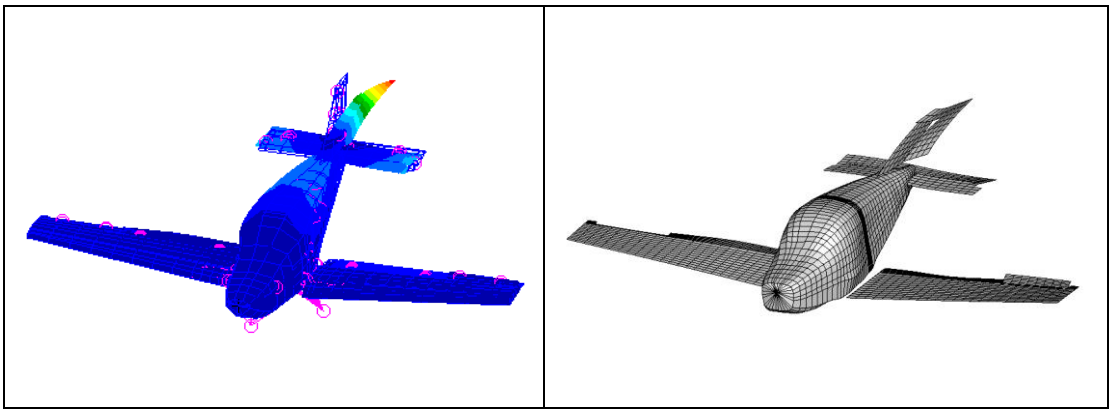

Figure B.10 Spline Verification of Vertical Tail Bending Mode Shape

C. Small Disturbance Equation Derivations

The Equation (4.1) can be divided into two parts [45]:

$$\Theta = \Theta_s + \Theta_u \qquad (C.1)$$

In Equation (C.1), steady and unsteady velocity potentials are represented by Θ_s and Θ_u respectively. According to steady and unsteady terms in Equation (C.1) respectively, Equation (4.1) can be expressed by Equations (C.2) and (C.3).

$$(1 - M^2{}_\infty)\Theta_{s_{xx}} + \Theta_{s_{yy}} + \Theta_{s_{zz}} = 0 \qquad (C.2)$$

$$(1 - M^2{}_\infty)\Theta_{u_{xx}} + \Theta_{u_{yy}} + \Theta_{u_{zz}} - 2\frac{M_\infty}{a_\infty}\Theta_{u_{xt}} - \frac{1}{a_\infty^2}\Theta_{u_{tt}} = 0 \qquad (C.3)$$

Equation (C.2) and Equation (C.3) are the steady and unsteady linearized small disturbance equations respectively. Assuming simple harmonic motion with oscillatory frequency (ω), the unsteady velocity potential can be expressed as:

$$\Theta_u = \bar{\Theta} e^{i\omega t} \qquad (C.4)$$

where reduced frequency-domain velocity potential is denoted with $\bar{\Theta}$. In order to simplify the equations, x, y and z terms can be expressed as:

$$\bar{x} = \frac{Lx}{\beta} \qquad (C.5)$$

$$\bar{y} = Ly \qquad (C.6)$$

$$\bar{z} = Lz \qquad (C.7)$$

where L is the reference length of the aeroelastic analysis, and it corresponds to the chord length and β is defined expressed as in Equation (C.8).

$$\beta = \sqrt{|1 - M^2{}_\infty|} \qquad (C.8)$$

Introducing modified velocity potential ($\widetilde{\Theta}$) and with the help of Equations (C.5-C.8), Equation (C.4) can be written in the following form:

$$\Theta_{\mathrm{u}} = \bar{\Theta} e^{i\omega t} = \widetilde{\Theta} e^{i\lambda M_{\infty} \bar{x}} \tag{C.9}$$

where reduced frequency (k) and compressible reduced frequency (λ) terms have the following definitions.

$$k = \frac{\omega L}{V} \tag{C.10}$$

$$\lambda = \frac{k M_{\infty}}{\beta} \tag{C.11}$$

In Equation (C.10), ω, L and V are the harmonic oscillatory frequency, reference chord length and velocity of the undisturbed flow. Then, Equation (C.3) can be re-expressed by defined parameters as in Equation (4.13).

$$\widetilde{\Theta}_{\bar{x}\bar{x}} + \mu \widetilde{\Theta}_{\bar{y}\bar{y}} + \mu \widetilde{\Theta}_{\bar{z}\bar{z}} + \lambda^2 \widetilde{\Theta} = 0 \tag{C.12}$$

The value of μ term in Equation (C.12) is 1 in subsonic region and -1 in supersonic region. Applying Green's theorem [55] to Equation (C.12), an integral solution is obtained in the following form:

$$\Theta_{\mathrm{u}} = \Theta_{\mathrm{W}}(x_0, y_0, z_0) + \Theta_{\mathrm{B}}(x_0, y_0, z_0) \tag{C.13}$$

$$\Theta_{\mathrm{w}}(x_0, y_0, z_0) = \frac{1}{E\pi} \iint_{w} \Delta\phi(x', y', z', t) e^{i\lambda M_{\infty} \xi} \frac{\partial}{\partial n} K dS \tag{C.14}$$

$$\Theta_{\mathrm{B}}(x_0, y_0, z_0) = -\frac{1}{E\pi} \iint_{B} \sigma(x', y', z', t) e^{i\lambda M_{\infty} \xi} K dS \tag{C.15}$$

In these equations, Θ_W and Θ_B are the velocity potential influence due to wing-like components and body-like components respectively. $\Delta\phi$ and σ refer to unsteady

doublet and source singularity distributions, respectively. K is the Kernel function and it is defined based on the flight regime as,

$$K = \frac{e^{i\lambda R}}{R} \qquad for\ subsonic\ region \tag{C.16}$$

$$K = \frac{\cos(\lambda R)}{R} \qquad for\ supersonic\ region \tag{C.17}$$

where R is defined as,

$$R = \sqrt{\xi^2 + \mu\eta^2 + \mu\zeta^2} \tag{C.18}$$

and,

$$\xi = \left(\frac{x' - x_0}{\beta L}\right),\ \eta = \left(\frac{y' - y_0}{L}\right),\ \zeta = \left(\frac{z' - z_0}{L}\right) \tag{C.19}$$

In Equation (C.19), x', y' and z' locations correspond to center of the sources and doublets in Equation (C.14) and (C.15) respectively. x_0, y_0 and z_0 locations are the field points to be calculated; E is equal to 2 or 4 in supersonic and subsonic flight regime, respectively. In Equation (C.14), $\frac{\partial}{\partial n}$ is the out-normal vector of the defined aerodynamic surface S, which is expressed as,

$$S = S(x, y, z, t) \tag{C.20}$$

where x, y, z are the points of the aerodynamic surface and t is time. The integral solutions of the problem over the surface S which are given in Equation (C.14) and (C.15) are defined in terms of the unsteady source and doublet singularity distributions. The source singularity distributions are used to calculate unsteady potential due to body-like components, whereas doublet singularity distributions are used to calculate unsteady wing-like components. Therefore, the integral boundary of the solution of the wing-like velocity potential equation (Θ_W) given in Equation (C.14) is corresponding to wing-like element surface and its wake effect through the

downstream whereas the integral boundary of the solution of the body-like velocity potential equation (Θ_B) given in Equation (C.15) is corresponding to body-like element surface. These integral equations are solved by the submodules of ZAERO, ZONA6 and ZONA7 in subsonic and supersonic regions respectively with necessary boundary conditions according to the aerodynamic model.

The unsteady velocity potential equation for wing-like elements is completely decoupled from steady velocity potential. On the other hand, unsteady velocity potential for body-like elements is coupled with the steady velocity potential. The governing equations for steady velocity potential for both wing-like and body-like elements are the small steady perturbations of the velocity components in x, y and z directions and further details can be found in [45].